

May 2014

Multilayer Nanomagnetic Systems for Information Processing

Srinath Rajaram

University of South Florida, srinath.nivas@gmail.com

Follow this and additional works at: <https://digitalcommons.usf.edu/etd>



Part of the [Electrical and Computer Engineering Commons](#)

Scholar Commons Citation

Rajaram, Srinath, "Multilayer Nanomagnetic Systems for Information Processing" (2014). *USF Tampa Graduate Theses and Dissertations*.

<https://digitalcommons.usf.edu/etd/5109>

This Dissertation is brought to you for free and open access by the USF Graduate Theses and Dissertations at Digital Commons @ University of South Florida. It has been accepted for inclusion in USF Tampa Graduate Theses and Dissertations by an authorized administrator of Digital Commons @ University of South Florida. For more information, please contact digitalcommons@usf.edu.

Multilayer Nanomagnetic Systems for Information Processing

by

Srinath Rajaram

A dissertation submitted in partial fulfillment
of the requirements for the degree of
Doctor of Philosophy
Department of Electrical Engineering
College of Engineering
University of South Florida

Major Professor: Sanjukta Bhanja, Ph.D.
Sudeep Sarkar, Ph.D.
Wilfrido A. Moreno, Ph.D.
Paris H. Wiley, Ph.D.
Karthikeyan Lingasubramanian, Ph.D.

Date of Approval:
April 2, 2014

Keywords: Multilayer spintronic devices, STT-MRAM, MRAM programmable grid, dipolar coupling

Copyright © 2014, Srinath Rajaram

DEDICATION

To my loving Parents, whose boundless sacrifices have brought me this far.

ACKNOWLEDGMENTS

I would like to take this opportunity to express my heartfelt gratitude to my mentor and major advisor Dr. Sanjukta Bhanja for giving me this opportunity and making my dream come true. Her constant support and belief in me has made me push my limits and become better both professionally and personally.

I extend my gratitude to Dr. Sudeep Sarkar, Dr. Paris H. Wiley, Dr. Wilfrido A. Moreno and Dr. Karthikeyan Lingasubramanian for being a part of my defense committee, whose inputs, support and guidance have been immensely helpful. Thank you for your valuable time.

I would like to thank the Department of Electrical Engineering and College of Engineering. I would like to thank Mr. Bernard Batson for all his help.

I would like to thank my wife, to whom I owe this success for her unconditional love and support and my parents for their sacrifices and encouragement.

I would like to acknowledge the National Science Foundation for financial support, which made this research possible.

Lastly, I would like to thank my colleagues Karthik, Anita, Dinuka, Ravi, Snetta, Munish, Jayita, Kevin, Drew who have been my friends and family here.

TABLE OF CONTENTS

LIST OF TABLES	iv
LIST OF FIGURES	v
ABSTRACT	ix
CHAPTER 1 INTRODUCTION	1
1.1 Motivation	1
1.2 Dissertation Objectives	4
1.3 Dissertation Outline	5
CHAPTER 2 RELATED WORK	7
2.1 Difficulties Arising Due to MOSFET Scaling	8
2.2 Emerging Beyond-CMOS Technologies	9
2.3 Spin-Transfer Torque Nanodevices	10
2.4 MRAM Basics	13
2.4.1 MRAM Write Operation	16
2.4.2 Phenomenology of Spin-Transfer Torque	17
2.4.3 STT-MRAM Device Types	19
2.4.4 Device Applications	20
2.5 Field-Coupled Computing Paradigm	20
CHAPTER 3 THEORETICAL BACKGROUND	22
3.1 Micromagnetics Foundation	22
3.2 Energy Terms	23
3.2.1 Exchange Energy	23
3.2.2 Anisotropy	24
3.2.2.1 Crystal or Magnetocrystalline Anisotropy	24
3.2.2.2 Uniaxial Anisotropy	25
3.2.2.3 Cubic Anisotropy	25
3.2.2.4 Shape Anisotropy	26
3.2.2.5 Stress Anisotropy	26
3.2.3 Magnetostatic Effects	26
3.2.4 Zeeman Energy	27
3.2.5 Magnetostatic Energy / Dipole-dipole Interaction Energy / Coupling Energy	27

3.2.5.1	Landau-Lifshitz Equation with Slonczewski Spin Torque	28
3.2.6	Switching Current Density	29
3.3	LLG Micromagnetic Simulation	30
3.4	Magnetic Field Coupled Computing Architectures	32
CHAPTER 4 BOOLEAN LOGIC COMPUTATION USING MULTILAYER NANOMAGNETS		35
4.1	Contributions	35
4.2	Introduction	38
4.3	The In-plane Device Logic Computation	38
4.4	The SyAF Device Logic Computation	41
4.5	The Perpendicular Device Logic Computation	42
4.6	The Tilted Device Logic Computation with Clocking and Switching Capabilities	44
4.6.1	Micromagnetic Model Parameters	45
4.6.2	Impact of Device Parameters on Writing and Clocking Tilted Devices	48
4.7	Results and Discussion	52
CHAPTER 5 STUDY OF NEIGHBOR INTERACTION BETWEEN NANOMAGNETIC DISKS		54
5.1	Introduction	54
5.2	Contribution	56
5.3	Micromagnetic Model	59
5.4	Simulation Results and Discussion	64
5.4.1	Effect of Diameter Variation on Interaction	64
5.4.2	Effect of Thickness Variation on Interaction	65
5.5	Fabrication	66
5.6	Conclusion	67
CHAPTER 6 PROGRAMMABLE NANOMAGNETIC GRIDS FOR NON-BOOLEAN COMPUTATION		69
6.1	Contribution	69
6.2	Introduction	71
6.3	Nanomagnets for Vision Computation - a Non-Boolean Framework	74
6.4	Design of Reconfigurable Array (STRAN) using LLG Simulation	76
6.5	Non-Boolean Computation using STRAN	86
6.6	Conclusion	87
CHAPTER 7 CONCLUSION		88
7.1	Future Work - Extension of Reconfigurable Nanomagnetic Grids for Boolean Computation	89
7.2	Programmable Nanomagnetic Grids using Multiferroic Structures	90

REFERENCES	93
APPENDICES	106
Appendix A Copyright Permission	107
ABOUT THE AUTHOR	End Page

LIST OF TABLES

Table 3.1	Magnetic moments of transition materials	24
Table 4.1	Input materials (Permalloy and Cobalt) magnetic parameters used for simulations.	41
Table 4.2	Comparison of SyAF, PMA and TD computing structures.	52
Table 5.1	Number of SDS and VS compared with the fabricated pairs of nano-magnetic disks	68
Table 6.1	STRAN cell critical deselection current	83
Table 6.2	Comparison of number of SDS magnets and VS magnets from fabricated patterns	87
Table 7.1	Logic-OR and NOR gates programmed in a 6x6 array of nanomagnets	91

LIST OF FIGURES

Figure 1.1	Comparison of memory technologies (From: [1])	2
Figure 1.2	MTJ cell in (a) Parallel and (2) Antiparallel configuration	3
Figure 2.1	A simple MOSFET device	7
Figure 2.2	Effects of CMOS scaling	8
Figure 2.3	Electron spin orientation	10
Figure 2.4	Spin-valve based on GMR effect	12
Figure 2.5	Magnetic tunnel junction	13
Figure 2.6	In-Plane MRAM devices	14
Figure 2.7	Out-of-plane MRAM devices	15
Figure 2.8	Field Induced Magnetization Switching (FIMS) MRAM	16
Figure 2.9	Direction of the magnetizations and spins of the electrons	18
Figure 2.10	Reference layer of a tilted device	20
Figure 2.11	STT-MRAM applications	21
Figure 3.1	Shape anisotropy	25
Figure 3.2	Schematic of Landau-Lifshitz equation	29
Figure 3.3	Discrete magnetization cell volume represented as 3-dimensional mesh structure in LLG simulation	31
Figure 3.4	Field coupled device architectures	33
Figure 3.5	Magnetization states encoded as two Binary logic states “0” and “1”	33
Figure 3.6	Majority gate architecture proposed by <i>Imre et al.</i> in [2]	34
Figure 3.7	Truth table of majority gate architecture that could be operated as AND or OR gates	34

Figure 4.1	Schematic of multilayer majority gate hardware with underneath CMOS devices	36
Figure 4.2	MRAM Binary logic representation	39
Figure 4.3	Schematic of an In-plane cell	39
Figure 4.4	Coupling failure in In-plane devices	40
Figure 4.5	Schematic of an SyAF Cell	40
Figure 4.6	Schematic of OR logic imlementation using SyAF devices	42
Figure 4.7	LLG simulation of SyAF OR logic implementation	42
Figure 4.8	Magnetization state vector of logic output	43
Figure 4.9	Schematic of an PMA cell	44
Figure 4.10	Magnetization vectors of AND gate operation.	44
Figure 4.11	Schematic of an TD cell	45
Figure 4.12	Initial magnetization state of free layer of input cell to be switched from A=1 to A=0 at $t=T_{Initial}$	46
Figure 4.13	Intermediate magnetization state of free layer of input cell to be switched from A=1 to A=0 at $t=T_{Intermediate}$	46
Figure 4.14	Final magnetization state of free layer of input cell switched to A=0 from A=1 at $t=T_{Final}$	46
Figure 4.15	Intermediate switching input state for tilted multilayer cell.	47
Figure 4.16	Magnetic alignment for tilted polarizer.	47
Figure 4.17	Final state of input switching using tilted polarizer.	48
Figure 4.18	Initial state of spin-torque clocking with tilted polarizer at time= $T_{initial}$	50
Figure 4.19	Intermediate magnetization state of clocked cell with tilted polarizer	50
Figure 4.20	Final magnetization state of clocked cell in +y-axis at time= T_{final}	50
Figure 4.21	Applying spin torque current to switch the magnetization of the TD devices	51
Figure 4.22	Spin torque current induced switching for TD devices	51

Figure 4.23	Magnetization graphs of output cell (C) for AND and OR logic operations for tilted devices.	53
Figure 4.24	Normalized magnetization graph of output cell (C) for different OR gate inputs Fixed = 0, A =1 and B =0	53
Figure 5.1	Phase diagram of single domain state and vortex state	56
Figure 5.2	Single domain state nanomagnetic disks with dimensions in the SDS region selected from [3]	56
Figure 5.3	Vortex state nanomagnetic disk with thickness ≥ 20 nm with dimensions in the VS region selected from [3]	56
Figure 5.4	Magnetization states representation of a nano-disk	57
Figure 5.5	Pair interaction energy between disks by varying the edge-to-edge spacing	58
Figure 5.6	Verification of the single domain state and the vortex state using MFM micrographs	59
Figure 5.7	Schematic of experiment conducted by varying the diameters D, thicknesses T and edge-to-edge spacing S.	60
Figure 5.8	The vector representation of a single domain state and vortex state	62
Figure 5.9	Magnetization direction of nano-magnetic disks superimposed on underlying domains	63
Figure 5.10	Pair interaction energy versus the spacing between nano-magnetic disks with thickness	64
Figure 5.11	The time evolution of magnetization state of a nanomagnetic disk with respect to different spacing	65
Figure 5.12	Pair interaction energy versus spacing between the disks with disk diameter D = 100 nm	66
Figure 6.1	Schematic of the programmable logic computation hardware	70
Figure 6.2	Object recognition using magnetic field-based computing proposed by <i>Sarkar et al.</i> in [4]	71
Figure 6.3	Schematic of STRAN cell dimension, material and spacing parameters.	72
Figure 6.4	Object recognition using magnetic field-based computing	73
Figure 6.5	Magnetic layout corresponding to the edge segments	74

Figure 6.6	Magnetic layouts for multiple images	75
Figure 6.7	The temporal evolution of the magnetization components under oscillation	77
Figure 6.8	Programming a pattern to a 3by3 STRAN	78
Figure 6.9	STT current induced deselection of the cell	79
Figure 6.10	Programming currents dependence on diameter of MTJ cell	80
Figure 6.11	Coupling energy graph between deselected (oscillating) magnet with its neighbors obtained using LLG simulation from the array.	81
Figure 6.12	Selection of cells using spin-transfer current, simulated using LLGS Micromagnetic simulator.	82
Figure 6.13	Schematic of region 1 in programmed STRAN hardware	83
Figure 6.14	STRAN output for region 1 layout	83
Figure 6.15	Schematic of region 2 in programmed STRAN hardware	84
Figure 6.16	STRAN output for region 2 layout	84
Figure 6.17	Schematic of region 3 in programmed STRAN hardware	85
Figure 6.18	STRAN output for region 3 layout	85
Figure 7.1	OR gate operation using a 6 x 6 MRAM reconfigurable array	89
Figure 7.2	Magnetization state of cell C3	91
Figure 7.3	Dipolar interaction between multiferroic structures	92
Figure A.1	IEEE copyright information	107

ABSTRACT

The Spin-Transfer Torque Magnetoresistive Random Access Memory (STT-MRAM) has opened new doors as an emerging technology with high potential to replace traditional CMOS-based memory technology. This has come true due to the density, speed and non-volatility that have been demonstrated. The STT-MRAM uses Magnetic Tunnel Junction (MTJ) elements as non-volatile memory storage devices because of the recent discovery of spin-torque phenomenon for switching the magnetization states. The magnetization of the free layer in STT-MRAM can be switched from logic “1” to logic “0” by the use of a spin-transfer torque. However, the STT-MRAMs have till now only been used as universal memory. As a result, STT-MRAMs are not yet commercially used as computing elements, though they have the potential to be used as Logic-In-Memory computation applications.

In order to advance this STT-MRAM technology for computation, we have used different MRAM devices that are available as memory elements with different geometries, to use it as computing elements. This dissertation presents design and implementation of such devices using different multilayer magnetic material stacks for computation. Currently, the design of STT-MRAMs is limited to only memory architectures, and there have been no proposals on the viability of STT-MRAMs as computational devices. In the present work, we have developed a design, which could be implemented for universal logic computation. We have utilized the majority gate architecture, which uses the magneto-static interaction between the freelayers of the multilayer nanomagnets, to perform computation.

Furthermore, the present work demonstrates the study of dipolar interaction between nanomagnetic disks, where we observed multiple magnetization states for a nanomagnetic

disk with respect to its interaction energy with its neighboring nanomagnets. This was achieved by implementing a single layer nanomagnetic disk with critical dimension selected from the phase plot of single domain state (SDS) and vortex state (VS). In addition, we found that when the interaction energy between the nanomagnetic disks with critical dimension decreases (increase in center-to-center distance) the magnetization state of the nanomagnetic disks changes from single domain state to vortex state within the same dimension. We were able to observe this effect due to interaction between the neighboring nanomagnets.

Finally, we have presented the design and implementation of a Spin-Torque driven Reconfigurable Array of Nanomagnets (STRAN) that could perform Boolean and non-Boolean computation. The nanomagnets are located at every intersection of a very large crossbar array structure. We have placed these nanomagnets in such a way that the ferromagnetic free layers couple with each other. The reconfigurable array design consists of an in-plane (IP) free layer and a fixed polarizer [magnetized out-of-plane (OP)]. The cells that need to be deselected from the array are taken to a non-computing oscillating state.

CHAPTER 1

INTRODUCTION

1.1 Motivation

There were only three types of Random access memory that prevailed for a long time in the semiconductor industry, with each device only performing adequately; Static Random Access Memory, also known as Static RAM or in short SRAM, Dynamic Random Access Memory or DRAM and Flash Memory. Of these types, SRAM was the most robust with excellent write speed and read speed, but the problem was with the dimension of the cell. The SRAM requires at least six or more CMOS transistors per cell. The operational efficiency of SRAM was quite impressive and it was ideally suited for cache memory, where the performance of the cell is less critical than the memory density. In addition to the cell size, the SRAM is volatile, but requires very low power for data retention [5, 6]. The next type, which is DRAM, was able to provide a better memory density, as it needs only a single transistor with a storage capacitor [7, 8]. However, the capacitor seems to be so leaky, that to maintain the charge in the capacitor the cell needs large amount of power with a high refresh cycle of few milliseconds [9]. This has limited the DRAM application only to the main memory of a system, where the density along with the performance is more important than the power consumed [10]. The last type of the memories, which is Flash memory, is very attractive because of its non-volatility and high density. The Flash memories have a reasonable speed, but the write speeds are slow and the endurance is very low [11, 12, 13]. Ideally, for the best performance, all three of these cells have to be mixed into a single device that is low power, high density, high endurance, high read/write speed and low cost [14]. Spin-Transfer Torque

Products/ Performance	SRAM	DRAM	Flash (NOR)	Flash (NAND)	FeRAM	MRAM	RRAM	STT-MRAM
Non-volatile	No	No	Yes	Yes	Yes	Yes	Yes	Yes
Cell Size [F ²]	50 - 120	6 - 10	10	5	15 - 34	16 - 40	6 - 10	6 - 20
Read Time [ns]	1 - 100	30	10	50	20 - 80	3 - 20	10 - 50	2 - 20
Write Time [ns]	1 - 100	15	1 μ s / 1ms	1ms / 0.1ms	50 / 50	3 - 20	10 - 50	2 - 20
Endurance	10 ¹⁶	10 ¹⁶	10 ⁵	10 ⁵	10 ¹²	> 10 ¹⁵	10 ⁸	> 10 ¹⁵
Write Power	Low	Low	Very High	Very High	Low	High	Low	Low
Power Consumption	Leakage	Refresh	None	None	None	None	None	None

Figure 1.1. Comparison of memory technologies (From: [1])

Magnetoresistive Random Access Memory (STT-MRAM) is an emerging memory technology that combines all the advantages of the three basic memory technologies and has the potential to become as a universal memory [15, 16, 1, 17, 18]. The interest in STT-MRAM has been tremendous in recent years because it is non-volatile, highly scalable, radiation hardened and has excellent write selectivity, low power consumption, simple architecture, easily integrated with other technologies and faster operation. A comparison table of the currently available memory technologies is shown in Fig. 1.1.

The STT-MRAM is actually a second generation MRAM family [1, 19, 16, 20, 21]. The MRAM uses the magnetization state of the magnetic layers to encode the binary bits “0” and “1”. The MRAM technology gained a lot of interest when the room temperature tunneling magnetoresistive read was discovered [22]. A schematic diagram of the MTJ element is shown in Fig.1.2. There are two possible magnetization states in an MTJ, based on the magnetization state of the freelay and the pinned layer, the parallel magnetization state and the antiparallel magnetization state. The parallel magnetization state refers to a low resistance state and is represented as R_P , while the antiparallel magnetization state refers

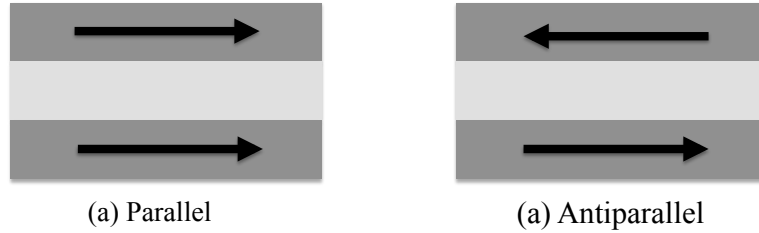


Figure 1.2. MTJ cell in (a) Parallel and (2) Antiparallel configuration

to a high resistance state and is represented as R_{AP} . The STT-MRAM uses spin-polarized current to write magnetic information in the MTJ cell.

The STT-MRAM requires only two to three additional masks to be integrated with the current CMOS technology, which accounts to less than 3% of the overall cost [23]. This technology has been able to replace existing universal memory, as it has several advantages and similarities over current technology. There have been significant number of papers published, which have presented 64 Megabyte STT-MRAM with 65 nm CMOS technology. In [24], authors have demonstrated a second generation MRAM technology, which is low power. In [15], a 22-nm technology miniaturization was achieved and more interestingly in [25, 26, 27] authors have easily integrated MRAM with 65 nm CMOS design kit. This chip was designed by STMicroelectronics [28] with 128K cross-point MTJ arrays. However, till now STT-MRAMs have been only viewed as a universal memory element. There has been only little work on TAS-MRAM based FPGA logic circuit [29, 30, 31], domain wall based logic circuits [32, 33, 34, 35, 36, 37] and no work on using these robust STT-MRAMs elements for logic computation. By selecting these STT-MRAM cells, we could design high performance non-volatile logic-in-memory circuits, which could replace the circuits built with traditional CMOS transistors. As we know, the STT-MRAM's attractive nature is a result of easy integration with CMOS technologies. It is possible to open a new field of logic computation using STT-MRAMs, which is a big challenge.

1.2 Dissertation Objectives

In this dissertation, we explore the physics behind the operation of STT-MRAM cells as computing cells. Till now, they have been only used as memory cells. The contributions of this dissertation follow:

- Boolean logic implementation using dipolar interaction among multi-layer spintronic devices: We have explored multi-layer spintronic structures directly for computation such that the computing and access mechanisms are homogeneous. This would solve multiple problems of integration, access and power requirements. Based on LLG simulation, we are the first to report successful dipolar interaction between neighboring free layers of multi-layer spintronic devices and utilized them to realize Boolean logic functions. This interaction between the multi-layer spintronic devices unveils new avenues of logic implementation for the future that offers possible solutions to the challenges faced by traditional logic realization.
- Dipolar neighbor interaction on magnetization states of nano-magnetic disks: We have investigated the effect of magnetic neighbor interaction on the state behavior of nano-magnetic disks for data storage and computation applications. We have observed and verified that a nano-magnetic disk with critical geometry can exist in either the single domain state or the vortex state depending on the edge-to-edge spacing between the disks. The experiments were conducted by varying the diameter and thickness with respect to edge-to-edge spacing. The dimensions of the disk were based on the phase diagram between the single domain state and the vortex state. We have observed, nano-magnetic disks spaced far apart from its neighbors settled in the vortex state and disks that were closely spaced settled in the single domain state. Based on our study, nano-magnetic disks with thickness in the range from 8nm to 20nm and diameter in

the range 80nm to 140nm, could exist in either the single domain state or the vortex state based on the change in edge-to-edge spacing between the nano-magnetic disks.

- Programmable Boolean and non-Boolean computation: We have presented the design and implementation of a Spin-Torque driven Reconfigurable Array of Nanomagnets (STRAN) that could perform Boolean and non-Boolean computation. The nanomagnets are located at every intersection of a very large crossbar array structure. We have placed these nanomagnets in such a way that the ferromagnetic free layers couple with each other. The reconfigurable array design consists of an in-plane (IP) free layer and a fixed polarizer [magnetized out-of-plane (OP)]. The cells that are to be deselected from the array will be taken to a non-computing oscillating state. In this work, we have shown: First, a non-Boolean framework effective to solve several instances of quadratic optimization problems, such as those arising in computer vision applications. Secondly, a Boolean logic computation framework with dynamically configurable architecture, flexible to operate as any logic is presented. The STT strengths, which have the ability to provide input to the free layer and induce oscillations for deselecting the cells, have been predicted through LLG simulations.
- We have presented preliminary work on design and implementation of a reconfigurable Boolean logic computation using Spin-Torque driven Reconfigurable Array of Nanomagnets (STRAN) and an efficient way of deselecting a cell from the array using multiferroic structures is also discussed in this dissertation.

1.3 Dissertation Outline

The organization of this dissertation follow,

- Chapter 2 provides background.
- Chapter 3 describes theoretical background on micromagnetism.

- Chapter 4 presents, in detail, Boolean logic implementation using multilayer spintronic devices.
- Chapter 5 explains, in detail, the effect of dipolar neighbor interaction on magnetization states of nano-magnetic disks.
- Chapter 6 explains, in detail, the design and implementation of a Spin-Torque driven Reconfigurable Array of Nanomagnets (STRAN) that could perform Boolean and non-Boolean computation.
- Chapter 7, concludes the dissertation and provides the future directions for this work.

CHAPTER 2

RELATED WORK

Till date, the MOS technology has met the growing needs for electronic circuits [38, 39, 40, 41, 42]. The main motivation that is powering today's electronics is miniaturization [43, 44, 45]. The metal-oxide-semiconductor field-effect transistor (MOSFET) is a device to amplify signals or can act as a switch in electronic circuits. The basic principle of operation was proposed in [46].

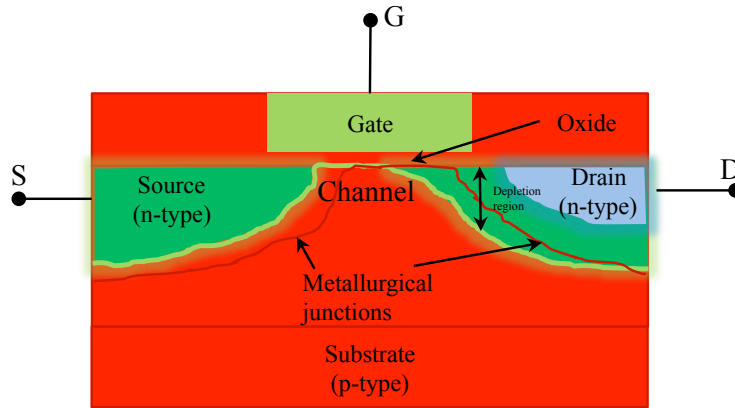


Figure 2.1. A simple MOSFET device

The MOSFETs are a three terminal device, voltage on the gate terminal creates an conducting channel between the source and drain as shown in Fig. 2.1. The channel could be p-type or n-type, accordingly p-MOSFET or n-MOSFET (commonly known as pMOS and nMOS) which is used in modern digital circuits.

2.1 Difficulties Arising Due to MOSFET Scaling

By making the transistor and the interconnect smaller and smaller, the number of devices fabricated on a single wafer has increased, thereby reducing the cost of manufacture and the power consumption [47, 48]. Each time the minimum width of the source-drain is reduced, we say the technology has stepped onto the next technology node. It also means that interconnects need to be reduced by 70% and thereby the signal delay increases. Additionally due to the subthreshold current, the transistor which has to be in “OFF” state is not completely “OFF”.

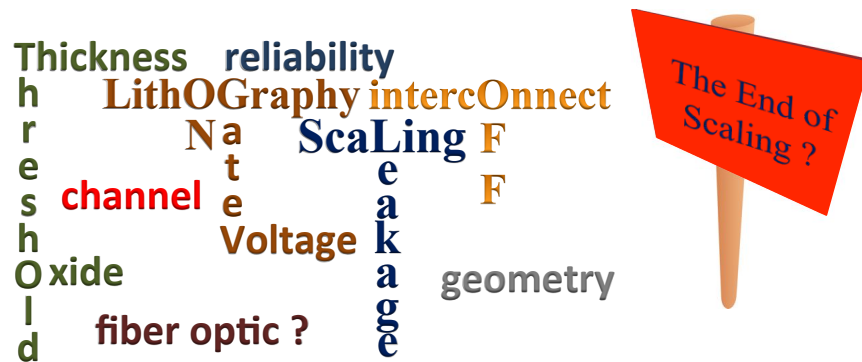


Figure 2.2. Effects of CMOS scaling

Over the past decade, MOSFETs have been continuously scaled down for the main reason to pack more and more devices in the same chip area [49, 50, 51]. This resulted in reduction of the size in all dimensions. By the reduction in channel width between the source and drain, there were several factors rising namely, reduction in gate voltage to maintain reliability, thinning the gate-oxide layer, junction leakage, interconnects, heat production. The two main factors that are caused due to scaling are discussed below,

- Channel length variation: Since the CMOS technology scaling has been the continuous key for its process, the gate-channel structures requires complex fabrication processes.

The channel length variation is caused by the increase in the depletion layer width, as the drain voltage increases. In extreme cases the channel length reduces to zero.

- Sub-threshold current: It has been assumed that no inversion layer charge exists below the threshold voltage. This condition leads to a “0” current below the threshold voltage. This condition is referred to as parasitic leakage in digital circuits where ideally there would be no current. Due to scaling, this subthreshold leakage current has been increasing from all sources and also there has been gate-oxide leakage and junction leakage. A solution for avoiding this leakage is a tedious task and still it is a critical step for most of the digital circuit designers.

2.2 Emerging Beyond-CMOS Technologies

There are various emerging beyond-CMOS technologies. These devices are based on Nano-mechanical devices, 3D vertical devices, Tunneling Field Effect Transistors, Spin devices [52, 53]. In nano-mechanical devices, the nanorelay is based on a conducting carbon nanotube placed on a silicon substrate. The nanorelay is a three terminal device that can act as a switch, amplifier and as memory element [54, 55]. These Nano-Electro-Mechanical-Systems (NEMS) are growing rapidly in research fields as a potential substitution for transistors. The tri-gate transistor has a single gate stacked up on two vertical gates allowing plenty of surface area for the electrons to travel [56, 57, 58]. These devices rely on electron travel, they tend to have reduced leakage, less power dissipation and higher speed. *Intel Inc.* has been using the tri-gate device in their recent *Ivy Bridge processors* and *Haswell processors* [59, 60]. The tunneling field effect transistors use quantum-mechanical tunneling to inject charge carriers into the device channel. The TFET’s are built on nanowires with a huge power reduction and also could be integrated with current CMOS technologies for low power integrated circuits. Finally, the spin-torque devices use the orientation of the spin of the electrons to carry the information. These devices offer improved area and power

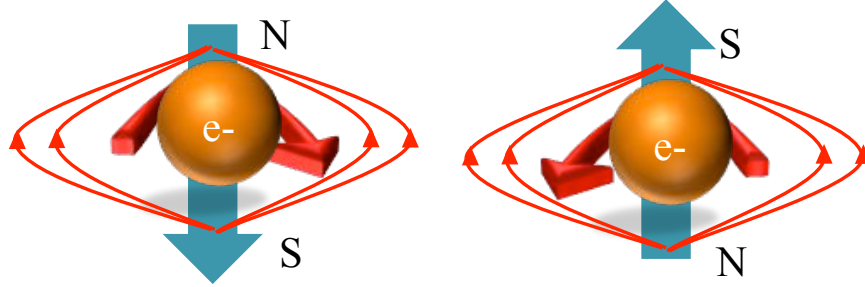


Figure 2.3. Electron spin orientation

consumption over other devices [61, 62]. We will discuss more about this device, which is the main focus of this dissertation work.

2.3 Spin-Transfer Torque Nanodevices

Spintronic devices emerged from the spin-dependent electron transport in devices [63, 64]. The observation of spin-polarized electron transfer from a ferromagnetic material to another metal, led to the discovery of Giant-Magnetoresistance (hereafter GMR) by *Albert Fert and Peter Grunberg (1988)* [65, 66, 67]. The use of spintronic devices can go beyond several theoretical proposals from the 1990s.

What constitutes a Spintronic device? The electrons are normally 1/2-spin fermions. They constitute two states of spin system, spin “UP” and spin “DOWN” as shown in Fig. 2.3. For a system to be termed as a spintronic device, which is spin electrons, the device should have the capability to generate spin-polarized electrons. These spin-polarized electrons can have either the UP spin or the DOWN spin. The spintronic device together has several layers contributing to a different purpose. One of its layers can generate the spin-polarized electrons called the spin-injector; the other layer is the detector, which can detect the spin-polarized electron. Manipulation of the direction of the spin-polarized electron from the injector to the detector can be done though external magnetic fields.

This led to the discovery of the popular device “Spin-valve” by IBM researcher Stuart Parkin with his colleagues [68, 69, 70, 71]. This device is capable of changing its magnetic state at atomic level. This discovery has changed the depiction of data storage devices to a different level with a dramatic increase in storage capacity. Later, IBM research scientists following the discovery of GMR, realized that the spintronic device could be a valuable member for the GMR based hard disk read heads. Later, *Parkin* found that by applying a small magnetic field, he could alter the current flowing through the device. The reason of this significant change is because, when the current flows through the different layers, the current gets spin-polarized and all electrons in the device gets spin-polarized in one direction with “UP” or “DOWN”, depending on the magnetic orientation of these layers. By giving a small magnetic field, we could reorient these layers, switching “ON” and “OFF” just like valves. This device also has the capability to detect minute changes in the magnetic field in a hard drive. This led to the development of the GMR sensor for high performance read capability. The first commercial use of spin-valve based GMR read head from IBM was during 1997 when they released Titan [72]. Today, Tunneling Magnetoresistance (TMR) has replaced GMR. Based on the physics of the device, the device is still spintronic. Since 2007, the basic spintronic device has been improved with thinner layers with very high tunneling magnetoresistance.

The GMR is a quantum mechanical magnetoresistance effect, which is observed in thin-films of a non-magnetic layer (NM) sandwiched between two ferromagnetic layers (FM) as shown in Fig. 2.4. The 2007 Nobel Prize in Physics was awarded to Albert Fert and Peter Grunberg for the discovery of GMR effect. It is what is now being used to read data from the hard disk drives and many other Microelectromechanical systems with GMR magnetic field sensor [73]. The readout is the significant change in resistance depending on the adjacent magnetization of the magnetic layers, where the magnetizations can be parallel or antiparallel. The overall resistance of the device is low when the magnetizations

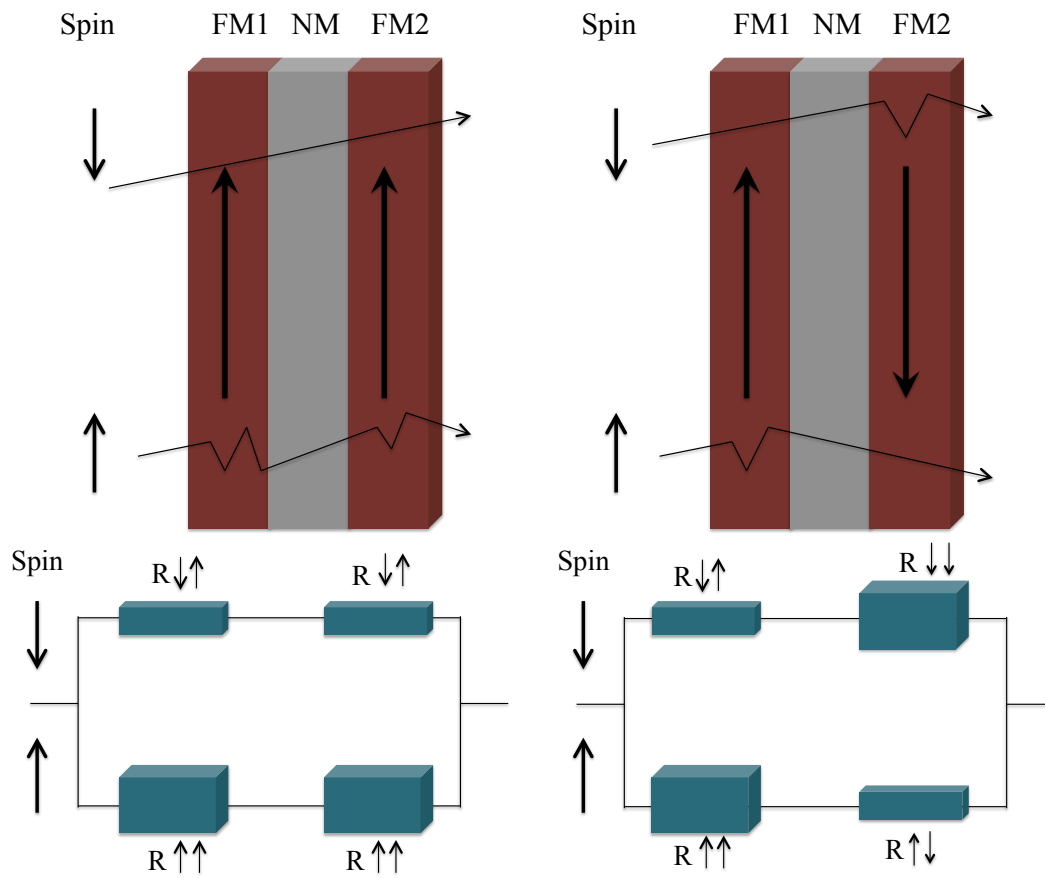


Figure 2.4. Spin-valve based on GMR effect. FM: Ferromagnetic layer, NM: Non-magnetic layer. Arrows indicate the magnetization direction.

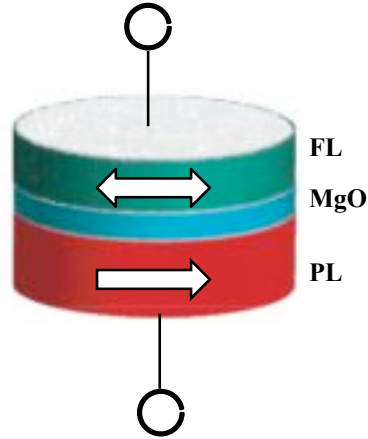


Figure 2.5. Magnetic tunnel junction

of the adjacent layers are parallel. When the magnetizations of the adjacent layers are antiparallel then the resistance is relatively higher. Applying external magnetic field controls, the magnetization of the free layer. The GMR effect is based on electron scattering on the orientation of spin.

2.4 MRAM Basics

The STT-MRAM has the potential to scale below 60nm, with the reduction in the current by more than a hundred-fold. The STT-MRAM has proved to be an excellent candidate for a universal memory, because of its non-volatility nature, low power, increased performance and high memory sensitivity. However, the possibilities of a computation paradigm using these STT-MRAM have not been opened up.

MRAM has emerged as a non-volatile memory technology that garnered tremendous interest over the past two decades [19, 1, 19, 16, 20, 21]. The basic MRAM cell is Magnetic Tunnel Junction (from now referred as MTJ), shown in Fig. 2.5. An MTJ consists of a oxide-tunneling barrier layer (MgO) sandwiched between two ferromagnetic layers, Pinned Layer (PL) and Free Layer (FL) [74]. As one can identify from the name, the Pinned Layer (PL) has its magnetization vector fixed in one direction. Thus, the magnetization

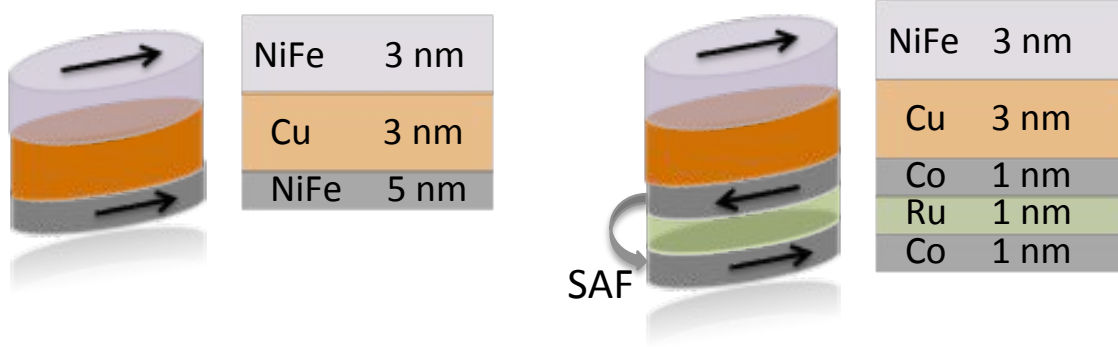


Figure 2.6. In-Plane MRAM devices

cannot be changed in PL, whereas in FL the magnetization is free to rotate in its easy-axis directions. In conventional MTJ, the magnetization vector in the FL can take two directions, corresponding to the PL, parallel or antiparallel. For non-volatile data storage applications, an MTJ can store 1-bit data with the cell having two states: Parallel (P) state and Antiparallel state (AP). One of the interesting aspects of this MTJ is the tunneling magnetoresistance dependence between the P and AP states.

The vectors are represented as R_P and R_{AP} respectively for Parallel and Antiparallel states. For an MTJ, $R_{AP} \geq R_P$. It is very clear that the two states are electrically distinguishable with their difference in their resistances. A common TMR ratio is given as;

$$TMR = \frac{R_{AP} - R_P}{R_P} \quad (2.1)$$

So a large TMR ratio indicates the difference between the P and AP states is quite large. The TMR ratio is very important as it determines how easily the two states are distinguishable.

Numerous types of MRAM structures have been proposed. In various designs, the major differences are in the magnetization state of the PL. There are four different MRAM struc-

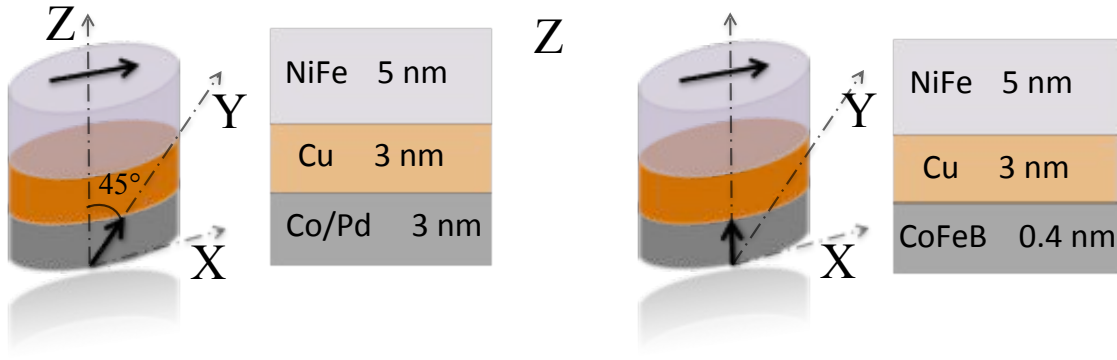


Figure 2.7. Out-of-plane MRAM devices

tures that have been proposed till now and can be categorized into In-plane and Out-of-Plane devices as shown in Fig. 2.6 and Fig. 2.7

- In-Plane devices (IP)
- Synthetic AntiFerro devices (SAF)
- Perpendicular devices (PMA)
- Tilted Devices (TD)

All of the different types of the MTJs have similar read schemes. As discussed above, the state of the MTJ can be inferred from their resistance differences. The information stored in the MTJ can be read by applying a small current through the MTJ and measuring the resulting voltage or by applying a voltage across the MTJ and measuring the current. The read current/voltage can be sensed and compared with the reference value determined from the reference cell. So, what is the main difference in the MRAMs? It is in the write operation. A brief discussion on the write operation is discussed in the next section.

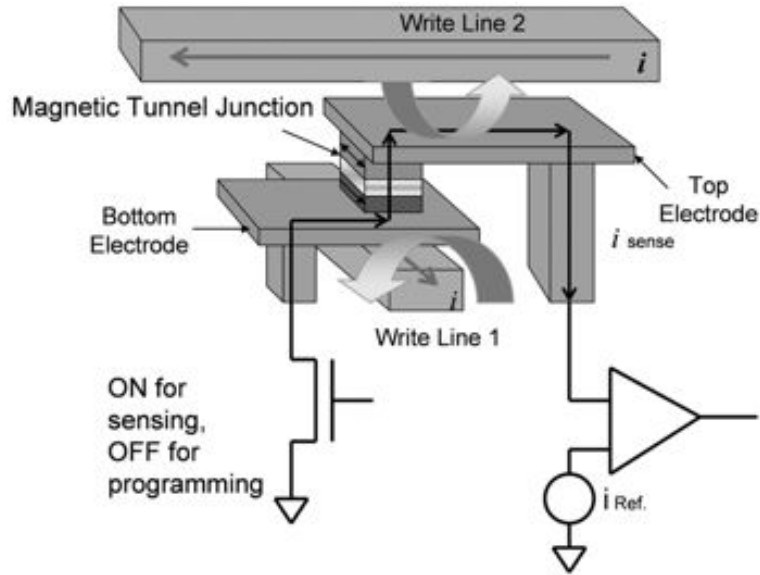


Figure 2.8. Field Induced Magnetization Switching (FIMS) MRAM (Obtained from [75])

2.4.1 MRAM Write Operation

Primarily, there are two types of MRAM: Field-induced MRAM (FIMS-MRAM) and Spin Transfer Torque MRAM (STT-MRAM). The Field-Induced MRAM, is the first type of MRAM, proposed in [76, 75, 77]. In this type of MRAM, a magnetic field is used to write information to the cells. Fig. 2.8 depicts the FIMS MRAM cell design. The MRAM cell design has two lines to generate magnetic fields for write operation (write line 1 and write line 2). When there is a current flowing through them, the two magnetic fields will be able to switch the magnetization of the FL [75]. There are several drawbacks of this type of scheme: The magnetic fields generated by the write lines are difficult to contain and focus on single spot. It also creates a disturbance in the magnetization state of neighboring cells when there is write process being executed with neighbors. Additionally, the FIMS-MRAM cells have shown poor scalability. These factors have made this type of MRAM technology too expensive in precise process technologies and has led to the development of a ultra-high performance STT-MRAM technology.

2.4.2 Phenomenology of Spin-Transfer Torque

The detailed theoretical description of the derivation of quantum mechanical effects of spin-transfer torque can be found in [78]. Here, we give the macro spin model of the spin-transfer torque developed in [78, 79].

In [80, 81, 82], they have studied the spin-transfer mechanism with angular momentum from the electrons in the ferromagnet. There are different processes that contribute to the angular momentum of the spin torque electrons.

- Because of the reflection probabilities of the electron leads to discontinuity of the spin components, which is later absorbed at the interface of the layers. This will give rise to a torque in the free layer magnetization and fixed layer magnetization will tend to align them.
- The scattered spins in the interface leads to another component, which is perpendicular to the plane formed by the magnetization of the free layer and the fixed layer, which is called as the perpendicular torque.

This phenomenon happens both in GMR and TMR, but there are very minute differences between the conduction of the spin electrons, through the spacer in GMR and the barrier in MTJ.

Consider a trilayer of fixed and free FM layers separated by a NM spacer layer shown in Fig. 2.5. The magnetization of the pinned layer is assumed to be pinned (in real case, it is pinned by an AFM layer) and cannot be flipped by any current density [83]. There is an angle θ between the magnetizations of two FM layers for current switching purpose. When the incoming spin orientation is collinear with the magnetization of the FM layer ($\theta=0$ or π), there will be no torque exerted [84].

Electrons always move in the opposite direction of the current. When current flows from the free to fixed layer, the s-band electrons will be spin-polarized in the direction of the

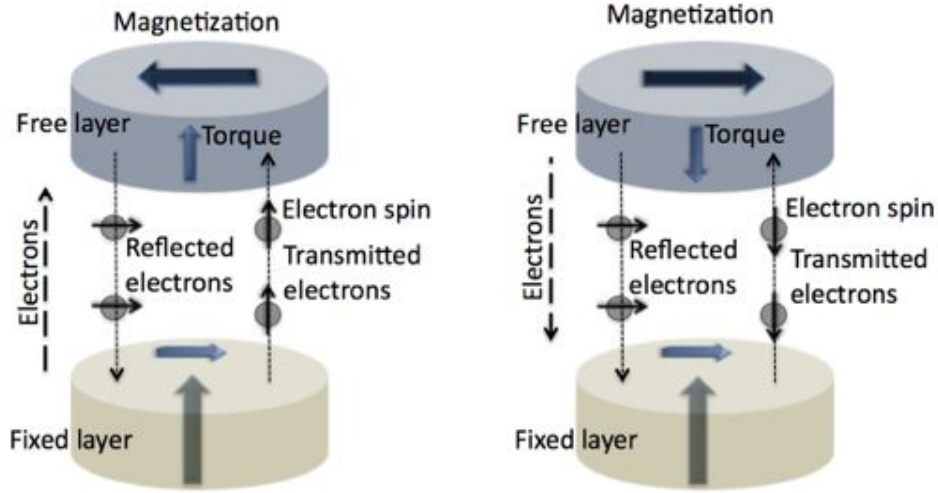


Figure 2.9. Direction of the magnetizations and spins of the electrons

magnetization of the pinned layer [85]. This is the first spin-filtering event: majority-spin electrons, with pinned layer, are able to pass through the spacer layer. The minority electrons accumulate in the FM layer. The second spin-filtering event happens in the free layer. When the electrons reach the free layer, exchange interaction occurs [85]. The electrons will align themselves along the magnetization of the free layer. Therefore, the spin will start to precess around the magnetization of the free layer. Since the precession is averaged over all electrons, transverse components of spin angular momentum becomes zero [86]. Due to conservation of spin angular momentum, the transverse components of the electron spins will be absorbed and transferred to magnetization of the free layer. Therefore, the same interaction also applies a torque on the free layer magnetization, making the magnetization of the free layer align towards the magnetization of the pinned layer. This torque effect is commonly known as spin transfer torque (STT). The minority electrons with respect to the free layer will be reflected back to the fixed layer, the magnetization of the pinned layer will not change because this torque is not strong enough. If the current density is high enough, that is more than critical switching current (usually around $10^7 A/cm^2$), the torque applied by the spin of electrons can switch the magnetization of the free layer [84]. Similar situation happens

when the electrons move from the free layer to the fixed layer with one exception. The torque exerted by the electrons that precess around the magnetization of the pinned layer is insufficient to switch the magnetization. The minority electrons are reflected back to the free layer. These electrons apply torque that is enough to switch the magnetization of the free layer antiparallel to the fixed layer. The strength of the torque is normally expressed as the magnitude of current density.

2.4.3 STT-MRAM Device Types

STT-MRAM can be broadly classified into two major categories:

- In-plane
- Out-of-plane

It is essential to know that the source of anisotropy for in-plane devices and out-of-plane devices is different. The anisotropy of in-plane device comes from the shape and geometry of the cell. For out-of-plane devices, the anisotropy source is from the magnetocrystalline effect. Due to the geometric effects in the in-plane devices, these cells have a large out-of-plane demagnetization field, while the out-of-plane devices virtually have no out-of-plane demagnetization field. The critical currents for in-plane and out-of-plane devices are given below. For in-plane devices,

$$I_{Co} = \frac{2e\alpha M_S V (H_K + 2\pi M_S)}{\hbar\eta} \quad (2.2)$$

For out-of-plane devices,

$$I_{Co} = \frac{2e\alpha M_S V H_K}{\hbar\eta} \quad (2.3)$$

As one can see, the ratio between the critical currents for in-plane and out-of-plane devices gives; $(H_K + 2\pi M_S)/H_K$, which is much larger than unity, because $M_S \gg H_K$. The reduction

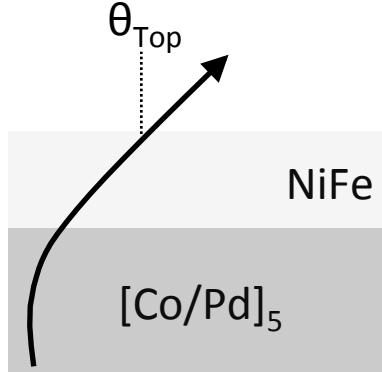


Figure 2.10. Reference layer of a tilted device. The magnetization is inclined at certain angle with Co/Pd material deposited under annealing

in the critical current for out-of-plane devices has made them the best design for STT-MRAM applications. However, it has been observed that these in-plane devices have very low TMR, which leads to performance issues, the out-of-plane devices have shown improved TMR as compared to in-plane devices. The tilted anisotropy can be achieved by, Co/Pd multilayer material. This material has strong perpendicular anisotropy and by introducing an in-plane material NiFe, due to the competition of two distinct anisotropies, unique magnetic configurations can be achieved. It has been observed, that the magnetization in the NiFe layer is tilted out-of-plane as shown in Fig. 2.10.

2.4.4 Device Applications

2.5 Field-Coupled Computing Paradigm

We have discussed in detail the fundamental limitations of current MOSFET technology and the scaling limits. Though several modifications have been proposed and implemented with design and material innovations, to push the scaling limit with vertical 3D transistors, high-k dielectrics etc., these developments would not help us in sustaining the scaling. Hence, there is a need for much smarter logic devices that could give us the same performance and the possibilities of scaling down. This section briefly discusses the new technologies being

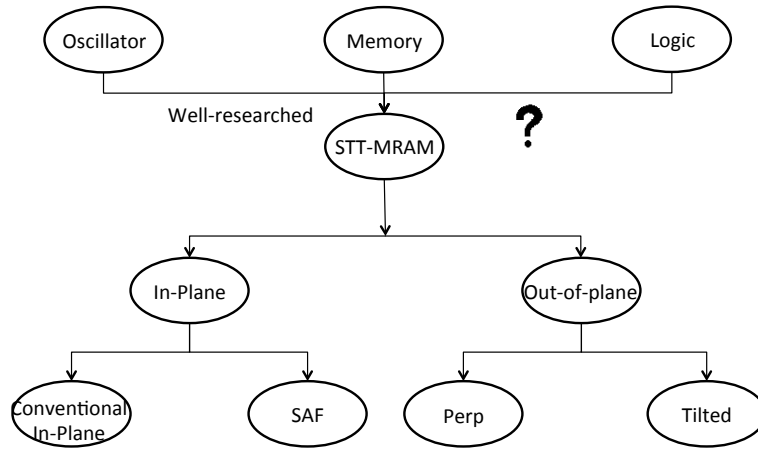


Figure 2.11. STT-MRAM applications

explored as an alternative to MOSFET technology without compromising on performance. Fig. 2.11 gives us an brief idea of the emerging technologies especially for the computing paradigm.

CHAPTER 3

THEORETICAL BACKGROUND

In this chapter we will discuss the magnetic energies, Micromagnetic equation governing the behavior of physical phenomenon. The magnetic interaction, which is influenced by different physical phenomena are mainly discussed in detail in this section.

3.1 Micromagnetics Foundation

The history of micromagnetics evolved during 1935 by Landau and Lifshitz and 1940 by Brown. The micromagnetic theory was limited to use the standard energy minimization to determine the domain structures. Around 1980's with the increased power of computing hardware availability, there has been a tremendous interest enabling more studies of realistic problems which are closely proved with experimental data. During this period one of the important fact that energy minimization approach can be dynamically solved using Landau-Lifshitz equation of motion was realized and it got a lot of momentum and has been most commonly used since then. The other area of exploration was happening parallel with the calculation of different magnetostatic energies, which contributes most of the calculations performed in Micromagnetics.

There are three major energy terms that one cannot neglect while performing micromagnetic calculations, which are exchange energy, anisotropy energy and magnetostatic energy. The magnetization behavior of a material depends on the balance between these magnetic energy terms that tries to bring the magnetization to a ground state. In current micromagnetic simulators, they ignore the atomic nature of the matter to neglect quantum mechanical

effects and use classical physics as a continuum description of magnetization material calculations. In these calculations, we assume a continuous magnetization vector field $M(r)$, where r is the position vector and M_s is the saturation magnetization of the material as shown in Eq. 3.1.

$$M(r) = M_s m(r); m \cdot m = 1 \quad (3.1)$$

3.2 Energy Terms

The micromagnetics deal with the interactions between magnetic moments governed by several energy terms. Each of the energy terms is explained in upcoming sections.

3.2.1 Exchange Energy

The exchange energy establishes an important role of covalent bonding in many solids and is the primary cause of the ferromagnetic coupling. The exchange energy is given by,

$$E_{exch} = -2JS_1 \cdot S_2 \quad (3.2)$$

where J is the exchange integral, S_1 and S_2 are atomic spins. For an ideal ferromagnetic coupling, J is positive and is dependent on the atomic property of the material. This interaction is termed as *exchange coupling* and arises from short-range interactions. Another model is Ruderman-Kittel-Kasuya-Yoshida (RKKY) interaction.

The exchange energy being a short range force, the total exchange energy of the magnetic layer would be the summation of the entire individual nearest neighbor spins. With this definition, the exchange energy can be written as,

$$E_{exch} = JS^2 \sum \phi_{ij}^2 \quad (3.3)$$

Table 3.1. Magnetic moments of transition materials

Material	Symbol	Configuration	Crystal	Moment ($A.m^2$)	$E_{exch}(J)$
Iron	Fe	bcc	$3d^5$	2.22×10^{-23}	-1.21×10^{-21}
Cobalt	Co	hcp	$3d^8$	1.72×10^{-23}	-5.51×10^{-21}
Nickel	Ni	fcc	$3d^7$	0.61×10^{-23}	-4.46×10^{-21}

The ϕ_{ij} represents the angle between the two neighboring spins i and j . So, if the magnetic moments align parallel, the material is ferromagnetic. If the moments align antiparallel to each other, then the material is antiferromagnetic. Table. 3.1 represents the magnetic moment energy and the exchange energy between two parallel ferromagnetic magnetic moments of different transition metals. By reversing the sign of the energy values represent antiparallel moments.

3.2.2 Anisotropy

The anisotropy energy refers to the properties of the ferromagnetic material, which depends on the direction of measurement. In several experiments, researchers have observed the energetically-favoured directions that could exist for different materials. In ferromagnetic materials, without any external fields, the magnetization tends to rotate along specific direction, which is referred as easy-axis direction. The anisotropy energy contributes an important part in the hysteresis curve of a magnetic material. There are several possibilities of occurrence of anisotropy energy:-

3.2.2.1 Crystal or Magnetocrystalline Anisotropy

This is related to the intrinsic property of the atomic level of a material. In materials with large anisotropy there exists strong coupling between the internal spins and angular momentum in atomic level. With the shape anisotropy, the orbits would prefer to lie in certain crystallographic direction. The spin-orbit coupling makes sure the magnetization

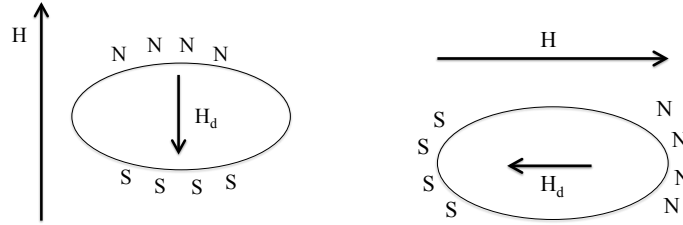


Figure 3.1. Shape anisotropy

settles in a preferred direction, called the easy-axis direction. So if one would needs to rotate the magnetization away from its easy-axis direction, energy must be spent - called anisotropy energy. This anisotropy energy is highly dependent on the atomic lattice structure.

3.2.2.2 Uniaxial Anisotropy

The most common anisotropy effect occuring due to one easy-axis direction is referred as uniaxial anisotropy. This occurs in in hexagonal crystals as Cobalt.

$$E = KV \sin^2\theta + \text{higher terms.} \quad (3.4)$$

where θ is the angle between the easy direction and the magnetization, K is the anisotropy constant, V is the volume of the sample.

3.2.2.3 Cubic Anisotropy

In this case, the anisotropy energy density has cubic density. This anisotropy occurs due to the spin-lattice coupling in cubic crystals such as Iron.

$$EV = K_o + K_1 + \alpha_1^2 \alpha_2^2 \quad (3.5)$$

where α is the direction cosine of the angle between the magnetization.

3.2.2.4 Shape Anisotropy

This type of anisotropy is due to shape of the material grain. Every magnetic body produces magnetic charges at the surface when it is isolated and is in itself a magnetic field source. This is called as demagnetizing field and it acts opposite to the magnetization that produces it. The demagnetization field is less when the magnetization is along the longest axis than when it is along the shorter axes.

3.2.2.5 Stress Anisotropy

This arises from the change in lattice structures, as a material is expands or contracts in one direction. This phenomenon is related to the “magnetostriction” which is also one of the upcoming field of study for high-density magnetic recording.

3.2.3 Magnetostatic Effects

The magnetostatic fields are natural fields arising from magnetization distribution. These magnetostatic fields are fundamental to a micromagnetic problem. The magnetostatic effects which gives rise to magnetization structures orders of magnitude greater than the lattice structure. The magnetostatic energy or the demag energy H_d is given by,

$$\nabla \times H_d = 0 \quad (3.6)$$

$$\nabla(H_d + 4\pi M) = 0 \quad (3.7)$$

The demagnetization field can be given as,

$$H_d = -\nabla\phi \quad (3.8)$$

By substituting the value of H_d we get,

$$\nabla^2\phi = -4\pi\nabla.M \quad (3.9)$$

3.2.4 Zeeman Energy

In 1896, Zeeman discovered the effect using the Bohr design of an atom. In his Zeeman-Lorentz force explanation an electron moving in a magnetic field, experiences a force that changes the orbit of the electron. The Zeeman energy effect is the splitting of energy in atoms, where there is an external energy applied to it. This is caused due to the interaction of magnetic moments μ in the atom with the magnetic field B which is slightly shifted by,

$$\nabla E = -\mu.B \quad (3.10)$$

The energy shift is dependent on the amount of the external field applied and also the direction of the magnetic moment.

3.2.5 Magnetostatic Energy / Dipole-dipole Interaction Energy / Coupling Energy

Consider two magnetic moments μ_1 and μ_2 , parallel to each other. The dipole interaction between these two magnetic moments can be given as,

$$E_{dipole-dipole} = \int \frac{\mu_1\mu_2}{r_3} 3\cos^2\theta - 1 \quad (3.11)$$

From the above equation, we can get some understanding on the nature of the dipole-dipole interaction. The dipole-dipole interaction strength is dependent on several factors: 1) the magnitude of coupling energy between the dipoles, 2) the distance between the dipoles, 3) the direction of the dipoles relative to one another. The rate of the dipole-dipole interaction is normally square of the dipole-dipole strength. So, if the rate of fall is $\frac{1}{r_3}$, the rate of

interaction is $\frac{1}{r_6}$. The second term $3\cos^2\theta - 1$ plays an important role under different conditions: 1) when the distance between the dipoles is a constant r , this term with θ determines the effective interaction energy the vector r makes with the z-axis, 2) the term averages to zero if all the angles are represented over the distance $\frac{1}{3}$.

3.2.5.1 Landau-Lifshitz Equation with Slonczewski Spin Torque

The time evolution of a tangible depends on the Hamiltonian of the system. The *Spin* operator in the dynamics of magnetization follows the Heisenberg equation of motion:

$$i\hbar\frac{d}{dt}\langle\hat{S}\rangle = \langle[\hat{S}, \mathcal{H}]\rangle \quad (3.12)$$

where H is the Hamiltonian of the magnetic layer.

The temporary collective spin of the magnetization in the layer, where the magnetization is free to rotate in its easy axis, can be written as,

$$\frac{d\hat{m}}{dt} = -|\gamma|\hat{m} \times H_{eff} \quad (3.13)$$

In a spin-valve or and magnetic tunnel junction devices, the spins in the free layer will experience an effective field H_{eff} which has, applied field, anisotropy field, and demag field.

As discussed in first section, in the spin-torque effect proposed by Slonczewski and Berger, the magnetization state can be controlled by electric current [87, 88]. The Hamiltonian, which includes all the energy terms and the spin-transfer current, is derived in [89, 90, 91]. By including the damping term to the LLG equation, we get,

$$\frac{d\hat{S}}{dt} = -\frac{g\mu_B}{\hbar}\hat{S} \times H_{eff} - 2\frac{J_{sd}}{\hbar}\hat{S} \times \hat{S}_M + \alpha\hat{S}\frac{d\hat{S}}{dt} \quad (3.14)$$

$$\frac{d\hat{m}}{dt} = -\gamma\hat{m} \times H_{eff} + \alpha\hat{m} \times \frac{d\hat{m}}{dt} + \frac{\gamma}{\mu_0 M_s}\tau \quad (3.15)$$

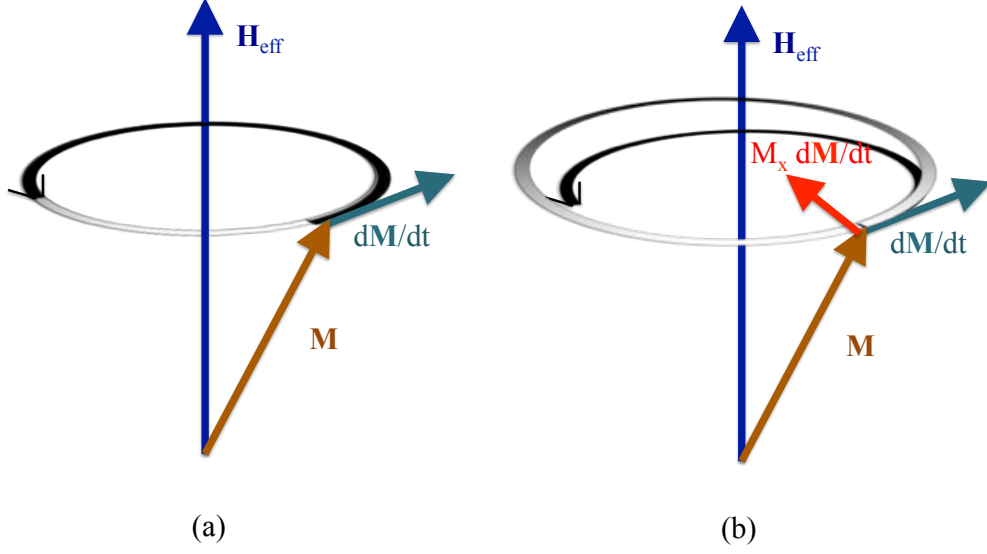


Figure 3.2. Schematic of Landau-Lifshitz equation. (a) The orange line refers to the magnetization precession around the effective field. (b) The magnetization precession with Gilbert damping term.

where \hat{m} is the magnetization unit vector and M_s is the saturation magnetization.

3.2.6 Switching Current Density

The critical current density required to cause magnetization reversal at zero temperature using macrospin approximation is given as,

$$\frac{d\mathbf{M}}{dt} = -\gamma\mathbf{M} \times \mathbf{H}_{\text{eff}} + \frac{\alpha}{M_s}\mathbf{M} \times \frac{d\mathbf{M}}{dt} + \frac{\gamma a_j(\theta)}{M_s}\mathbf{M} \times (\mathbf{M} \times \mathbf{p}) \quad (3.16)$$

$$J_{c0} = \left(\frac{2e}{h}\right) \times \left(\frac{\alpha}{\eta}\right) \times (M_s t_F) \times \left(\pm H_e x t + H_k + 2\pi M_s - \frac{H_{k\perp}}{2}\right) \quad (3.17)$$

or equivalently in terms of current,

$$I_{c0} = \left(\frac{2e}{h}\right) \times \left(\frac{\alpha}{\eta}\right) \times (M_s A t_F) \times \left(\pm H_e x t + H_k + 2\pi M_s - \frac{H_{k\perp}}{2}\right) \quad (3.18)$$

3.3 LLG Micromagnetic Simulation

In this section, we review the micromagnetic spin model, that is used in LLG simulator [92], developed by Michael R. Scheinfein, which is widely used to study the magnetization dynamics of nanomagnetic materials.

The micromagnetic structure present in the surface domains, can be extracted with the solution to the Landau-Lifshitz-Gilbert equation shown in Equ. 4.1. These methods are given in [93, 94, 95]. The magnetization equilibrium results from the energy minimization of the system. We have already seen that a ferromagnetic system is composed of various energy terms namely, the exchange energy E_{ex} denoted by the exchange coupling constant A (erg/cm), the magnetocrystalline anisotropy energy denoted by K_v (erg/cm³), the magnetostatic self-energy, the external energy and the magnetostrictive energy arising from strain. The solution for the energy minimization problem is considered as a boundary condition problem in 2D or 3D space, with the constraint of constant saturation magnetization across the whole sample. This continuous magnetization across the sample is approximated by discrete magnetization distribution of same volume in cubes for 3D and rods for 2D. The finite approximation method to solve the LLG equation shown in Equ. 4.1. In this type of approximation, each individual discrete magnetization cell volume would be treated as 3-dimensional mesh structure as shown in Fig. 3.3. In this 3D simulator, the cells discretized along x-axis contains N_x elements, y-axis contains N_y elements and z-axis contains N_z elements. So, the total simulation volume would be consisting of $N_x \times N_y \times N_z$ cells. As discussed before, the bulk saturation magnetization M_s normally does not fluctuate much across the ferromagnetic sample with different material parameters at room temperature. The value of the magnetization vector, $M(\mathbf{r})$ within the ferromagnetic sample is the saturation magnetization multiplied with the direction cosines, which is $M(\mathbf{r}) = (M_x(\mathbf{r}), M_y(\mathbf{r}), M_z(\mathbf{r}))$, which is in turn with the direction cosines represented as, $M_s \alpha(r) = M_s(\alpha(r), \beta(r), \gamma(r))$. This equation has the magnetization vector $M(\mathbf{r})$ assumed as $\alpha(r) = 1$. The energy terms are computed over

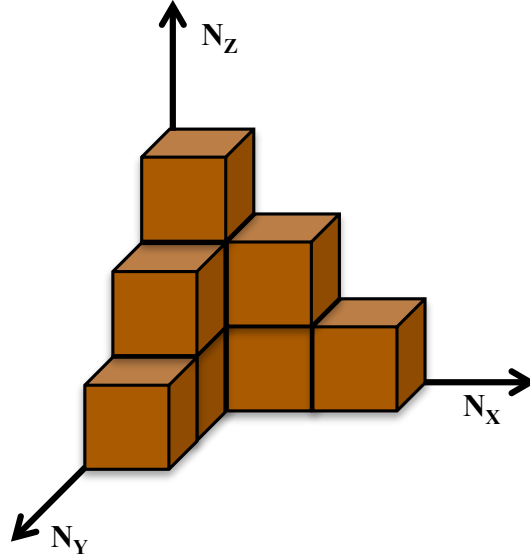


Figure 3.3. Discrete magnetization cell volume represented as 3-dimensional mesh structure in LLG simulation

the appropriate integral over the dimension of the ferromagnetic sample dV . The exchange interaction between each spin can be approximated as,

$$E_{ex} = \int dV [|\nabla \alpha^2| + |\nabla \beta^2| + |\nabla \gamma^2|] \quad (3.19)$$

The exchange coupling constant A (erg/cm), can be obtained from the spinwave [96, 97, 98]. This single spin eases the trace of the magnetization direction. This is more than sufficient for us to study different aspects of spin-transfer torque induced magnetization switching and precession in magnetic nanostructures.

To calculate the magnetic geometry of a ferromagnetic sample, the time evolution of the magnetization configuration inside a ferromagnetic structure, which is described by the LLG equation, must be solved. The equation has the following form,

$$\frac{d\tilde{\mathbf{M}}}{dt} = -\frac{\gamma}{1 + \alpha^2} \tilde{\mathbf{M}} \times \tilde{\mathbf{H}}_{\text{eff}} - \frac{\gamma\alpha}{(1 + \alpha^2)M_s} \tilde{\mathbf{M}} \times (\tilde{\mathbf{M}} \times \tilde{\mathbf{H}}_{\text{eff}}) \quad (3.20)$$

The LLG simulation algorithm is mentioned below,

1. The variables N_x number along x-direction, N_y number along y-direction and N_z number along z-direction variables are loaded.
2. The fields H_x field in Oe along x-direction, H_y field in Oe along y-direction and H_z field in Oe along z-direction are initialized.
3. The material parameters including exchange constant, saturation magnetization, uniaxial anisotropy, cubic anisotropy, surface anisotropy, resistivity and anisotropy magnetoresistance are obtained from the material database with respect to the material label.
4. The demagnetization coupling tensor is loaded into the environment along the N_x , N_y and N_z directions.
5. All the output parameter files such as direction cosines file, movie file, magnetization masking file which carries the magnetic cell dimension parameters are initialized.

3.4 Magnetic Field Coupled Computing Architectures

The magnetic field coupled architecture has a very low power dissipation and high density. In addition to these advantages they can operate at room temperatures and radiation resistance devices. A nanomagnetic logic has two different arrangements of nanomagnetic architectures embedded into its operation as shown in Fig. 3.4 and Fig. 3.4. In a ferromagnetic coupled devices, as shown in Fig. 3.4, when the cells are clocked to its hard axis and released to settle in its energy minimum, they settle in parallel fashion. Whereas in antiferromagnetic coupling, when the cells are clocked and released from its clocking state, they settle in antiparallel fashion as shown in Fig. 3.4. This wire architecture can be regarded as the interconnect between the logic architectures commonly known as fan-out. The

antiferromagnetic wire architecture can also be used as inverter wire. Where the Binary logic states can be encoded as two meta-stable magnetization states of the magnets with shape anisotropy gives two major stable states as shown in Fig. 3.5.

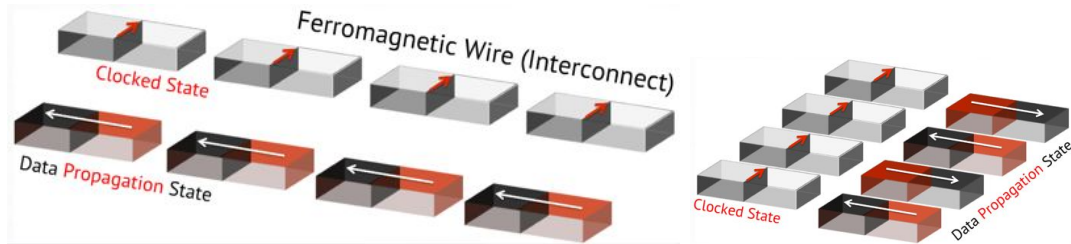


Figure 3.4. Field coupled device architectures. (Top) Ferromagnetic wire architecture. (Bottom) Antiferromagnetic wire architecture.

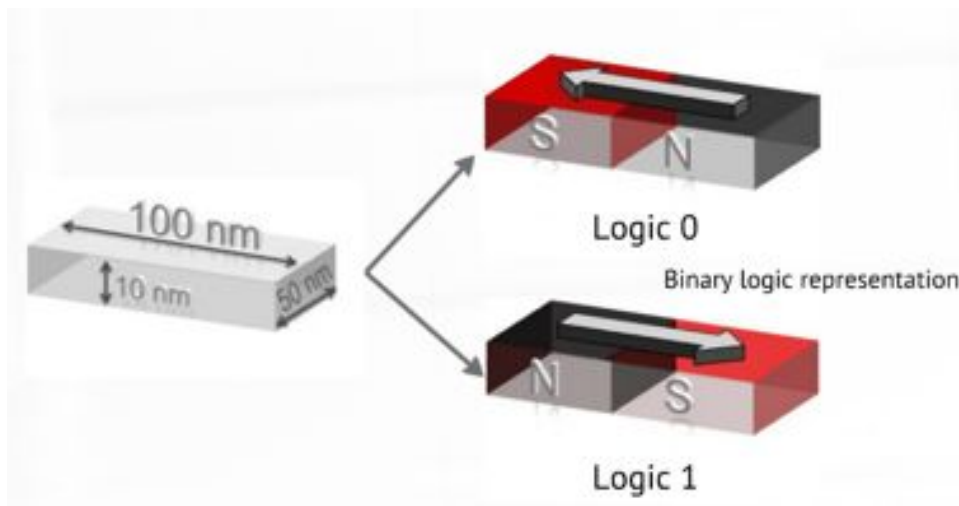


Figure 3.5. Magnetization states encoded as two Binary logic states “0” and “1”

The basic logic gate architecture of an field coupled devices are majority gate architecture proposed by *Imre et al.* shown in Fig.3.6. The majority gate works on finding the majority of the 3-inputs, Fixed, Input A and Input B as shown in Fig. 3.6. The majority gate is capable of performing NAND, NOR and NOT logic operation by setting the inputs of the Fixed magnet to either logic “0” or logic “1” as shown in Fig. 3.7.

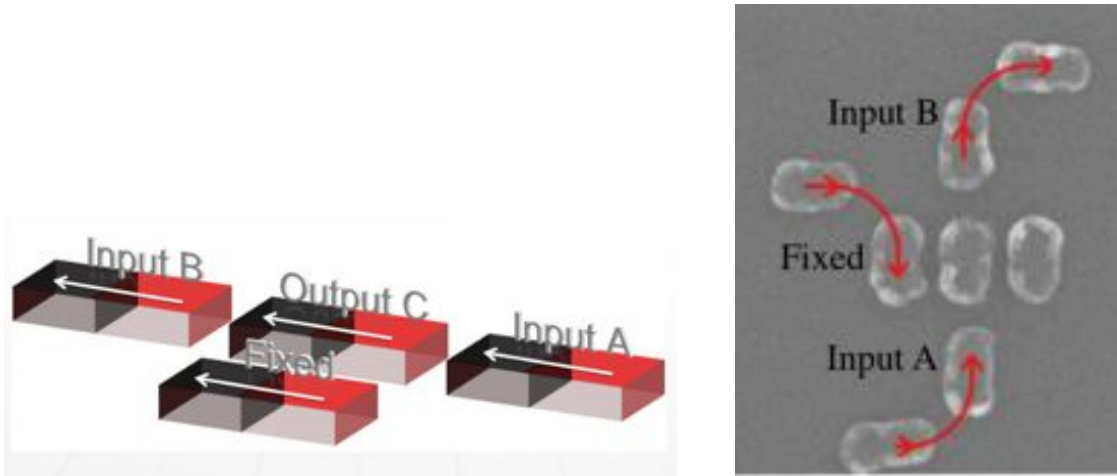


Figure 3.6. Majority gate architecture proposed by *Imre et al.* in [2]. Figure obtained from [2]

Fixed	Input A	Input B	Output C	
0	0	0	0	AND Gate
0	0	1	0	
0	1	0	0	
0	1	1	1	
1	0	0	0	OR Gate
1	0	1	1	
1	1	0	1	
1	1	1	1	

Figure 3.7. Truth table of majority gate architecture that could be operated as AND or OR gates

The magnetic field coupled architecture with the ability of fan-out was demonstrated by *Varga et al.* in [99]. In his experimental demonstration, a fan-out circuit with respect to the direction of the data flow was demonstrated. Later, *Pulecio et al.* demonstrated coplanar crosswires, where he showed overlapping crosswire system, in which the data can be propagated without any interaction in the junction forming between the crosswire systems [100].

CHAPTER 4

BOOLEAN LOGIC COMPUTATION USING MULTILAYER NANOMAGNETS

This work is a leap ahead towards logic in magnetic memory implementation. The work adds the following features in monolayer field coupled magnetic logic: 1) Local spin-torque driven controlled switching, which has been utilized to perform Boolean logic. More specifically, by canting the reference polarizer in the tilted devices to 45° in the X/Z direction. 2) Reading from and writing to the cells using STT current, which provides more controllability over individual cell in logic realization. 3) A novel clocking mechanism, using spin-transfer current instead of conventional field-based clocking mechanism. 4) Low power logical operation, due to magnetization switching induced by spin-torque current, instant-on and rad-hard features of MRAM. 5) We have also found that, though the tilted devices works at a wider range of dimensions and spacing (suitable for flexible CMOS integration), wherein the SyAF devices have inflexible spacing constraints to integrate with underneath CMOS architecture. With this observation, we have to make a selective choice of cell structure depending on the location in the circuits. In addition to these, the structures emulated in this work are fundamental devices for the development of future spintronic elements. A schematic of logic computation hardware is presented in Fig. 4.1.

4.1 Contributions

Magnetic field coupled computing is a promising paradigm, due to room temperature operation, low static power, instant-on feature and interconnect-free approach that does not rely on charge transport. Individual control, clocking and read-out however had to rely

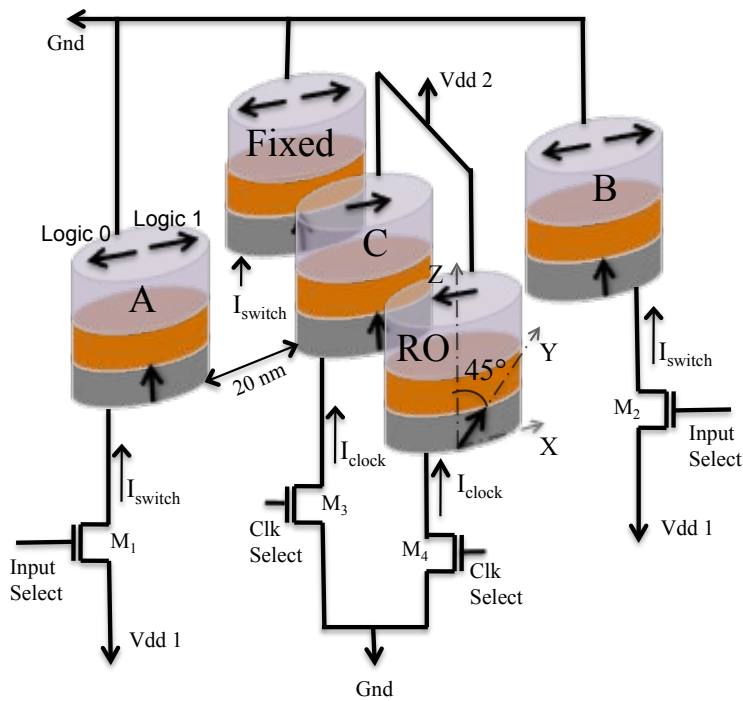


Figure 4.1. Schematic of multilayer majority gate hardware with underneath CMOS devices. The Fixed, A and B are inputs, C is output and RO is the read-out cell which has tilted configuration.

on multi-layer spin-driven magnetic devices, called spin-valve or magnetic tunnel junction. Attractive features of these multi-layer Spintronic structures lie in spin-assisted low power switching, individual control and high signal differentiability's for read-outs. In this chapter, we explore these multi-layer spintronic structures directly for computation such that the computing and access mechanism is homogeneous. This would solve multiple problems of integration, access and power requirements. Based on LLG simulation, we report successful dipolar interaction between adjacent freelayers of multi-layer devices and utilized them to realize Boolean logic functions. This interaction between the multi-layer Spintronic devices unveils new avenues of logic implementation for the future that offers possible solutions to the challenges faced by traditional MQCA realization. We investigate and propose three multi-layer computational elements that can be exploited for logic computation. Spin Valve with free layer possessing in-plane shape and crystalline anisotropy with (i) in-plane Synthetic Anti-Ferromagnetic reference polarizer (as *SyAF devices*), (ii) perpendicular-to-plane polarizer (as *PMA devices*) and (iii) with tilted (45°) reference polarizer (as *TD devices*). The simulated results indicate that SyAF, PMA and TD devices possesses promise to be an excellent candidate for nanomagnetic logic computation. However, the PMA devices suffer from zero resistance readout, the SyAF devices have stringent spacing constraints due to the underneath CMOS architecture, while TD devices is best suitable for writing, clocking and reading the logic state of the cell.

In this work we have

- utilized individual multi-layer spintronic devices, which are robust and are already fabricated separately as single elements are combined into computing elements.
- achieved logic computation using three different elemental multi-layer cells.
- utilized spin torque switching currents to provide different inputs to individual cells.
- utilized spin torque clocking current to clock the output cell for computation.

- maintained the switching current in μA thus improving the switching speed.
- proposed ultrafast and low power computing.

4.2 Introduction

There has been several designs, where researchers have used the dipolar coupling between the single domain nanomagnets for computation [101, 2, 102]. These single-domain magnetic logic devices are controlled by field and require enormous current and also have limited local cell control. These shortcomings led us to investigate an alternative paradigm of spin-torque driven reading, writing and clocking of Magnetic Cellular Automata (MCA) logic computation that offers low power, non-volatile computing. Experimental demonstration with MTJ for nanomagnetic logic with resistance measurement was performed[103]. However, external magnetic fields are used for clocking the cells, which suffer additional power dissipated from the current carrying conductor. Writing to the input cells have been proposed using external and on-chip clocking mechanisms [104, 105]. Recently a new form of computing using the spin injection called “All spin logic device” was proposed[106]. In our multilayer spintronic device, the Binary logic states representation uses the magnetization direction of the free layers regardless of the reference polarizer is shown in Fig. 5.4.

4.3 The In-plane Device Logic Computation

The traditional In-plane MRAM devices has a Barrier/Spacer sandwiched between two ferromagnetic layers PL and FL as shown in Fig. 4.3. We placed two of these devices close to each other ≈ 20 nm, such that their free layers couple with each other as shown in Fig. 4.4. We initialized one of the free layer’s magnetization to its hard axis in +y-direction and released to settle in its energy minimum state. On studying our simulation results, the dipolar interaction between two neighboring In-plane devices indicated the strong anti-ferromagnetic coupling between the pinned layer and the free layer in a single cell that does

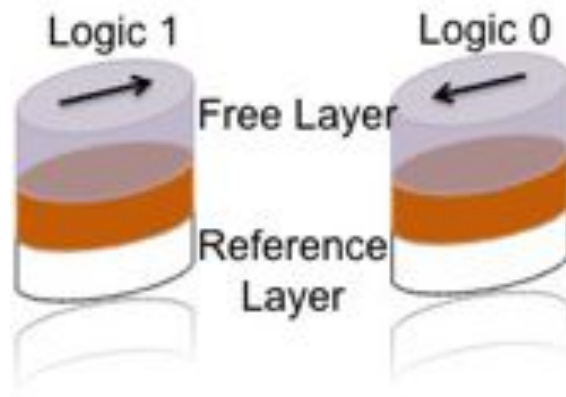


Figure 4.2. MRAM Binary logic representation. The arrows in the free layers indicate their respective magnetization directions.

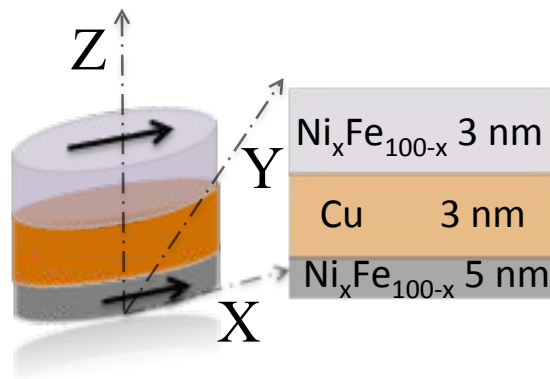


Figure 4.3. Schematic of an In-Plane cell. As one can see the magnetization of free layer and the pinned layer are collinear.

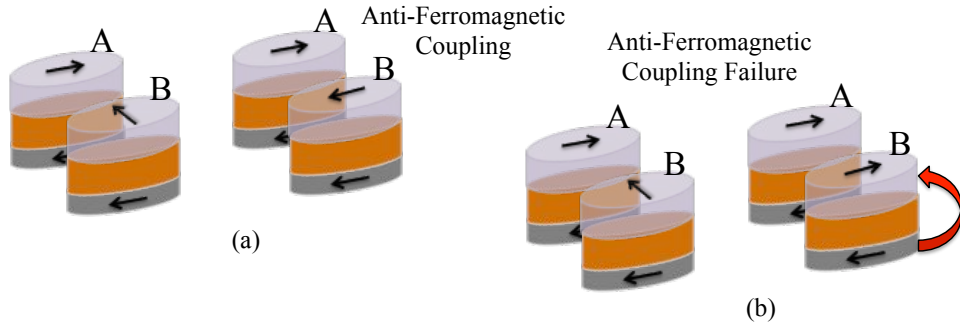


Figure 4.4. Coupling failure in In-plane devices. As one can see the in-plane devices fail to realize dipolar coupling between freelayers due to strong inter-layer coupling between the PL and FL layers.

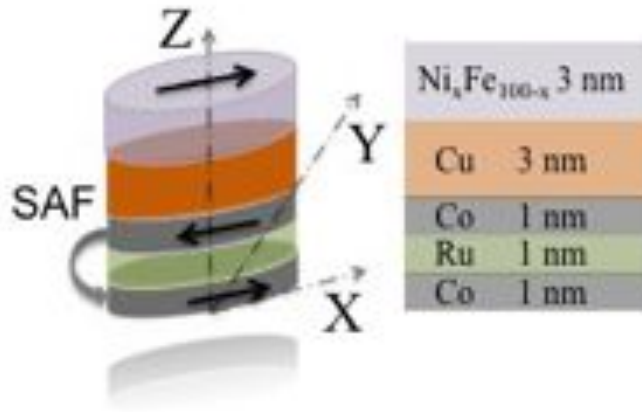


Figure 4.5. Schematic of an SyAF Cell. The magnetization of free layer and the AF pinned layer are collinear.

not allow neighbor interaction between the neighboring cells to decide the final state of the clocked cell as shown in Fig. 4.4. We performed the experiments with different thickness of the free layer, pinned layer and spacing between the devices, but in any of these instances the dipolar coupling between the neighboring free layers were not strong enough to overcome the coupling between the FL and PL. Thereby, In-plane devices failed to realize dipolar coupling ruling out their possibility of involvement in magnetic field coupled computing realization.

4.4 The SyAF Device Logic Computation

We then utilized SyAF devices due to their reduced magneto-static coupling between the free layer and pinned layer and its robustness. From literature we found that, there had been similar magnetostatic coupling problem with the PL and FL layers that led the MRAM memory community to introduce the SyAF devices. We have incorporated the magnetic properties shown in Table. 4.1 for SyAF structures into our model to achieve computation using the majority gate architecture is shown in Fig. 4.6. The majority gate architecture is already discussed in Chapter. 3.4. Fig. 4.7 shows the majority gate architecture and the final magnetization state of the free layer representing majority-OR logic implementation. As one can see from Fig. 4.8, the normalized magnetization vectors m_x , m_y and m_z of the free layer of output cell “C” settles in +x-direction (C=1) which is the logic output when the inputs are Fixed=1, A=1 and B=0.

Table 4.1. Input materials (Permalloy and Cobalt) magnetic parameters used for simulations.

Material Parameters	NiFe	Co
Saturation Magnetization $M_s(emu/cm^3)$	800	1414
Uniaxial Anisotropy $K_{u2}(erg/cm^3)$	$1E^3$	$4E^6$
Exchange Coupling $A(erg/cm)$	1.050	3.050
Exchange Stiffness between cells $A_{IJ}(uerg/cm)$	1.050	3.050
Resistivity $Rho(u - ohm/cm)$	15.000	5.800
Bilinear exchange across Co/Ru/Co in SyAF	0.018	

We have implemented Logic-OR, Logic-AND and Logic-NOT using SyAF devices and one can see from the magnetization graph shown in Fig. 4.8 there is no influence of the pinned layer with the free layer as the magnetization vectors m_y and m_z goes to zero. The magnetization state vectors for all the inputs for SyAF devices are verified. These SyAF devices require very high switching current in the order of 3 mA to overcome the antiferromagnetic coupling and for clocking, magnetic-electrical interface design was proposed[107], which uses an off-chip magnetic field to clock the nanomagnets. Moreover, we found that in order to utilize dipolar coupling, these devices have stringent spacing constraints (≤ 15 nm).

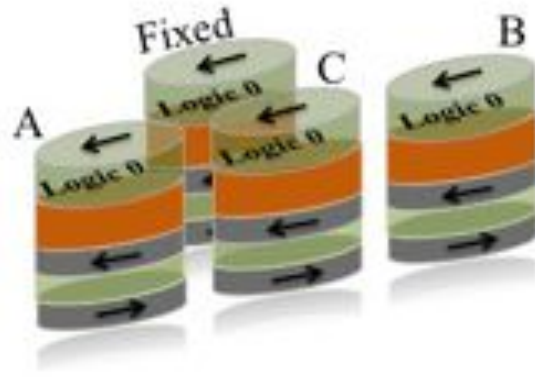


Figure 4.6. Schematic of OR logic implementation using SyAF devices. SyAF device placement and magnetic alignment at $t = T_{final}$

So, in order for these devices to be used as coupled computation devices, they have to be placed much closer to each other. This would lay tremendous dimensional constraints to the underneath CMOS architecture for clocking and switching these computation elements.

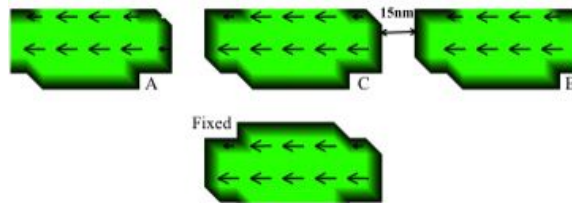


Figure 4.7. LLG simulation of SyAF OR logic implementation. The magnetization and domains of the free layer of device C settles to logic 0 at $t = T_{final}$ respectively when the inputs are $A = 0$ and $B = 0$.

4.5 The Perpendicular Device Logic Computation

The limitations with In-plane and SyAF device computation advanced our design in using Perpendicular Multilayer Anisotropy (PMA) shown in Fig. 4.9. Where the PL has its crystalline anisotropy pointing out-of-plane, which does not couple with the free layer and allows the free layer in turn to couple with its neighboring free layer. We successfully

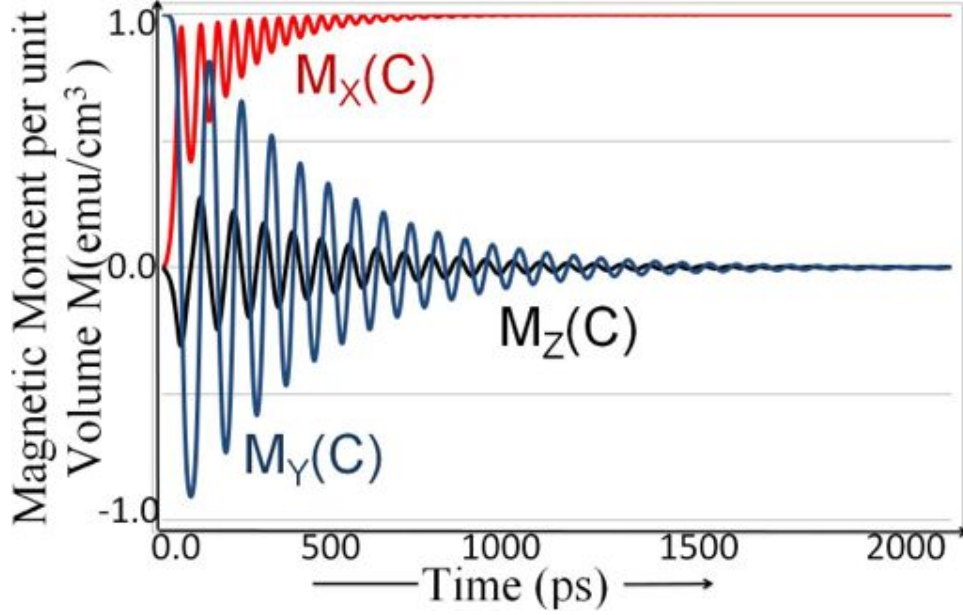


Figure 4.8. Magnetization state vector of logic output. The inputs for the logic operation is, Fixed=1,A=0 and B=1. The output settles to C=1.

implemented AND, OR and NOT gates using PMA devices. The devices have a distinctive in-plane crystalline anisotropy in their free layers; along with their shape anisotropy gives the layers a definitive easy axis along the x-direction, which gives us a method to realize logic functions. The PMA device structure with the choice of materials is shown in Fig. 4.9.

However, for reading the magnetization value through TMR, we would require at least some component of In-plane magnetization to be incorporated in the device structure. The current to switch the magnetization was in the order of $\approx 5mA$. In addition, PMA device structures suffer from resistance read-out between its logic states “0” and “1” as there is no out-of plane magnetization in the free layer and hence the inability to read the state of the output cells using the readout schemes. Using different architectures as output cells[108] would result in inhomogeneous logic computation. Hence, a novel device element that could prevent these shortcomings would be necessary and is presented in the next section.

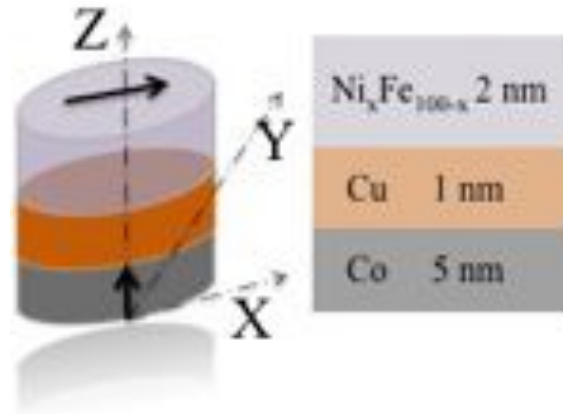


Figure 4.9. Schematic of an PMA cell. The free layer easy axis is along x and reference layer is along z.

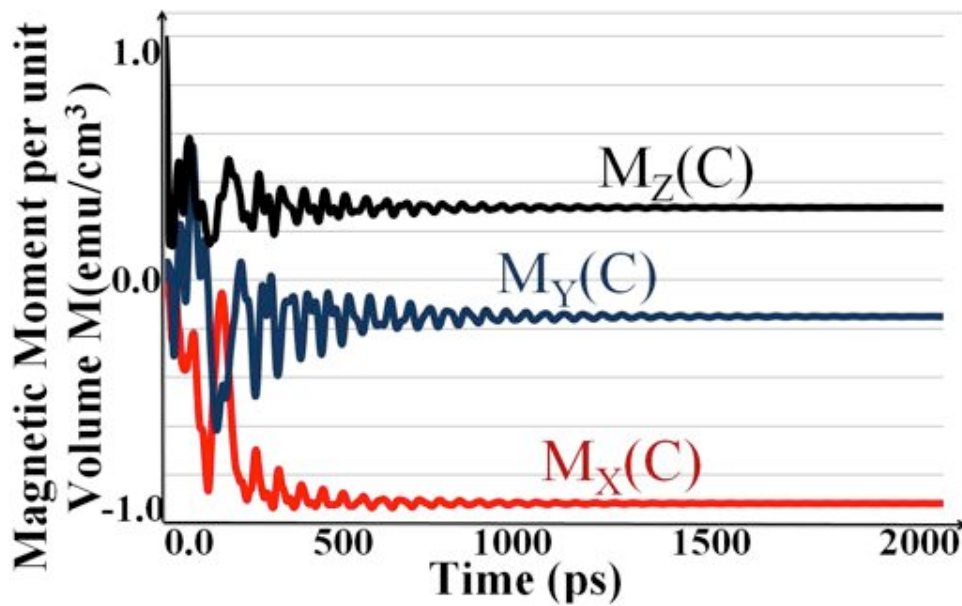


Figure 4.10. Magnetization vectors of AND gate operation. The free layer magnetization graph of an AND gate with inputs $A=1$ and $B=0$, where the output cell C settles to 0(-1)

4.6 The Tilted Device Logic Computation with Clocking and Switching Capabilities

In this section, we present the possibility of logic computation using tilted polarizer wherein, the bottom polarizer was canted at 45° in the X/Z axis, as shown in Fig. 4.11.

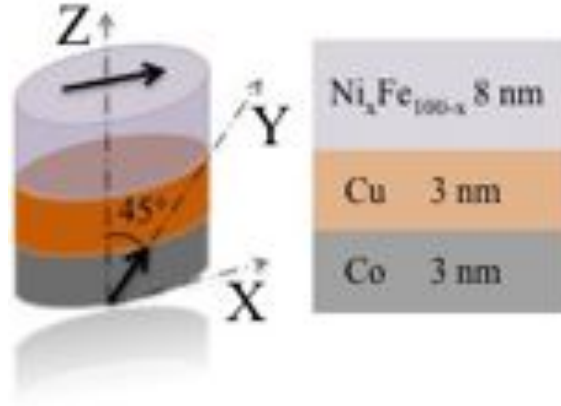


Figure 4.11. Schematic of an TD cell. The reference layer is aligned 45° to x and z axis.

4.6.1 Micromagnetic Model Parameters

The Landau-Lifshitz-Gilbert equation of motion for a free layer that includes the spin polarized induced torque is given by,

$$\frac{d\hat{m}}{dt} = -\gamma\hat{m} \times H_{eff} + \alpha\hat{m} \times \frac{d\hat{m}}{dt} + \frac{\gamma\hbar\eta(\varphi)J}{2\mu_o M_s e d} \hat{m} \times (\hat{m} \times \hat{m}_p) \quad (4.1)$$

where \hat{m} and \hat{m}_p are unit vector of free layer and pinned layer magnetization, γ is gyrometric ratio, μ_o magnetic vacuum permeability. The second term on the right hand side is the Gilbert damping term and α is the damping parameter ($\alpha \ll 1$), the effective field from bottom layer, H_d , the demagnetization field, H_{dm} . The last term represents the spin torque, \hbar is the reduced Planck constant, d is the free layer thickness and e is electron charge.

The input switching initiates with the magnetization vector starting from +y-direction with initial spin-torque current through PL. With more spin torque current the input switches to “0” (-1) from “1”.

A single-domain multilayer model with *tilted* reference layer was developed in LLG Micromagnetic simulator[92]. The time evolution of \hat{m} unit vector along the free layer is found from Eq.4.1. For the results presented here for an elliptical lateral device 50 x 25 nm², a

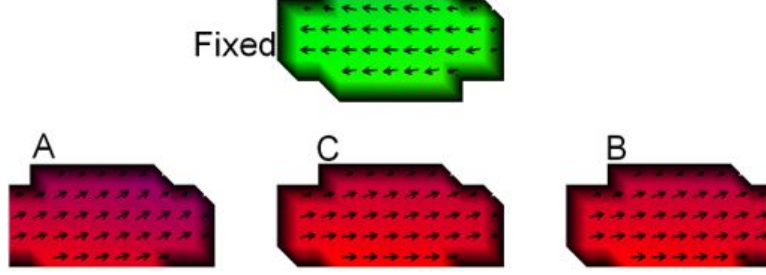


Figure 4.12. Initial magnetization state of free layer of input cell to be switched from $A=1$ to $A=0$ at $t=T_{Initial}$

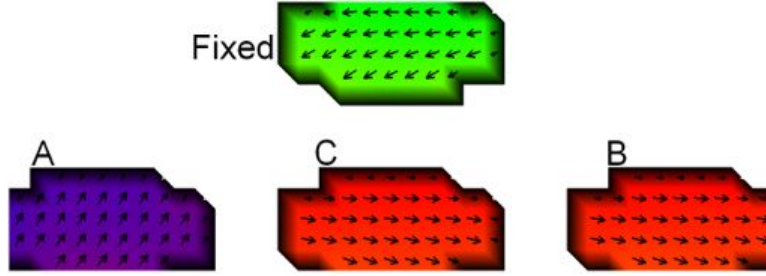


Figure 4.13. Intermediate magnetization state of free layer of input cell to be switched from $A=1$ to $A=0$ at $t=T_{Intermediate}$

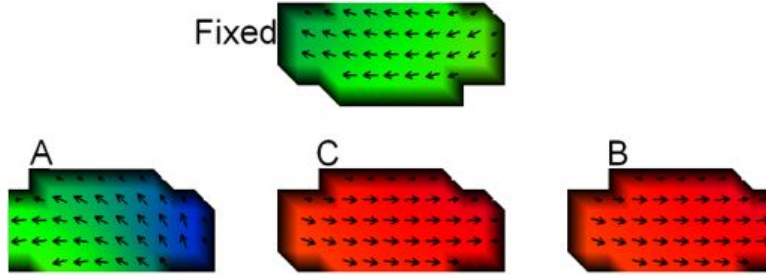


Figure 4.14. Final magnetization state of free layer of input cell switched to $A=0$ from $A=1$ at $t=T_{Final}$

Co/Cu/NiFe tilted polarizer system and cell dimension was at $5 \times 5 \times 4.6 \text{ nm}^3$. The spacing between TD devices was 20 nm . The material parameters used for *Co*: $M_s = 1414 \text{ emu/cm}^3$, $A = 3.050 \text{ } \mu\text{-erg/cm}$, $\rho = 5.8 \text{ } \mu\text{-ohm-cm}$, magnetocrystalline uniaxial anisotropy = $4e6 \text{ erg/cm}^3$ in z-axis. The ρ for barrier layer *Cu* is set to $1.68e-8 \text{ ohm-m}$. For Ni_xFe_{100-x} are: $M_s = 800 \text{ emu/cm}^3$, $A = 1.050 \text{ } \mu\text{-erg/cm}$, $\rho = 15 \text{ } \mu\text{-ohm-cm}$, magnetocrystalline uniaxial anisotropy = 1000 erg/cm^3 in x-axis. The damping (α) and gamma(γ) was taken as 0.02

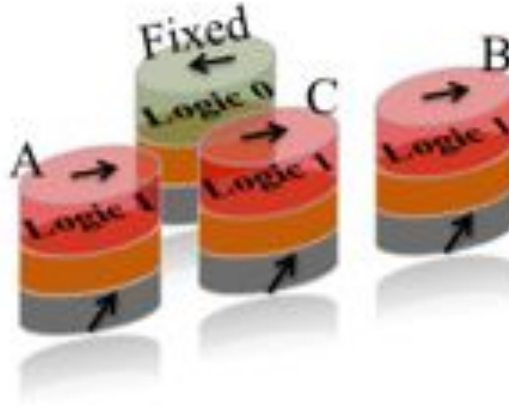


Figure 4.15. Intermediate switching input state for tilted multilayer cell. Switching inputs with Spin-Torque induced current in Tilted polarizer. At $T_{Intermediate}$

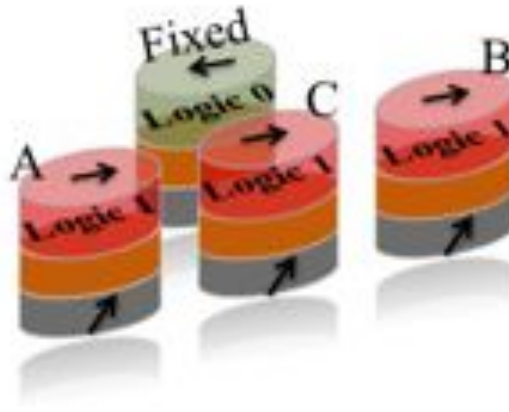


Figure 4.16. Magnetic alignment for tilted polarizer. Switching inputs with Spin-Torque induced current in Tilted polarizer. TD device placement and magnetic alignment

and 17.6 MHz respectively and $P = 0.54$. By using suitable pinning fields the reference layers were tilted to 45° in X/Z axis. The input logic states A, B and Fixed for computation were assigned by applying switching spin torque current to the cells as shown in Fig. 4.6.1. The output device C was initially clocked to $+y$ -direction by passing the spin torque clocking current of $300\mu A$ shown in Fig. 4.17 and released at start of simulation for it to compute the appropriate logic. We have used average torque as exit criteria and Predictor-Corrector algorithm with time integral for 3D complex FFT method in our simulation.

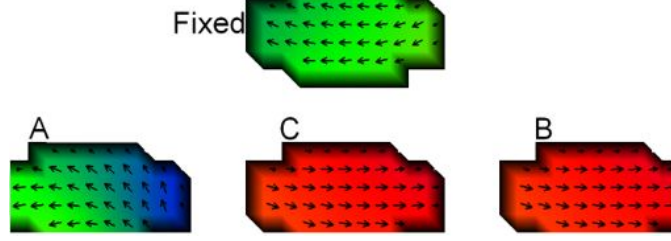


Figure 4.17. Final state of input switching using tilted polarizer. Switching inputs with Spin-Torque induced current in Tilted polarizer. Switched input cell A to 0 at $t=T_{final}$

4.6.2 Impact of Device Parameters on Writing and Clocking Tilted Devices

For a multi-layer structure with tilted-polarizer, the clocking was induced by injecting spin-polarized current to switch the magnetization of the cell to y-axis. The coupling from the bottom pinned reference layer was also included in the simulation.

From Eq.4.1 effective field H_d is added to the H_{eff} where H_d is given by,

$$H_d = -H_d\alpha_p\hat{e}_x + H_d\gamma_p\hat{e}_z \quad (4.2)$$

where e_x and e_z are the unit vector in the direction of magnetization of the pinned layer and α_p, γ_p are its respective direction cosines. The H_{eff} is given as[109],

$$H_{eff} = H + H_A + H_d + H_{dm} \quad (4.3)$$

where in our model, H is the external field is *zero*, H_{dm} is the demagnetization field. The presence of e_x and e_z component in the pinned layer leads to a large demagnetization field which forces the magnetization vector of the free layer to precess about the direction normal to the plane. The rate of precession is determined by the demagnetization field which reaches maximum ($\approx 4\pi M$) when the layer magnetization is in precession in $+y$ -direction is given by $H_{dm} = -4\pi \cdot M_y \cdot \hat{e}_y$. The in-plane uniaxial anisotropy field $H_A = 0$ when the layer is clocked in $+y$. The magnetization distribution within the layer becomes a vector field, and is given as,

$$M(r) = M_s \cdot |m(r)| \quad (4.4)$$

due to the magnetization pop-up to out-of-plane from the influence of the bottom pinned layer, the constraint $|m(r)|=1$, which leads to,

$$M(r) = M_s \quad (4.5)$$

in clocked state,

$$M_y = M_s, \quad (4.6a)$$

$$M_x = M_z = 0, \quad (4.6b)$$

$$M \times (M \times M_p) \approx M_x e_x + M_z e_z \quad (4.6c)$$

in a stationary steady state $dm/dt = 0$, therefore during clocking Eq.4.1 becomes,

$$\gamma M_s \hat{m} \times h_{eff} = \frac{\gamma \hbar \eta(\varphi) J}{2\mu_o M_s e d} \hat{m} \times (\hat{m} \times \hat{m}_p) \quad (4.7)$$

where,

$$H_{eff} = M_s \times h_{eff}, \quad (4.8a)$$

$$h_{eff} = \frac{1}{M_s} [-H_x \hat{e}_x + H_z \hat{e}_z + -4\pi M_s \hat{e}_y], \quad (4.8b)$$

$$m = \frac{M}{M_s} = \hat{e}_y \quad (4.8c)$$

which solves,

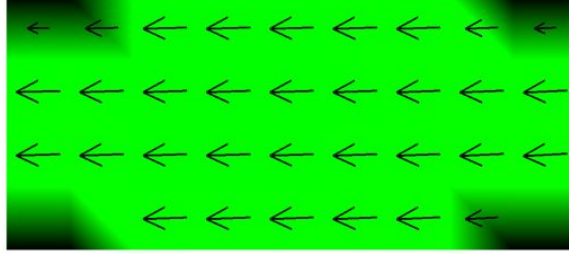


Figure 4.18. Initial state of spin-torque clocking with tilted polarizer at time= $T_{initial}$



Figure 4.19. Intermediate magnetization state of clocked cell with tilted polarizer

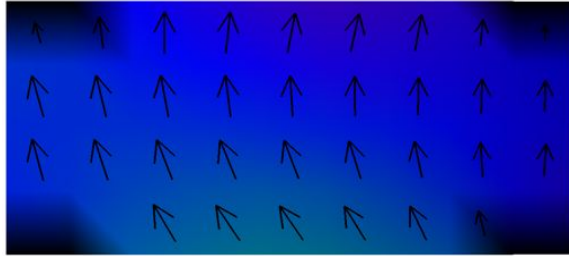


Figure 4.20. Final magnetization state of clocked cell in $+y$ -axis at time= T_{final}

$$H_x e_z + \gamma H_z e_x = M_y a_1 \hat{m} \times (\hat{m} \times \hat{m}_p) \quad (4.9)$$

Here,

$$a_1 = \frac{\gamma \hbar \eta(\varphi) J}{2\mu_o M_s e d} \quad (4.10)$$

Equating the above equation for direction cosines e_x and e_z for tilted polarizer, we could see $\alpha_p = \gamma_p$, which substantiates that the bottom polarizer should be canted in 45° in its XZ axis switches the device to a clocked state $+y$ which is shown in simulation Fig. 4.21.

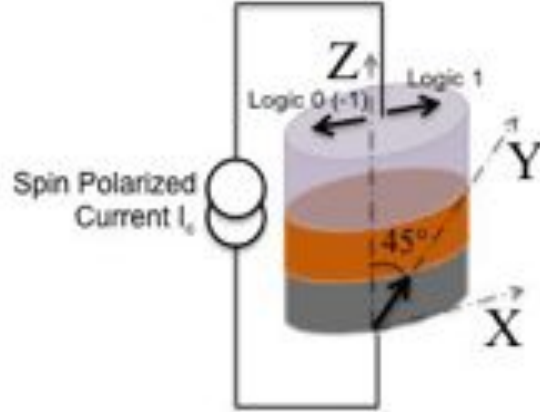


Figure 4.21. Applying spin torque current to switch the magnetization of the TD devices

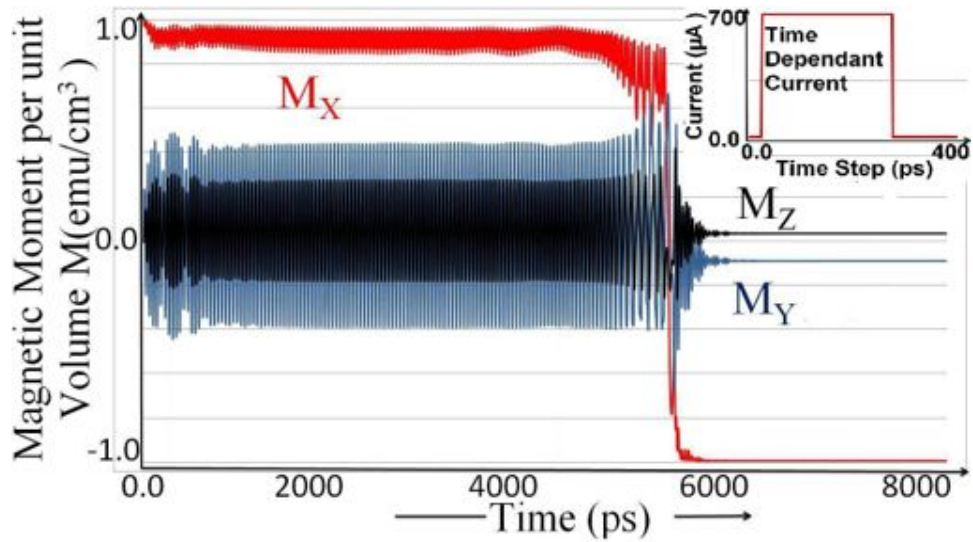


Figure 4.22. Spin torque current induced switching for TD devices. Magnetization switching curve from P (logic “1”) to AP (logic “0”)

The current induced switching magnetization curve is shown in Fig. 4.21. We used 2D Slonczewski Spin Polarized perpendicular to plane current of $700\mu\text{A}$ with a time step of 1ps in 5 intervals; the interval step was 25ps , 1ps , 250ps , 1ps and 123ps .

Table 4.2. Comparison of SyAF, PMA and TD computing structures.

Structures →	SyAF		PMA		TD	
Polarizer	InPlane x-direction	in	Out of Plane z-direction	in	45° in the XZ axis	
Switching Time	2.5ns		$\approx 50ps$		$\approx 20ps$	
Switching Current	$\approx 3 - 5mA$		$\leq 5mA$		$\approx 200 - 700\mu A$	
Clocking Current	Off-chip magnetic field	mag-	Cannot clocked PMA	be with	$\approx 300 - 400\mu A$ in +y	
Device Spacing to achieve coupling	$\leq 15nm$		20nm		20nm	
Logic Operation tested	<i>AND</i> , <i>NOT</i>	<i>OR</i> ,	<i>AND</i> , <i>NOT</i>	<i>OR</i> ,	<i>AND</i> ,	<i>OR</i> , <i>NOT</i>

4.7 Results and Discussion

Boolean AND, OR and Inverter operations were successfully achieved for all inputs with multi-layer stacks utilizing dipolar interaction among neighboring spintronic devices for SyAF, PMA and TD devices for which the magnetization graph results for the OR and AND logic operation for TD devices are presented in Fig. 4.23. Looking at the magnetization dynamics obtained for all inputs from the continuously varying in-plane x-axis magnetization vector, one can see the state of output cell (C) exhibiting a favorable OR logic gate operation with respect to inputs. We have also verified AND and Inverter operations for all inputs. Successful implementation of logic using Spintronic devices therefore heralds the onset of a new era in logic computation.

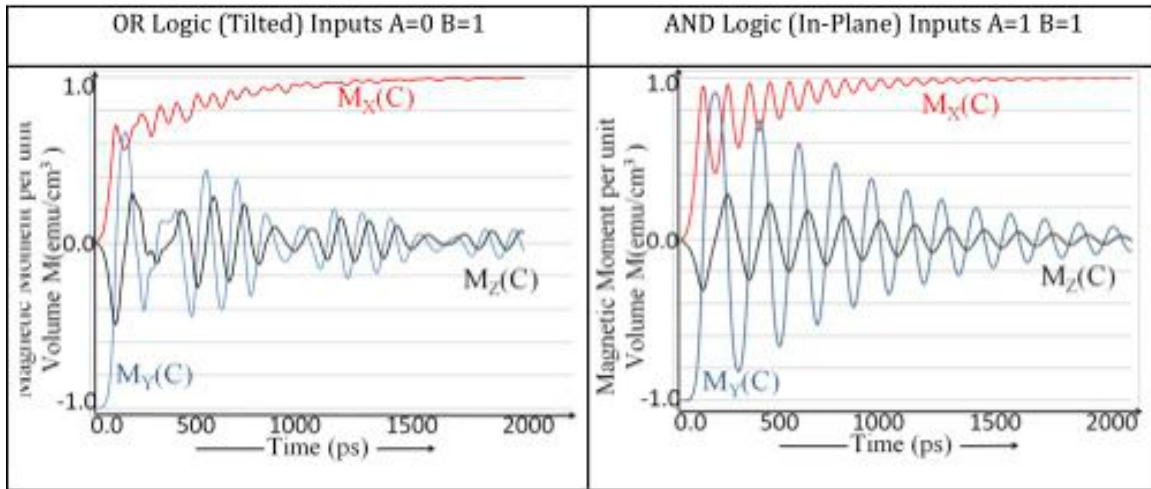


Figure 4.23. Magnetization graphs of output cell (C) for AND and OR logic operations for tilted devices.

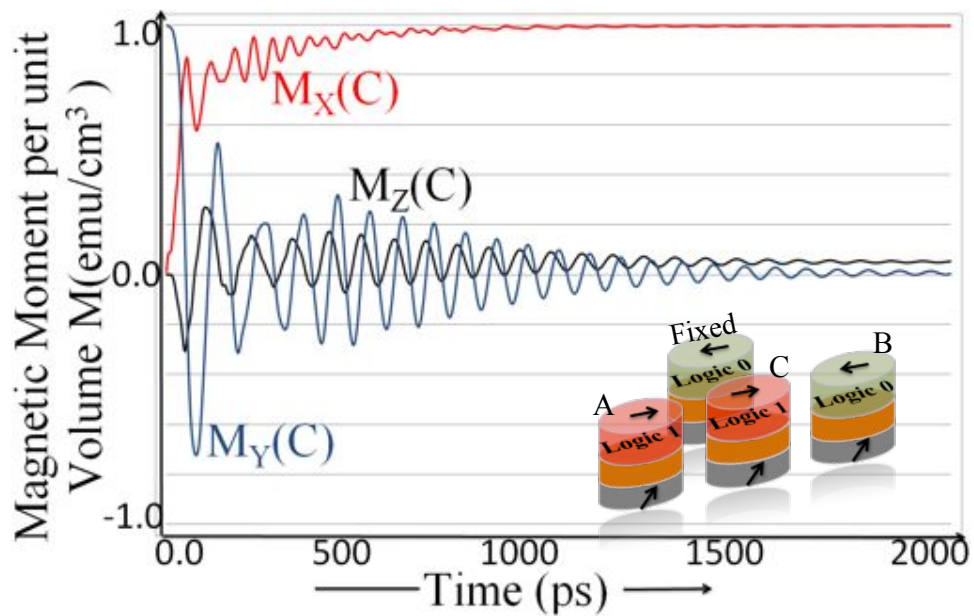


Figure 4.24. Normalized magnetization graph of output cell (C) for different OR gate inputs Fixed = 0, A = 1 and B = 0. The output cell C = 1 verifying OR gate operation.

CHAPTER 5

STUDY OF NEIGHBOR INTERACTION BETWEEN NANOMAGNETIC DISKS

The study investigates the effect of magnetic neighbor interaction on the state behavior of nano-magnetic disks for data storage and computation applications. We have observed and verified that a nano-magnetic disk, with certain dimension, can exist either in the SDS or VS depending on the edge-to-edge spacing between the nano-magnetic disks. The experiments were conducted by varying the diameters and thicknesses with respect to edge-to-edge spacing. The dimensions were based on the phase diagram between the single domain state and the vortex state. We have observed nano-magnetic disks spaced far apart from its neighbor, settled in the vortex state and coupled nano-magnetic disks with less spacing settled in the single domain state. This phenomenon was observed for nano-magnetic disks with thickness between 8 nm to 20 nm and diameters between 80 nm to 140 nm. Results from this chapter have been previous published in IEEE Transactions on Magnetism [110]¹

5.1 Introduction

For the past few decades single-domain nano-magnetic disks have been actively explored as computing elements [111, 112, 4, 113, 104, 114] and as data storage devices [115, 116, 117], as it exhibits several new and interesting characteristics. As a result, there were various experimental and theoretical studies on coupled and isolated nano-magnetic disks [118, 119, 120]. Here, we report the observations in a coupled nano-magnetic system, where a disk can exist in the single domain state or the vortex state depending on the strength of its

¹©2013 IEEE. The permission from IEEE is included in Appendix A.

neighboring interactions. We have verified this by simulation and directly fabricating pairs of nano-magnetic disks with different edge-to-edge spacing's. Earlier works have reported the phase diagrams between the single domain state and the vortex state as a function of diameter and thickness for isolated nano-magnetic disks [101, 121, 122]. For instance Cowburn *et al.* have fabricated isolated nano-magnetic disks of diameters ranging from 55 nm to 500 nm and thickness ranging from 6 nm to 15 nm, and experimentally identified a phase plot between SDS and VS. Also, Jubert *et al.* and Hoffmann *et al.* have reported on the phase boundaries between the single domain state and the vortex state for isolated nano-magnetic disks. Bennett *et al.* [123] have shown magnetostatic interactions in planar arrays for only the single domain state nano-magnetic disks with 50 nm in diameter and 10 nm in thickness. Kumari *et al.* [3] have reported a phase diagram as a function of disk diameter and thickness for coupled nano-magnetic disks with a constant edge-to-edge spacing of 20 nm. We have selected the dimensions of the nanomagnetic disks in the single domain state region and regardless of the spacing between the nanomagnetic disks; the final ground state is always single domain state due to its dimensions. This was verified by simulating a pair of nanomagnetic disks separated by a distance of ≥ 200 nm. The nanomagnets were clocked to its hard axis (Z-direction) and released to settle in its energy minimum. The final state of the nanomagnetic disk settles in single domain state as shown in Fig. 5.2.

We have performed similar simulation for nanomagnetic disks in vortex state region. The dimension of the disk was chosen with thickness $T \geq 20$ nm and diameter $D \geq 200$ nm. Regardless of the spacing between the nanomagnetic disks, the magnets settle in vortex states shown in Fig. 5.3. Our region of interest is in the boundary between SDS and VS in Fig. 5.1.

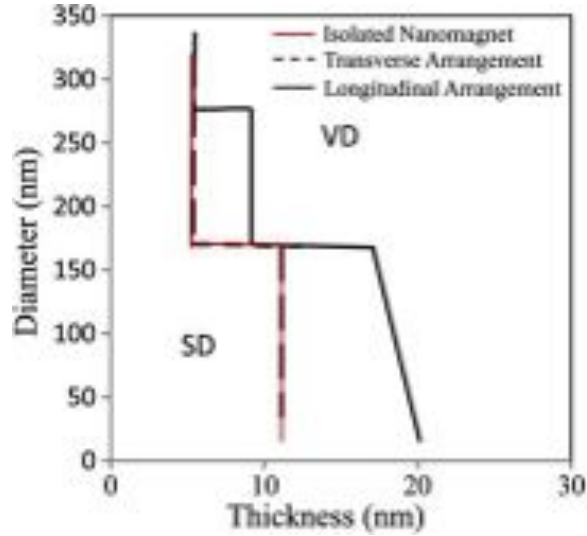


Figure 5.1. Phase diagram of single domain state and vortex state. A circular nano disk with different thickness and diameter (Obtained from [3])

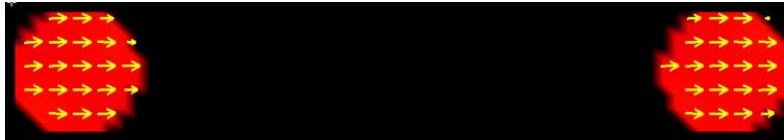


Figure 5.2. Single domain state nanomagnetic disks with dimensions in the SDS region selected from [3]

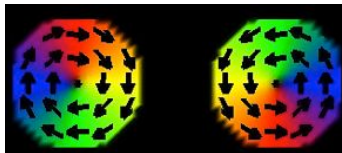


Figure 5.3. Vortex state nanomagnetic disk with thickness ≥ 20 nm with dimensions in the VS region selected from [3]

5.2 Contribution

We have chosen the dimensions for the nano-magnetic disk near the phase boundary in the vortex state region and studied the dipolar neighbor interaction between the nano-magnetic disks. There are two possible stable states for a circular nano-magnetic disk with

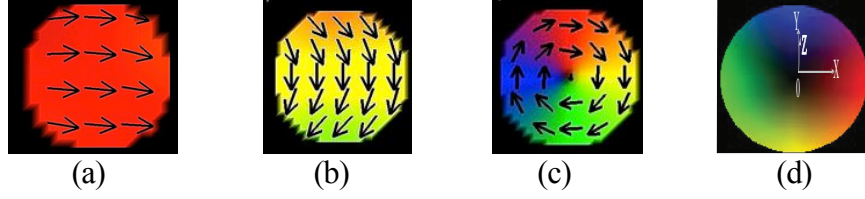


Figure 5.4. Magnetization states representation of a nano-disk. (a) Single domain state where the domains are aligned in one direction. (b) C-State, where the domains are in curling fashion (c) Vortex state where the domains are arranged in a curling shape and the center is at the aperture. (d) Legend explaining the color representation for domains and their associated magnetic directions when simulated using LLG simulation suite. All domains are color coded as follows: red if they are aligned in \hat{x} and blue if they are aligned in \hat{y} and green if aligned $-\hat{x}$ and yellow if aligned $-\hat{y}$.

an intermediate transition state known as the C-state. One of its states is the single domain state, where all the spins align in one direction as shown in Fig. 5.4(a). Second is the vortex state, where the magnetization curls in the plane of the disk as shown in Fig. 5.4(b). In our study, we have investigated the magnetization states of coupled nano-magnetic disks with varying diameters, thicknesses and edge-to-edge spacing's. Fig. 5.5 shows the interaction (coupling) energy curve between the nano-magnetic disks with 110 nm in diameter and 10 nm in thickness under conditions of changing edge-to-edge spacing. As expected (see Fig. 5.5), when the interaction energy decreases gradually, the nano-magnetic disks with closer edge-to-edge spacing settle in the single domain state, whereas disks with larger separation settle in the vortex state. In our study the vortex states are considered to be non-interacting with respect to the condition, $d \geq 2D$ [124] where, d is the edge-to-edge spacing between the disks and D is the diameter of the nano-magnetic disk.

This study examined the unique contribution of the following conclusions to a nano-magnetic disk:

- A nano-magnetic disk can exist either in the SDS or VS depending on the edge-to-edge spacing between the neighboring magnets.

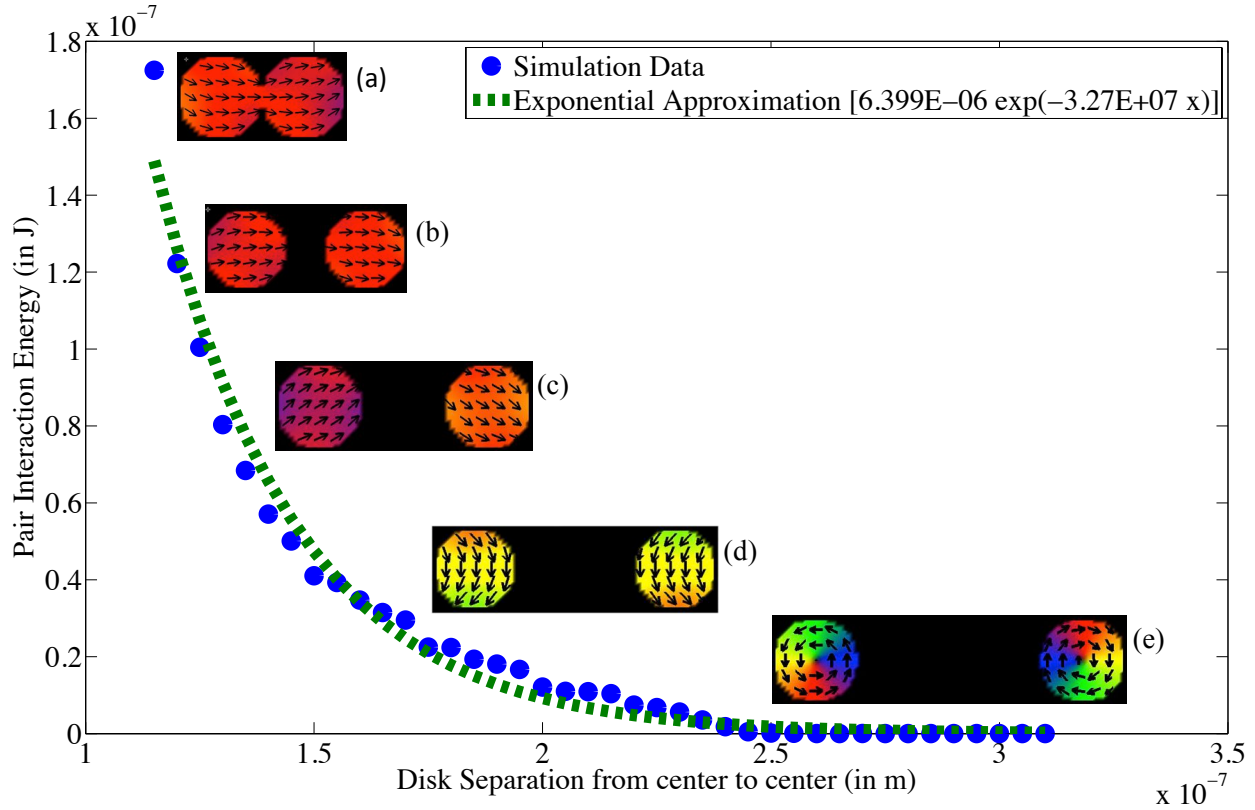


Figure 5.5. Pair interaction energy between disks by varying the edge-to-edge spacing.

- As the diameters of the nano-magnetic disks increases, the probability of the vortex state increases and thereby the coupling energy is minimum. Due to a very low coupling energy between the disks the vortex states are preferred even for this smaller edge-to-edge spacing.
- As the thicknesses of the nano-magnetic disks increases, the vortex state transition is preferred at large edge-to-edge spacing.

The simulation results were validated by fabricating pairs of nano-magnetic disks with an average diameter of 110 nm, an average thickness of 10 nm and varying edge-to-edge spacing from 20 nm to 260 nm. The magnetic force micrograph (MFM) of the nano-magnetic disks

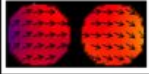





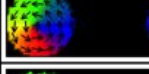







Edge-to-Edge Spacing	Simulation	MFM
20 nm		
60 nm		
100 nm		
120 nm		
160 nm		
180 nm		
240 nm		

Figure 5.6. Verification of the single domain state and the vortex state using MFM micrographs. The simulation results with MFM micrographs of Permalloy ($Ni_{80}Fe_{20}$) nano-magnetic disk pairs fabricated with diameter $D = 110$ nm and thickness 10 nm for different spacing's. MFM micrographs are generated by *D K Karunaratne, USF*

verifies the observations of the simulated experiment results (shown in Fig. 5.6) that the single domain state or the vortex state could exist for similar nano-magnetic disks.

To our knowledge, this is the first work to report the observation of a nano-magnet, with appropriate geometry, can exist the single domain state or the vortex state depending on the neighborhood coupling.

5.3 Micromagnetic Model

The magnetization dynamics of coupled nano-magnetic disks were investigated using Landau-Lifshitz-Gilbert (LLG) Micromagnetic solver [92]. The solver has been extensively used for characterizing micromagnetic structure and dynamics [125, 126]. To calculate the magnetic microstructure in ferromagnets, the time evolution of a magnetization configuration

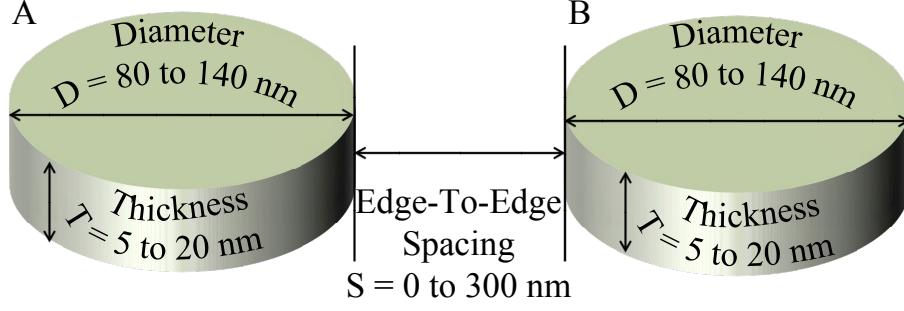


Figure 5.7. Schematic of experiment conducted by varying the diameters D , thicknesses T and edge-to-edge spacing S .

inside a ferromagnet, which is described by the Landau-Lifshitz-Gilbert equation, must be solved. This equation has the following form.

$$\frac{d\tilde{\mathbf{M}}}{dt} = -\frac{\gamma}{1+\alpha^2}\tilde{\mathbf{M}} \times \tilde{\mathbf{H}}_{\text{eff}} - \frac{\gamma\alpha}{(1+\alpha^2)M_s}\tilde{\mathbf{M}} \times (\tilde{\mathbf{M}} \times \tilde{\mathbf{H}}_{\text{eff}}) \quad (5.1)$$

where γ is the gyromagnetic ratio, $\tilde{\mathbf{M}}$ is magnetization vector of the disk, $\tilde{\mathbf{H}}_{\text{eff}}$ is effective magnetic field, α is intrinsic damping constant and M_s is saturation magnetization.

The observation that similar nanodisks can exist either in the single domain state or the vortex state that is dependent on the change in edge-to-edge spacing can be related to the continuous change in effective field H_{eff} of the system, which is determined by differentiating the system total energy E_{total} with the saturation magnetization.

In micromagnetics, the effect of different energy terms on the magnetization vector is represented by the term H_{eff} , which is given as,

$$H_{\text{eff}} = H_{\text{exch}} + H_{\text{demag}} + H_{\text{zeeman}} \quad (5.2)$$

$$H_{\text{eff}} = \frac{-\delta E_{\text{total}}}{\delta(M_s \hat{\alpha})} \quad (5.3)$$

At equilibrium, the total energy of a nano-magnetic element is given by,

$$H_{exch} = \frac{2A_{exch}}{M_s^2} \Delta^2 M \quad (5.4)$$

$$E_{total} = E_{demag} + E_{interaction} \quad (5.5)$$

$$E_{demag} = \frac{1}{2} \mu_0 V M H_{demag} \quad (5.6)$$

$$E_{interaction} = \frac{1}{2} \mu_0 V M H_{interaction} \quad (5.7)$$

where A_{exch} is the exchange stiffness, V is the volume of the nano-magnet, demagnetization energy E_{demag} depends on the shape of the dot and the $E_{interaction}$ is the energy term coming from the interaction with neighboring dots [104] and E_{zeeman} is zero.

$$H_{eff} = D_i M + \sum_{neighbors} C_i M \quad (5.8)$$

where the term D_i is the demag tensor of the i^{th} nano-magnet dependent on the shape of the nano-magnet and C_i is the interaction (coupling) tensor of the i^{th} nano-magnet which is the sum of all the $E_{interaction}$ energy from all its neighbors.

We have used a 3D-compatible correction method for micromagnetics of curved geometries discretization as shown in [127]. Comparison between the 2D and 3D discretization are identical for all disks. The unit element size is 4.72 nm x 4.72 nm x T/2 nm, where T is the thickness of the disks. Decreasing the element size did not influence the results. We have used Time based relaxation method, which is rotating the magnetization with respect to the effective field vector. The simulations incorporated predictor corrector integrator that yields most accurate results with damping factor $\alpha \sim 0.01$ and a convergence value of 1×10^{-4} for exiting the calculation. We used a free electron gyromagnetic frequency γ to be 17.6 Mhz

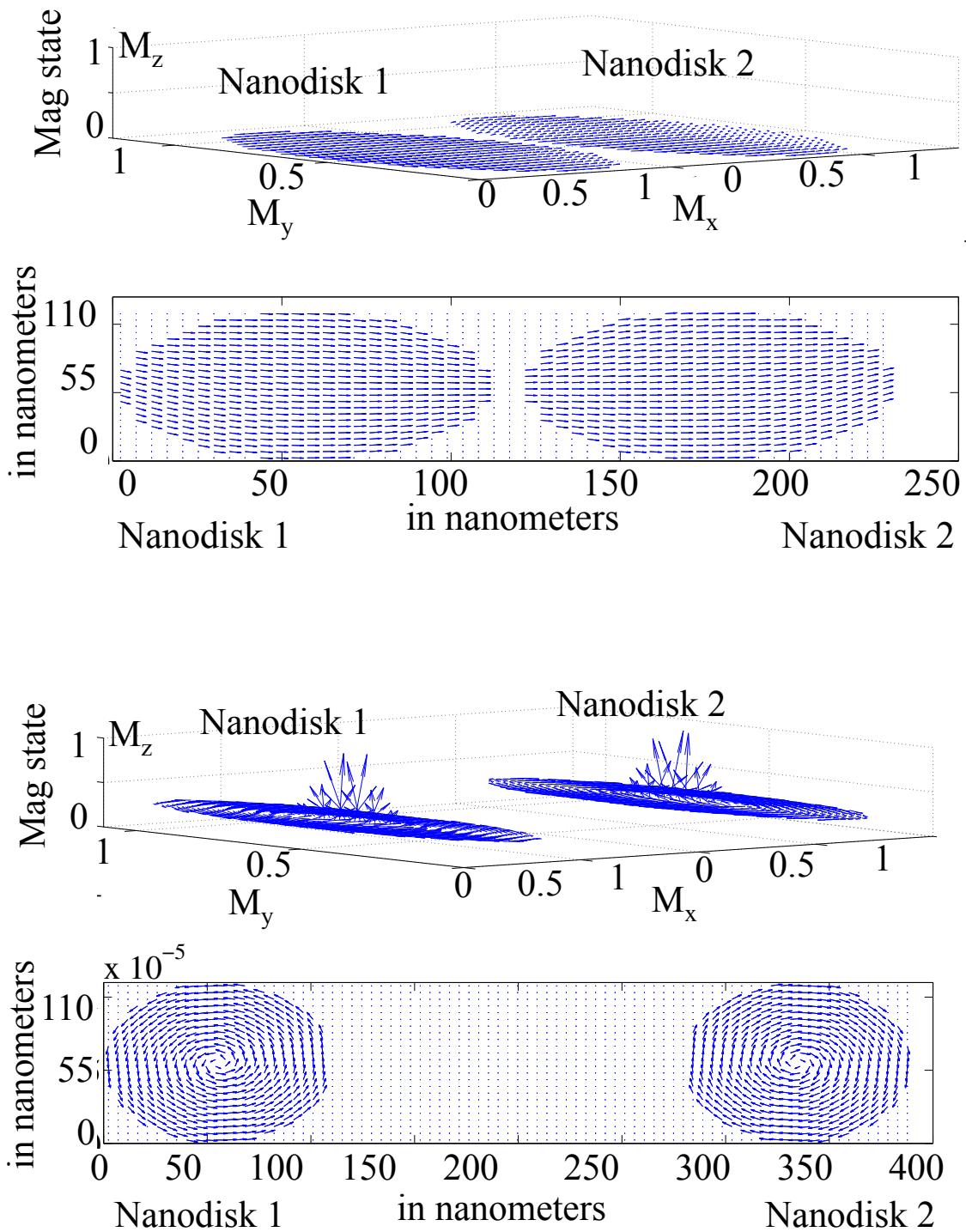


Figure 5.8. The vector representation of a single domain state and vortex state. (Top) and vortex state (Bottom) nano-disk of diameter $D = 110$ nm and thickness $T = 10$ nm from LLG simulation


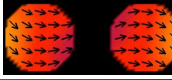








Spacing \ Thickness	(i) Thickness = 10 nm	(ii) Thickness = 15 nm
(a) Spacing = 50 nm		
(b) Spacing = 150 nm		
(c) Spacing = 200 nm		
(d) Spacing = 250 nm		
(e) Spacing = 300 nm		

Figure 5.9. Magnetization direction of nano-magnetic disks superimposed on underlying domains. For 100 nm diameter and thickness (i) 10 nm, (ii) 15 nm with different edge-to-edge spacing marked by open circles, (a) $S = 50$ nm, (b) $S = 150$ nm, (c) $S = 200$ nm, (d) $S = 250$ nm, (e) $S = 300$ nm. Each pair of nano-magnetic disks is the snapshots at t_{final} ground states (energy minimum states).

for all our simulations. For exciting the system, we used an initial time dependent field B_z of 300 *Gauss* in +x direction.

In order to study the dipolar neighbor interaction on magnetization states of nano-magnetic disks with similar dimension, we have placed two such disks A and B adjacent to each other as shown in Fig. 5.7. The disks are composed of Py material, where Py corresponds to Permalloy $Ni_{80}Fe_{20}$. The edge-to-edge spacing between the disks is one of the varying parameters of investigation along with variation in diameter and thickness of the disks. For each pair of nano-magnetic disks the edge-to-edge spacing between the disks was varied from 0 nm to 300 nm for fixed diameter and thickness and observations of the magnetization states. We calculated the interaction energy, which is the neighboring dipolar coupling energy, by subtracting the magnetic energies of the individual disks from the total magnetic energy of the system.

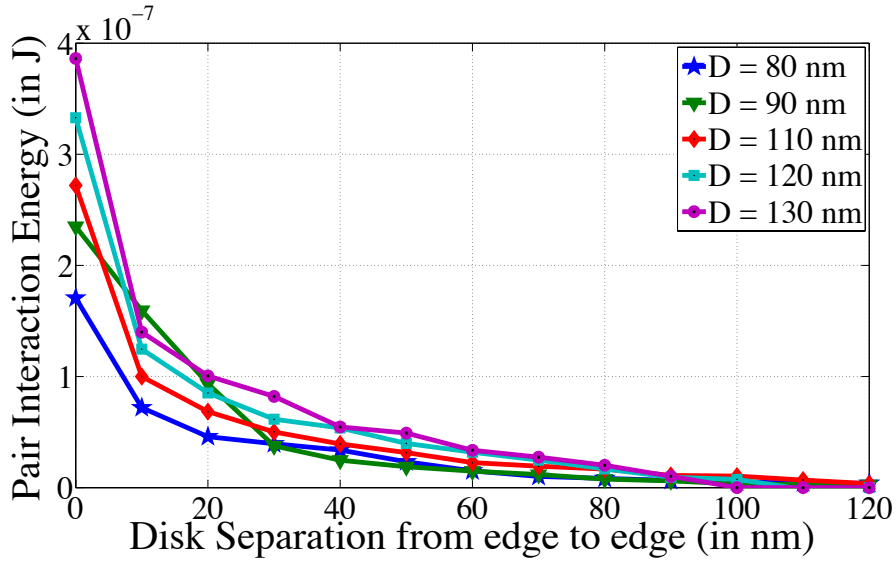


Figure 5.10. Pair interaction energy versus the spacing between nano-magnetic disks with thickness

5.4 Simulation Results and Discussion

To observe the effect of diameter and thickness on the dipolar coupling between the neighboring nano-magnetic devices, similar experimental set up and procedure was followed as mentioned in Sec. 5.3.

5.4.1 Effect of Diameter Variation on Interaction

To illustrate the effect of disk diameter on the final magnetization ground state of coupled nanodisks, we examined two single domain nanodisks with respect to change in edge-to-edge spacing. In this study, the thickness of the disk was kept constant. As the diameter of the nano disk was increased, the probability of the vortex state increased and thereby the magnets prefer to settle in the vortex state much faster for large diameters. The graph in Fig. 5.10 shows the variation of interaction energy with edge-to-edge spacing for different disk diameters. It is evident from the graph the interaction energies are high when the

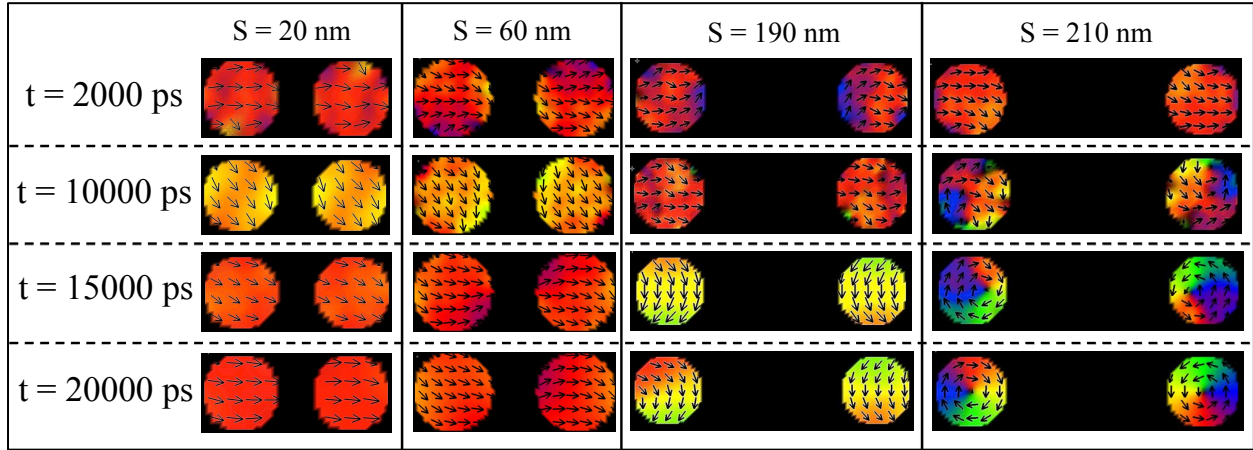


Figure 5.11. The time evolution of magnetization state of a nanomagnetic disk with respect to different spacing

nano-magnets were in the single domain state and almost zero when settled in the vortex state as the interaction energy decreases, when the edge-to-edge spacing is increased.

5.4.2 Effect of Thickness Variation on Interaction

To illustrate the effect of disk thickness for a coupled nano-magnetic system the diameter of the disks were kept constant. Fig. 5.9 shows the variation of the magnetization state, when the thickness was increased with respect to change in edge-to-edge spacing. As one can see, when the thickness was increased, the vortex state transition occurs for a larger edge-to-edge spacing. The graph in Fig. 5.12 shows the variation of interaction energy with edge-to-edge spacing for different disk thicknesses. It is evident from the graph that the interaction energies are high when the nano-magnets were in the single domain state and almost zero in the vortex state.

Based on the simulated results, nano-magnetic disks with thicknesses of less than 8 nm had a fixed magnetization of the single domain state and for the nanodisks with thicknesses more than 20 nm had a fixed magnetization of the vortex state regardless of any variation in the edge-to-edge spacing. The nano-magnetic disks with thickness between 8 nm to 20 nm

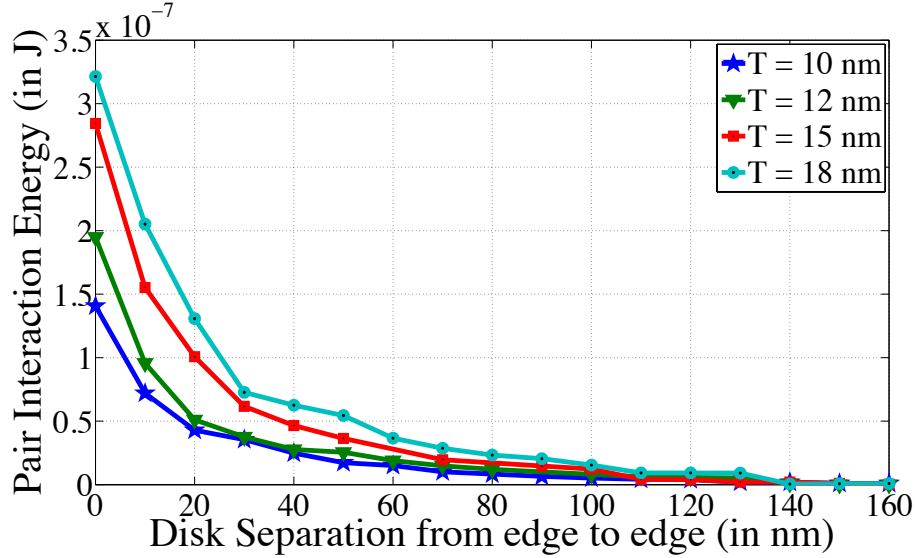


Figure 5.12. Pair interaction energy versus spacing between the disks with disk diameter $D = 100$ nm. The thickness T varying from 10 nm to 18 nm.

and diameters between 80 nm to 140 nm, with the change in edge-to-edge spacing, similar nano-magnetic disk existed either in the SDS or VS. We also observed that magnetic coupling energies drops continuously with the factor of $\frac{1}{s^3}$, where s is the edge-to-edge spacing.

5.5 Fabrication

To validate the simulation results, *D K Karunaratne, USF* helped us in fabricating pairs of nanomagnets disks that had an average diameter of 110 nm and an average thickness of 10 nm with the edge-to-edge spacing varying from 20 nm to 260 nm. Each pair of nano-magnetic disks with different edge-to-edge spacing was placed far apart to minimize magnetic interaction. The samples were fabricated on a Silicon wafer using e-beam lithography, e-beam evaporation, and a lift-off process. As for the magnetic material, Permalloy ($Ni_{80}Fe_{20}$) was chosen for its high magnetic permeability and its low coercivity. The samples were characterized with a scanning electron microscope to identify pairs of defect-free nano-magnetic disks. Next, an external magnetic field in the form of a pulse was applied to

the samples along the in-plane direction for stimulus. Finally, the nano-magnetic disks were allowed to settle to an energy minimum and the defect free magnetic systems were characterized with a magnetic force microscope. Fig. 5.6 is the MFM micrograph images that are correlated with the numerical simulation results. Table. 5.1 shows the number of SDS and VS observed in both the disks for different edge-to-edge spacing for average diameter $D = 110$ nm and average thickness = 10 nm. When the spacing $S \geq 180$ nm, we observed only vortex states. For spacing $S \leq 60$ nm, we observed only single domain states.

5.6 Conclusion

We have observed and verified that a nano-magnetic disk, with certain dimension, can exist either in the SDS or VS depending on the edge-to-edge spacing between the nano-magnetic disks. We have also investigated the effect of interaction energy on nano-magnetic disks for different diameters and thicknesses by varying the edge-to-edge spacing between the nano-magnetic disks. Finally, we fabricated pairs of nano-magnetic disks (diameter of 110 nm and thickness of 10 nm) with varying edge-to-edge spacing and observed their final magnetization state. Repeated experiments of the fabricated results concluded that the pairs of nano-magnetic disks with an edge-to-edge spacing from 20 nm to 100 nm always settled to single domain state whereas when the edge-to-edge spacing was from 120 nm to 260 they always settled to vortex state. This work was published in *IEEE Transactions on Magnetics*.

Table 5.1. Number of SDS and VS compared with the fabricated pairs of nano-magnetic disks. The disks have diameter $D = 110$ nm and Thickness $T = 10$ nm with different edge-to-edge spacing by *D K Karunaratne, USF*.

Edge-To-Edge Spacing	Single Domain States Observed (Disk Pair %)	Vortex States Observed (Disk Pair %)
20 nm	100 %	0 %
60 nm	100 %	0 %
100 nm	100 %	0 %
120 nm	40 %	60 %
180 nm	0 %	100 %
220 nm	0 %	100 %
260 nm	0 %	100 %

CHAPTER 6

PROGRAMMABLE NANOMAGNETIC GRIDS FOR NON-BOOLEAN COMPUTATION

Recently, several design techniques have been proposed for using a collection of nano-magnets for Boolean and Non-Boolean computation. However, in most of the design, each nano-magnet is spatially arranged in a location that matches a particular problem. In this work, we describe a compact design and implementation of reconfigurable array of nanomagnets using spin-transfer torque based on Magnetic RAM array architecture that could perform non-Boolean computation. We have placed these nanomagnets in such a way that the ferromagnetic free layers couple with neighbors. The programming currents are studied with respect to diameter and damping constant of the Magnetic RAM cells. The cells that needs to be “deselected” from the array is taken to a non-computing oscillating state. In this work, we have shown: A non-Boolean framework effective to solve several instances of quadratic optimization problems, such as those arising in computer vision applications. The STT strengths, which have the ability to induce oscillations for deselection of the cells, have been predicted through LLG simulations. The reconfigurable array design consists of an in-plane (IP) NiFe free layer and a fixed polarizer [magnetized out-of-plane (OP) Co/Pd] multilayer.

6.1 Contribution

The unique contribution from this work are as follows.

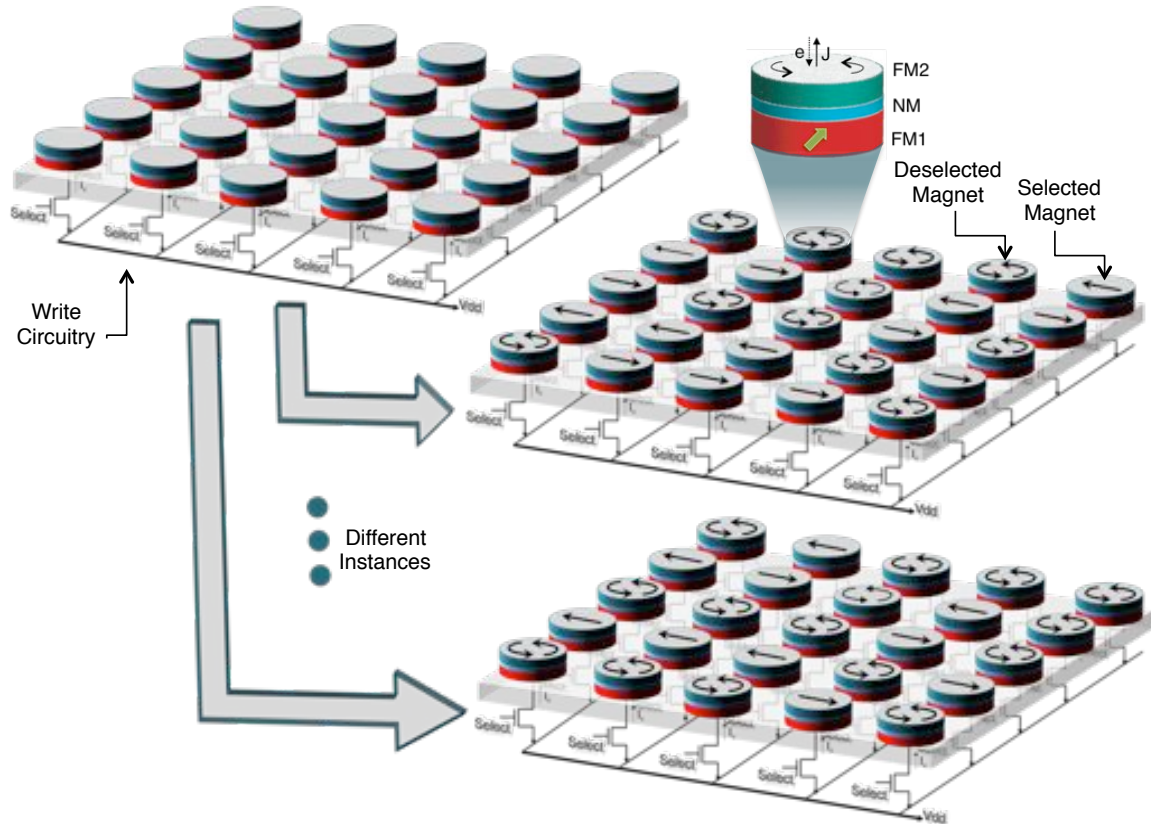


Figure 6.1. Schematic of the programmable logic computation hardware. A array of spin-transfer torque based MRAM reconfigurable array (STRAN) with underlying CMOS devices to read/write the magnetization of each cell. Only the “selected” magnets (magnets in single domain state) participate in the computation.

- we exploit spin-transfer nano-oscillator (STO) to deselect the nanomagnets from the array to a non-computing state using the torque generated from the OP polarizer.
- we have used STRAN for non-Boolean framework, where the cells are circular that exhibits multiple magnetization states.
- we have shown the programming current dependence on the dimensions of the MTJ cells where the I_P decreases with the decrease in dimensions of MTJ. This means that the STRAN is highly scalable.

6.2 Introduction

Single-domain nanomagnets is well known as computing and as data storage elements[128, 129, 130]. So far, there has been several ideas to implement Boolean computation using magnetic tunnel junctions MTJs and domain wall magnets [131, 132, 133, 134]. In these systems, the shape anisotropy provides two stable magnetization directions encoded with classical binary bits “0” and “1”. With the development of many interesting experiments on lateral spin valves, domain wall magnets and spin hall effect, have opened new avenues in non-Boolean computation[135, 136]. Recently, Sarkar *et al.*, DrSouza *et al.* and Zhang *et al.* have proposed various algorithms for computer vision applications using nanomagnets which performs non-Boolean computation[137, 138, 139, 140].

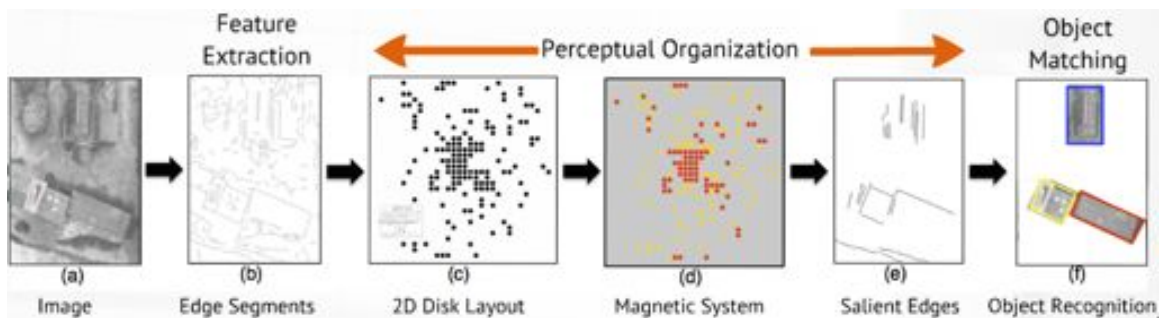


Figure 6.2. Object recognition using magnetic field-based computing proposed by Sarkar *et al.* in [4]

In which, Sarkar *et al.* have proposed an algorithm that harness energy minimization aspects of nanomagnets to solve quadratic optimization problems that often arises in computer vision applications as shown in Fig. 6.2. Among those non-Boolean algorithms, the approach already proposed by Sarkar *et al.* using circular nanomagnets showed feasible performance for practical applications[137, 141]. However, fabricating different magnetic layouts to solve every instance of a quadratic optimization problem remains an issue and highly expensive which still restricts current state-of-art application. Spin-Transfer Torque induced Magnetoresistive random-access memories (STT-MRAM) promise great interest to

be integrated in reconfigurable logic circuits. However, it has been potentially used only as memory configuration in FPGA's to replace the flash and SRAM[142, 143, 144, 145], which offers non-volatility to FPGA circuits. In this work, we present a simple reconfigurable array (from now referred as STRAN - Spin-Torque driven Reconfigurable Array of Nanomagnets) of $n \times n$ magnetic elements using spin-torque nano-oscillator technique for deselecting any magnet from computation shown in Fig. 6.1 and can emulate 2^{n^2} different magnetic layouts. Each magnetic cell is a magnetic multilayer of Co/Pd/MgO/NiFe. This type of problem solving can tremendously benefit from STT-MRAM technology due to its density and compatibility with CMOS.

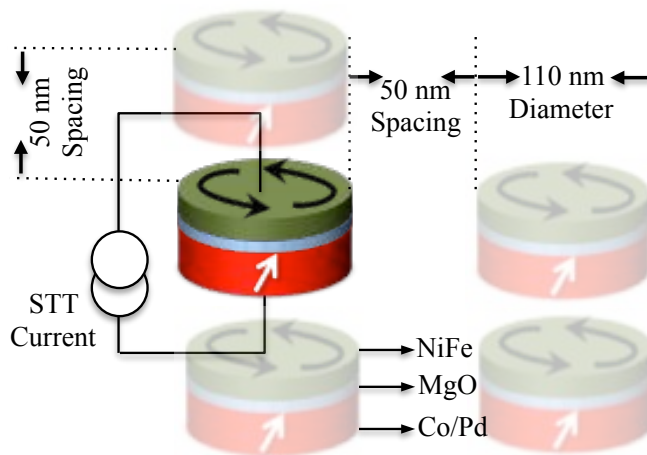


Figure 6.3. Schematic of STRAN cell dimension, material and spacing parameters.

In order to perform non-Boolean computation, we have shown an example of a solution to quadratic optimization problem that accomplishes identifying salient edge segments from an image as shown in Fig. 6.4(a-d) using our reconfigurable array. The results were verified with fabricated layouts of nanomagnetic disks.

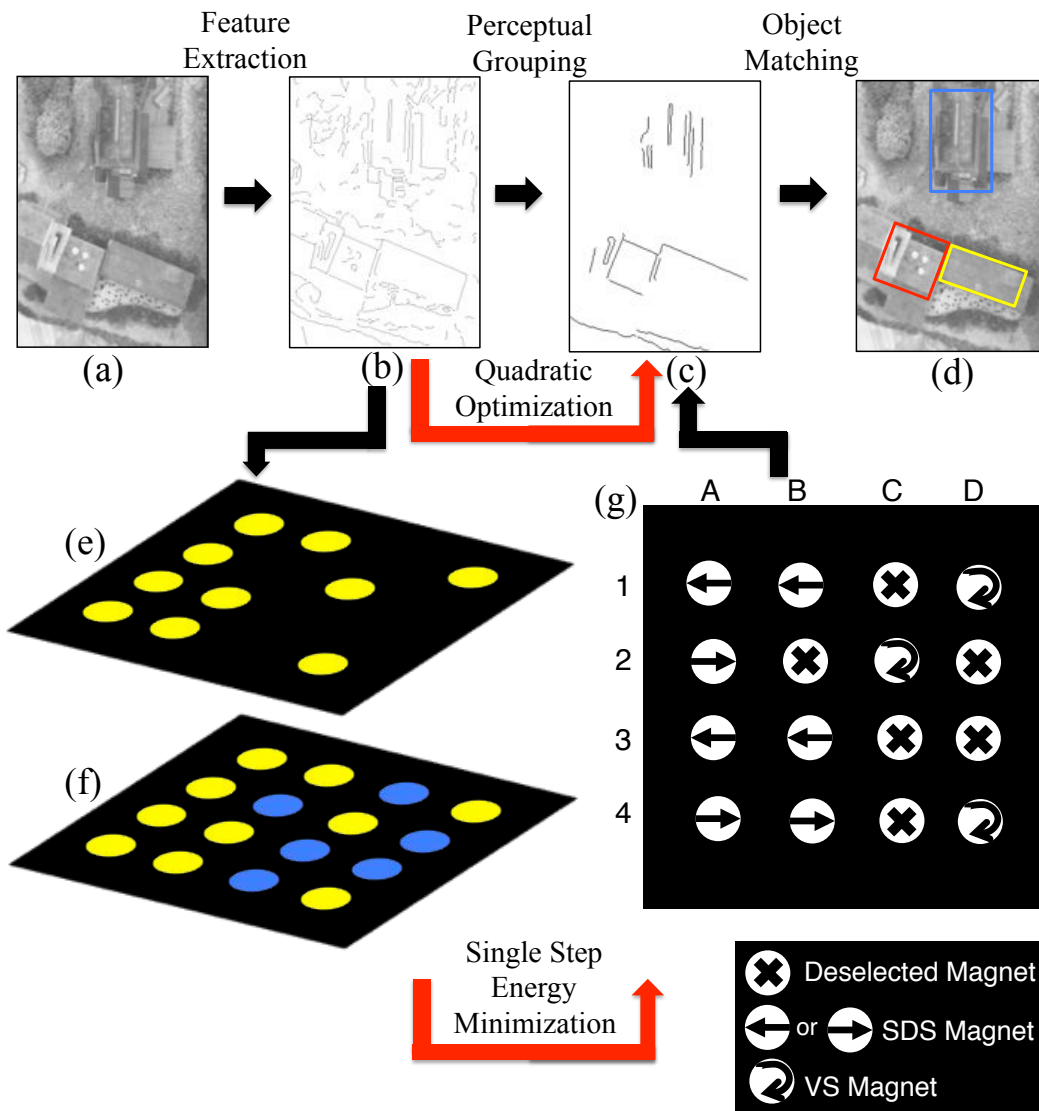


Figure 6.4. Object recognition using magnetic field-based computing. (a) Gray scale image. (b) Edge image of (a). (c) Distance map of the edge image in (b). (d) Object mapping of salient features in image (a). (e) 2D layout of nano-disks generated from MDS layout. (f) Nano-disks mapped to STRAN. “yellow” disks are selected magnets and “blue” disks are magnets to be deselected. (g) Magnets settle in SDS or VS depending on the coupling energy and applied to salient edge segments.

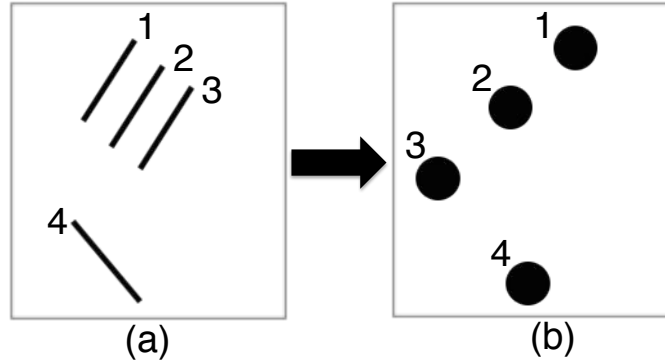


Figure 6.5. Magnetic layout corresponding to the edge segments. (a) Line segments (b) Corresponding 2D MDS layout

6.3 Nanomagnets for Vision Computation - a Non-Boolean Framework

In vision computing, the object recognition involves three main steps: feature extraction, perceptual grouping and object matching (see Fig. 6.4(a-d)). The first step involves feature extraction, which is extraction of local features say edges, points and regions. The second step is perceptual organization, which is the act of recognizing important features from an object and not from the background. The final step is object matching, which is used to match the salient edges from the object database. While there are many hardware solutions to speed up the process in the first process, the perceptual organization step are still solved in conventional software computation where the number of iterations increases with the problem size and is computationally expensive. The grouping of important edge segments can be accomplished by quadratic optimization process as shown in Fig. 6.4(b) & (c). In [137, 141], Sarkar *et al.* have already demonstrated an unconventional way of non-Boolean computation, to solve several quadratic optimization problems.

In which, each of the line segments shown in Fig. 6.4(b) would be assigned with a “0” or “1” corresponding to unimportant edge and important edge respectively. So, every pair of edge segments would carry an important measure called the affinity value capturing its saliency (importance). There are numerous ways to measure this saliency. For example in

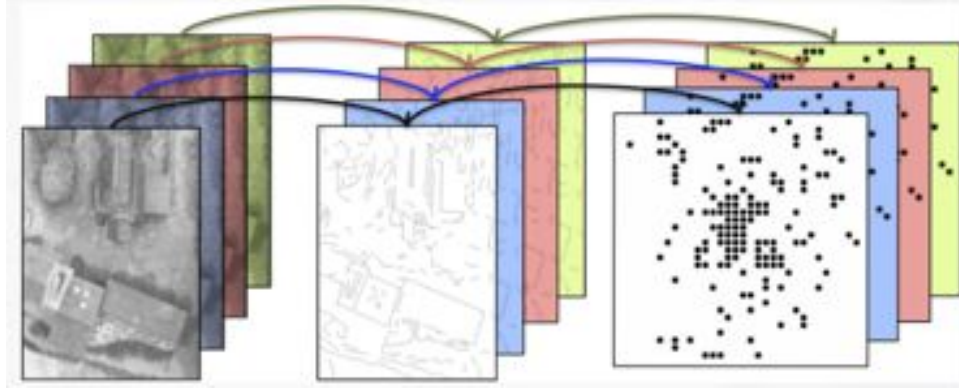


Figure 6.6. Magnetic layouts for multiple images. The MFC needs multiple instances of magnetic layouts for every image.

Fig. 6.5(a), if there are three straight lines that are parallel 1,2 & 3, their affinity value will be very high than other random line segment 4. Also, in Fig. 6.5(b), notice that each line segments corresponds to a magnet. The purpose of placing those magnets in certain coordinates represents the features similar to Fig. 6.4(b), such that the distance between the magnets is directly proportional to the affinity between the corresponding line segments. Accordingly, their pairwise interaction will also be proportional to their coupling energies is given by [137]. By using this design developed, it will be difficult for us to fabricate specific individual layouts for each and every instance as shown in Fig. 6.6.

Therefore, we would not be able to completely leverage the advantage of this methodology. In this work, we present a simple reconfigurable array using the STT-MRAM in Fig. 6.4. Basically, the way of solving an quadratic optimization problem using nanomagnets proposed here is almost same as the one presented by Sarkar *et al.* in [137, 141]. Different from the method of [137], which uses magnetic field driven monolayer single domain nanomagnets, our proposed reconfigurable array are STT-MRAMs, which can be easily programmable using STT currents. Moreover compared to the number of layouts that it can solve in [137], our hardware will be able to solve 2^{n^2} different arrangements of layouts for any such non-Boolean quadratic optimization problems.

6.4 Design of Reconfigurable Array (STRAN) using LLG Simulation

We carried out a micromagnetic simulation based on Landau-Lifshitz-Gilbert (LLG) equation including STT. The STRAN consists of circular MTJ cells with the diameter of 110 nm, spaced 50 nm with out-of-plane polarizer as its reference layer (pinned layer) and a free layer (FM1) magnetized in-plane with structure (Co/Pd 40 Å /MgO 35 Å /NiFe 100 Å) as shown in Fig. 6.3. The circular disk shape magnet has two stable magnetization states (Single domain state- SDS and Vortex state- VS). We have investigated the effect of magnetic neighbor interaction on the magnetization state behavior for computation. We have observed that a nano-magnetic disk, with certain dimension selected near the phase boundary between the SDS and VS region, can have two possible ground states (SDS & VS) depending on the edge-to-edge spacing between the nano-magnetic disks. We have observed nano-magnetic disks spaced far apart from its neighbor, settled in the vortex state and coupled nano-magnetic disks with less spacing settled in the single domain state. We have used an array of such nanomagnets to solve optimization problems.

The magnetization dynamics of the FM1 and FM2 layers can be described by Landau-Lifshitz-Gilbert-Slonczewski (LLGS) equation Eq.6.1 including the spin-torque term. We have used a 3D-compatible correction method for micromagnetics of curved geometries discretization as shown in [127]. The unit element size is 4.68 nm x 4.68 nm x 4.68 nm. We have used time based relaxation method, which is rotating the magnetization with respect to the effective field vector. The simulations incorporated predictor corrector integrator that yields most accurate results with damping factor $\alpha \sim 0.015$ and a convergence value of 1×10^{-4} for exiting the calculation. We used a free electron gyromagnetic frequency γ to be 17.6 Mhz for all our simulations.

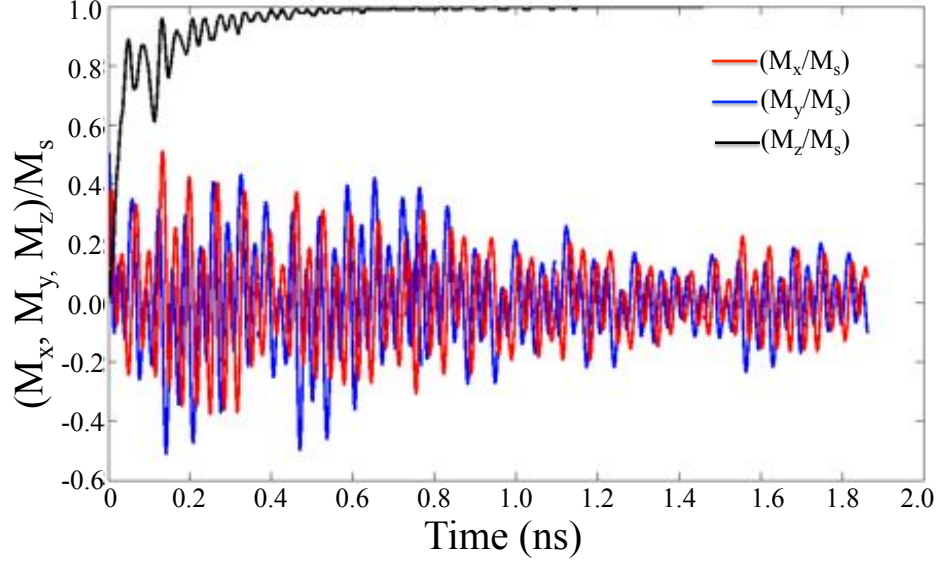


Figure 6.7. The temporal evolution of the magnetization components under oscillation

$$\begin{aligned}
\frac{d\mathbf{M}}{dt} = & -\gamma \mathbf{M} \times H_{eff} - \frac{\alpha\gamma}{M_s} \mathbf{M} \times (\mathbf{M} \times H_{eff}) \\
& - \frac{2\mu_B J}{(1 + \alpha^2)edM_s^3} (\mathbf{M}, P) \mathbf{M} \times (\mathbf{M}, P) \\
& + \frac{2\mu_B \alpha J}{(1 + \alpha^2)edM_s^2} (\mathbf{M}, P) (\mathbf{M}, P)
\end{aligned} \tag{6.1}$$

The first term on the right side of Eq. 6.1 is the conventional magnetic torque with the gyrometric ratio γ . This torque is driven by the effective field as shown below,

$$H_{eff} = \frac{1}{\mu_0} \frac{\delta E}{\delta \mathbf{M}} \tag{6.2}$$

where the effective field of the LLGS equation includes the anisotropy, demag, zeeman and coupling fields, namely, $H_{eff} = H_{exch} + H_{anis} + H_{coupling}$. The last two terms in Eq. 6.1 described in the LLGS equation that drags the magnetization away from the initial in-plane state and drives the magnetization to precession around the effective field. The scalar function is given by [146]

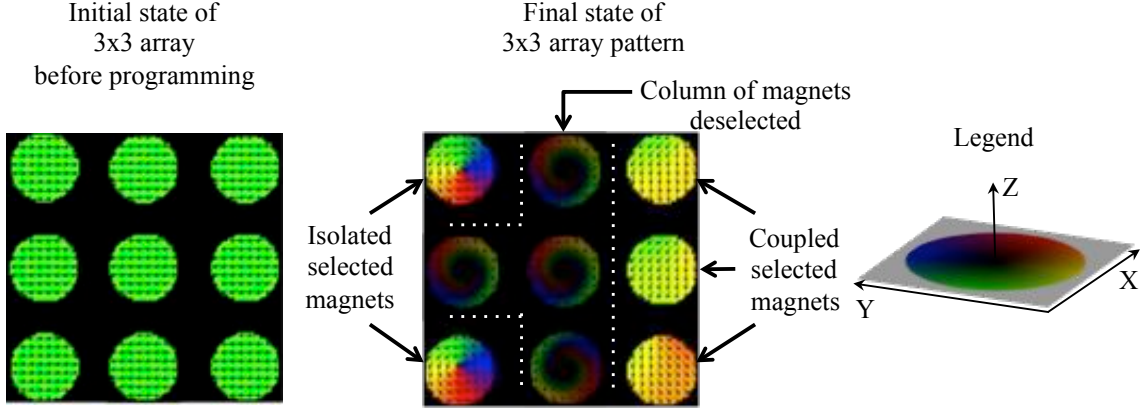


Figure 6.8. Programming a pattern to a 3by3 STRAN. The FL2 dimensions are 100 nm diameter, 8 nm thickness. The final magnetization states of nanomagnets in column(2) have deselected magnets and the selected magnets settle in their energy minimum states depending on its neighbor interaction.

$$g(M, P) = \left[-4 + \frac{(1 + \eta^2)(3 + M.P/M_s^2)}{4\eta(3/2)} \right] \quad (6.3)$$

and the corresponding effective field is given by,

$$H_{eff-STT} = \frac{2\mu_B J g(M, P) M \times P}{(\gamma e d M_s^3)} \quad (6.4)$$

where μ_B , J , d , e and M_s , are the Bhor magnetron, current density, thickness of the free layer, electron charge and saturation magnetization, respectively.

When the spin-torque current (hereafter referred to as ST current), when passed along a special direction through a magnet can lead to some interesting magnetization behaviors. Among the special behavior, the temporal evolution of magnetization components for a continuous ST current, the magnetization dynamics lies in the multi-domain state. Concerning the same kind of devices, experimentally published by Bertotti *et al.*, Huang *et al.* and Klselev *et al.* thoroughly analyzed each precessional state corresponding to different ST currents. They have also predicted similar existence of multidomain state (MS) in some regions of the state space [147, 148, 149, 150]. The mechanism is similar to precession states, except that

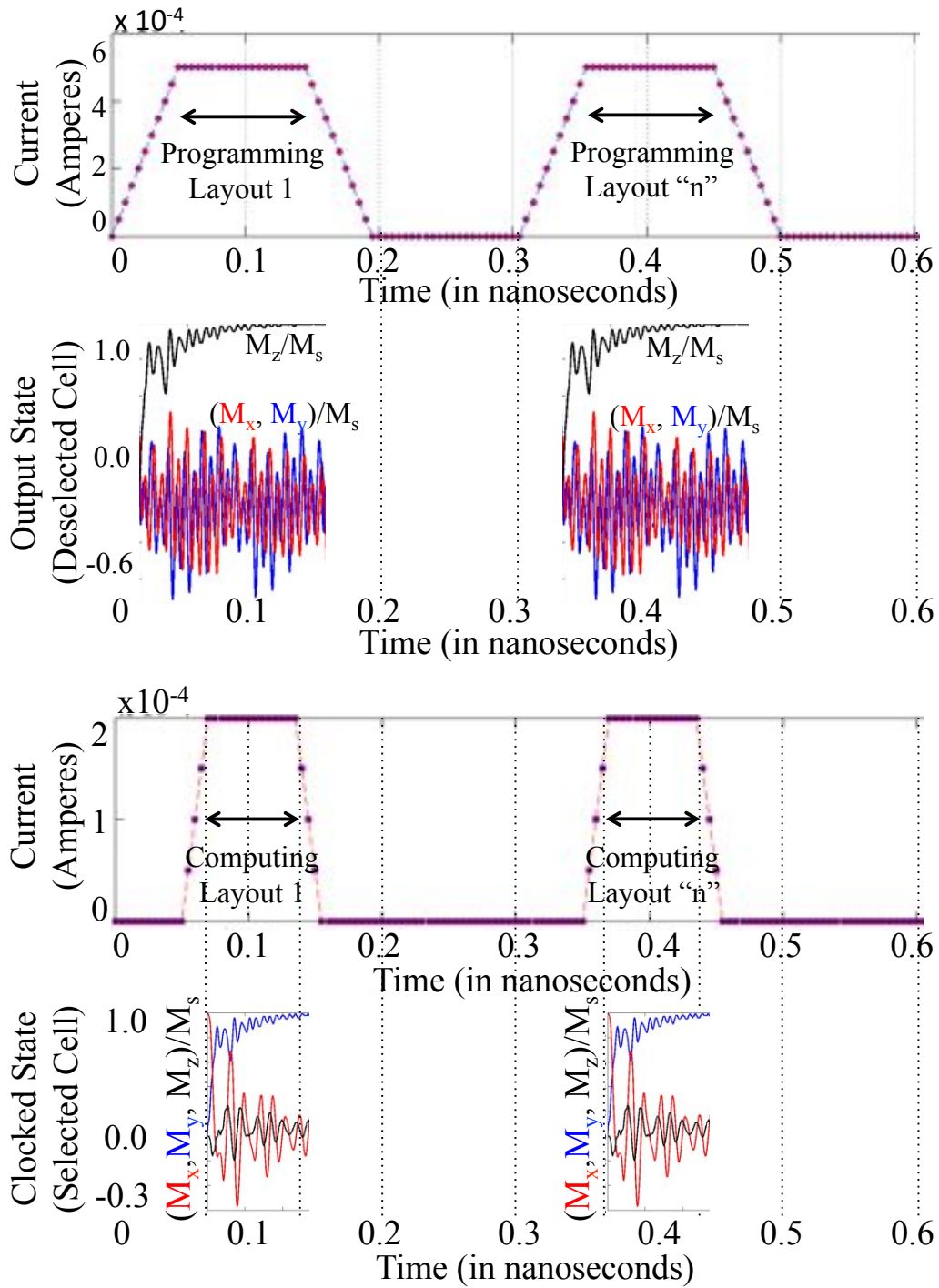


Figure 6.9. STT current induced deselection of the cell. The cell diameter is 110 nm and thickness 5 nm with 50 nm spacing between the cells. The current profile is shown for deselection and clocking of the selected cells.

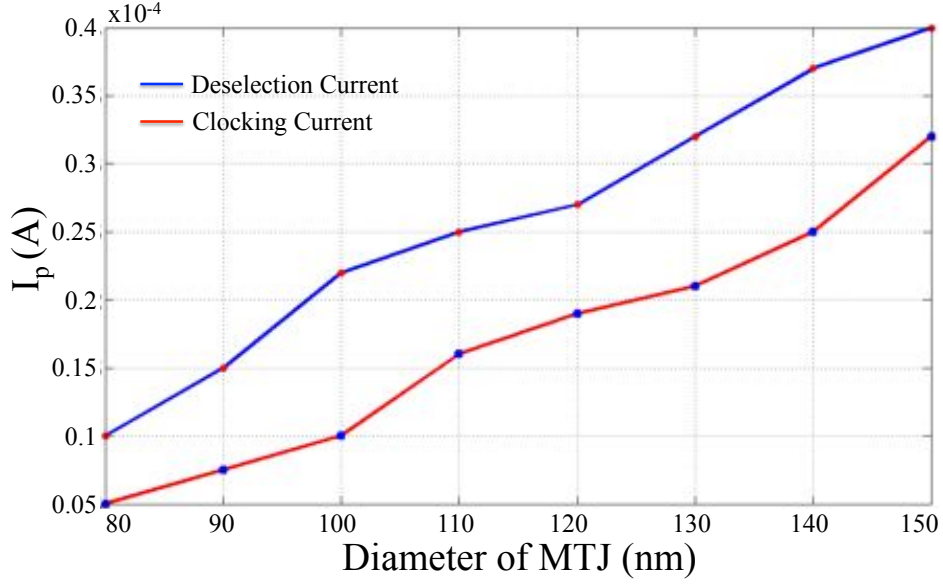


Figure 6.10. Programming currents dependence on diameter of MTJ cell. The programming current reduces as the diameter reduces. This means that the STRAN is highly scalable.

the free layer is not a monodomain and the amplitudes of magnetization oscillation are not constant as shown in Fig. 6.7. This kind of multidomain could be explained by the large ST current input energy. The ST current energy per unit time driving into the nanomagnet is so large that the formation of magnetic excitations is much shorter than the element size becomes possible, leading to the formation of multidomains. We have implemented these ideas using the LLG micromagnetic solver [92]. Fig. 6.10 shows the size dependence of the programming current. The current profile for our STRAN is shown in Fig. 6.9.

Considering a neighboring magnet spaced 50 nm apart, the dipole-dipole coupling interaction between the i^{th} and the j^{th} magnet is expressed as

$$H_{dipole}^{ij} = \sum_i^N \sum_j^N \frac{1}{r_{ij}^3} (m_i \cdot m_j) - 3(m_i \cdot \vec{e}_{ij})(m_j \cdot \vec{e}_{ij}) \quad (6.5)$$

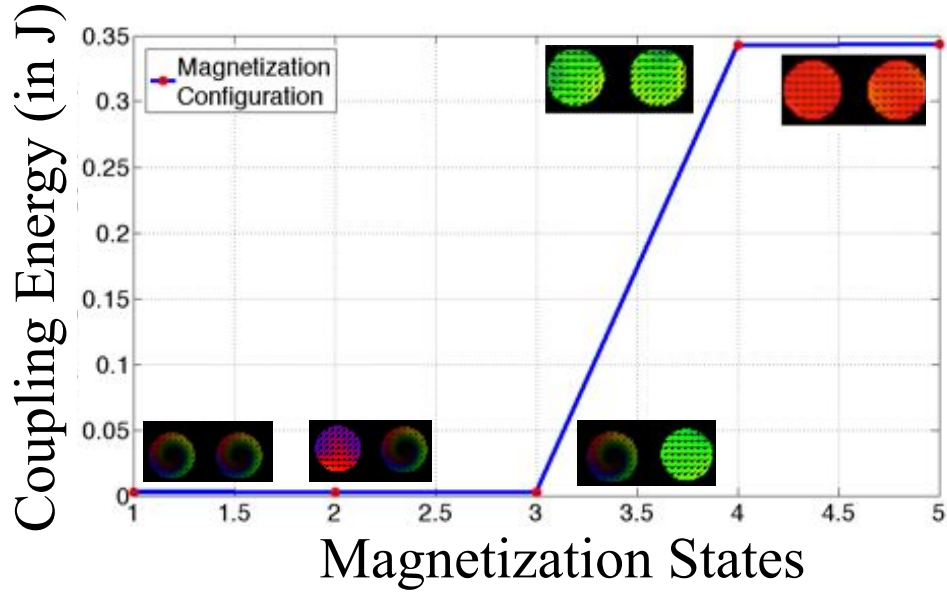


Figure 6.11. Coupling energy graph between deselected (oscillating) magnet with its neighbors obtained using LLG simulation from the array. The coupling energy between a deselected magnet (DS) with any of its immediate neighbors is zero, whereas the selected magnets in single domain state with its neighbors has higher coupling energy.

where m_i is one magnet and m_j is other magnet and H_{dipole}^{ij} is the dipole coupling energy between m_i and m_j magnets, e_{ij} is the unit vector along the direction that connects the two magnetic moments. r_{ij} is the center to center distance between m_i and m_j .

By considering the two magnetic moments from the deselected magnet and any neighboring magnet, each of μ_B , one can approximate the magnitude of dipole-dipole interaction to be ~ 0.00263 , which approaches to zero. Our results shown in Fig. 6.11 suggest the coupling might be considered as weak and non-interacting with its neighboring magnet precising, which favors as our method to “deselect” the cell from computing. Once the magnets are deselected, the array would then be clocked and allow the energy minimization nature of the “selected” magnets in the grid to perform the computing. The final states would be read off as the solution to the problem mapped to the grid.

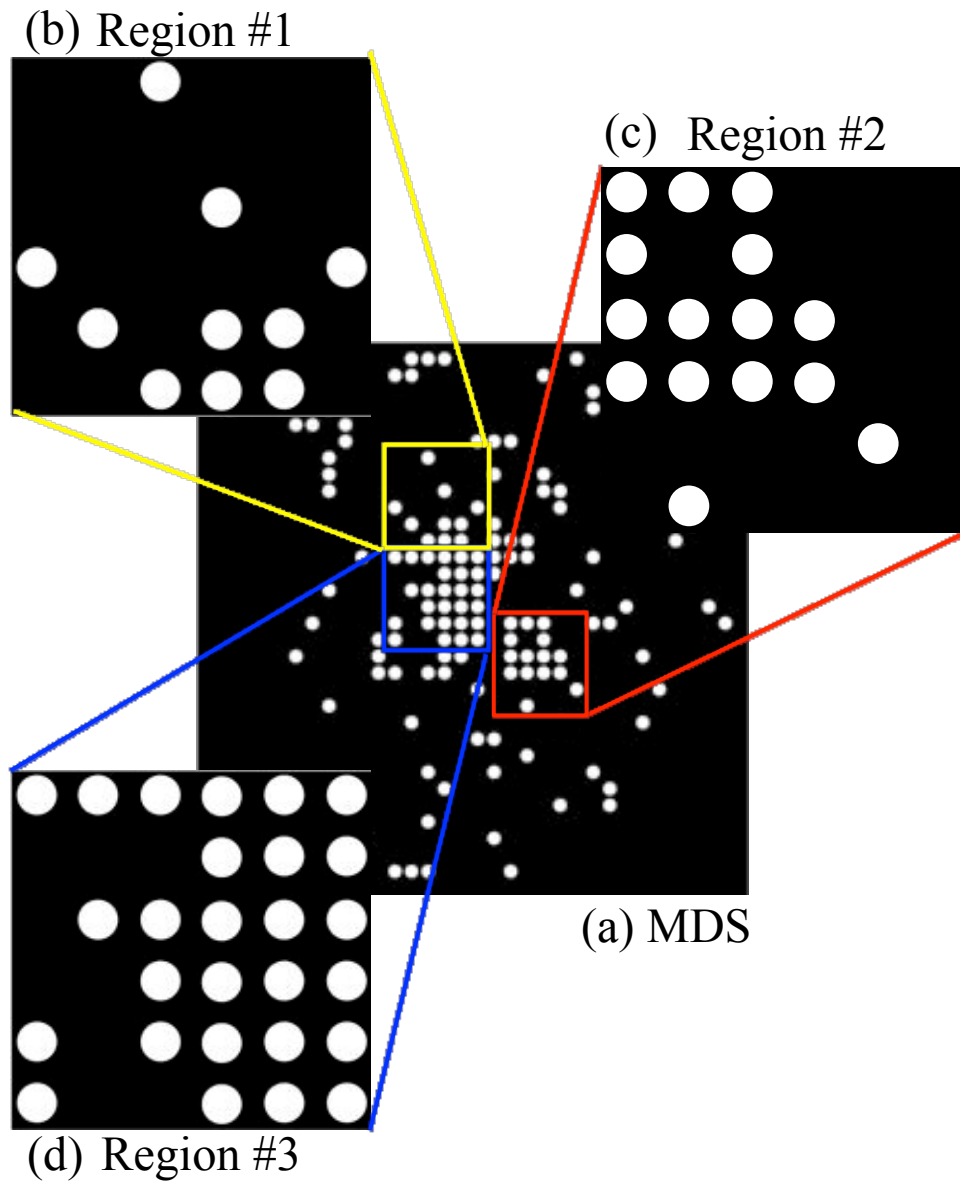


Figure 6.12. Selection of cells using spin-transfer current, simulated using LLGS Micromagnetic simulator.

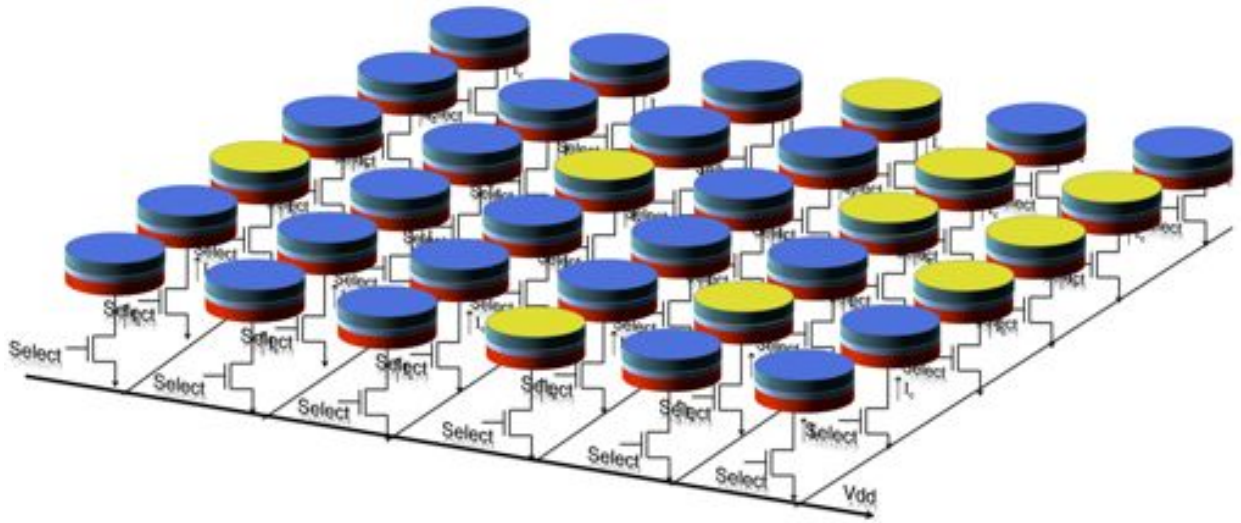


Figure 6.13. Schematic of region 1 in programmed STRAN hardware

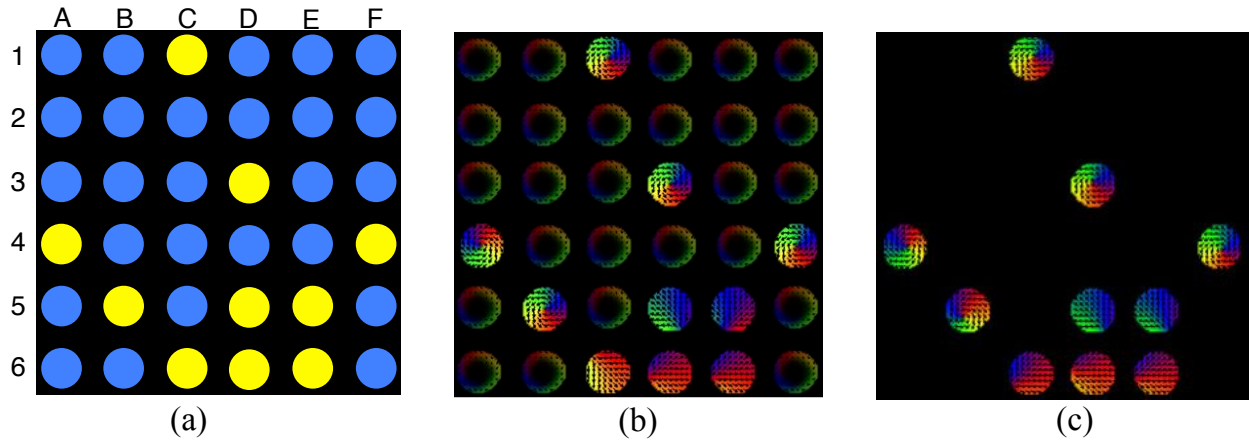


Figure 6.14. STRAN output for region 1 layout

Table 6.1. STRAN cell critical deselection current. The current pulse duration and clocking current for cell dimensions 110 nm Diameter and 50 nm spacing between cells.

Thickness of free layer	Critical Deselection Current in μA	Critical Clocking Current in μA
5	150	50
8	200	100
11	260	160

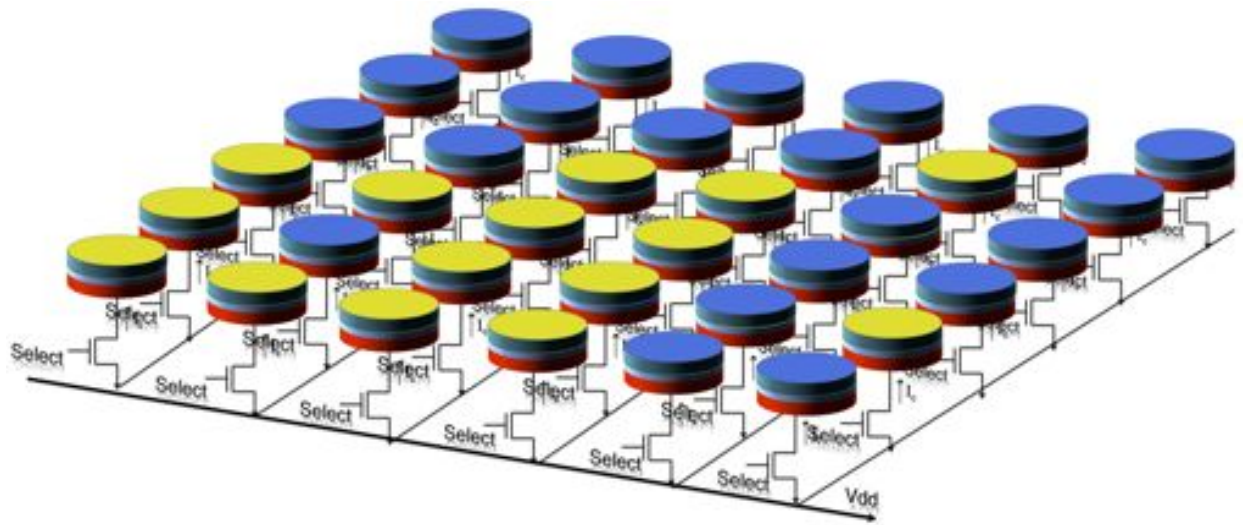


Figure 6.15. Schematic of region 2 in programmed STRAN hardware

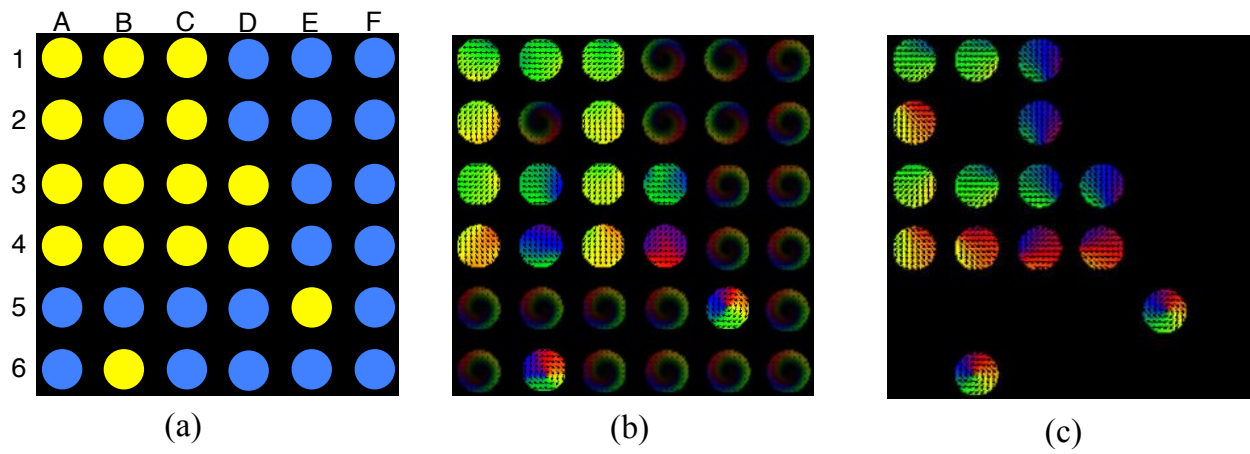


Figure 6.16. STRAN output for region 2 layout

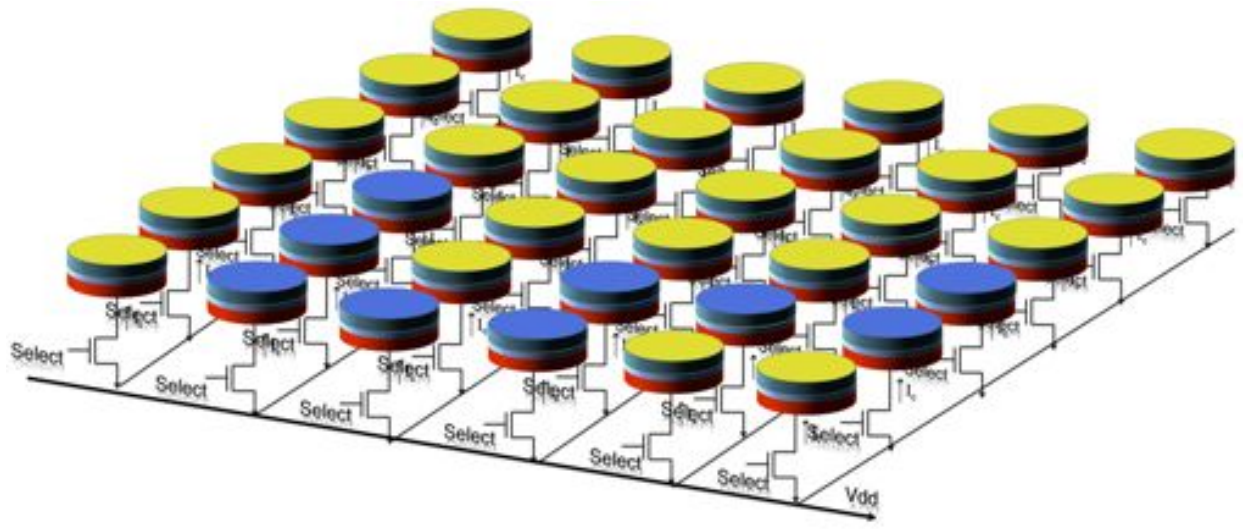


Figure 6.17. Schematic of region 3 in programmed STRAN hardware

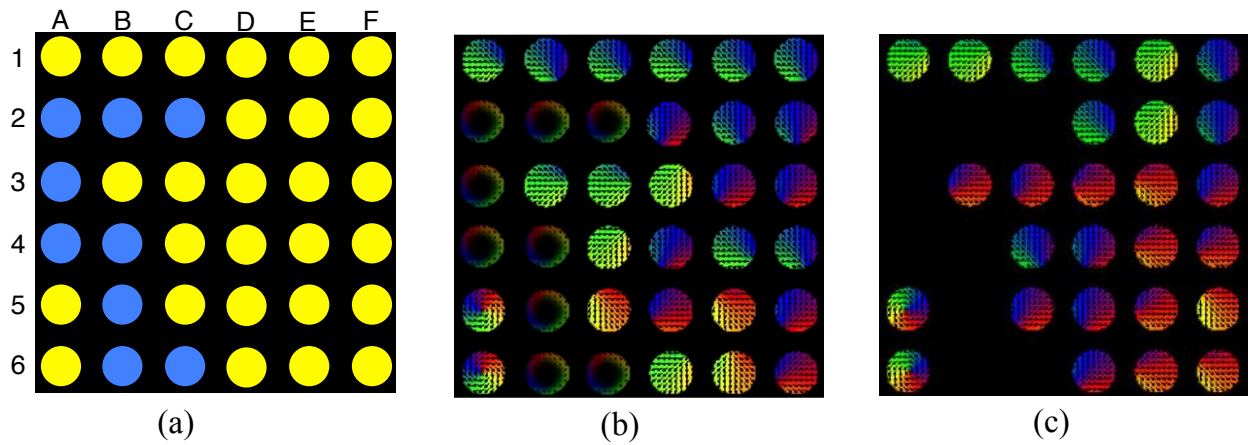


Figure 6.18. STRAN output for region 3 layout

6.5 Non-Boolean Computation using STRAN

The spatial arrangement of nano-disks layout from MDS that matches a particular image was obtained from our previous experiments [137] as shown in Fig. 6.12(a). We have divided the layout into three different regions that could be represented in a 6 by 6 grid of nanomagnets as shown in Fig. 6.12(a),(b)&(c). We have shown our STRAN output with respect to all the regions in Fig.6.13 & Fig. 6.14, Fig.6.13 & Fig. 6.16 and Fig.6.13 & Fig. 6.18. The second column shows STRAN layout mapping with respect to regions. The selected magnets are represented with “yellow” dots and “blue” dots represents the magnets that needs to be deselected. The deselected magnets will be driven to a non-computing oscillating state and the current profile is shown in Fig. 6.9. As one can see from the STRAN output in column 3, for Region 1 the deselected magnets for example A1 to A3, A5, A6 and so on. The selected cells will be clocked using ST current and released to settle in its energy minimum state. The ST clocking current profile is shown in Fig. 6.9. We have already shown that the oscillating magnet does not interfere in the computation. To verify this with our STRAN output, we performed LLG simulation of only the selected cells and one can see the magnetization states matches well with the STRAN output.

As shown in Fig.6.14 for region 1 and column 3, one can see that the isolated magnets C3, A4, B5, D3 and F4 settle in the vortex state and the remaining selected magnets settle in the single domain state. These results well matched with the fabricated free layer with critical dimensions and we used an image processing application MSE [151] to estimate the final magnetization states of all the selected magnets. From the MSE output, the “yellow” color represents vortex states and “red” color represents single domain states. As one can see, the magnetization states well matched with our STRAN outputs. We could use the TMR based readout scheme to identify the state of the magnet, which a computer vision application would use as the solution to the problem. We simulated five different images

Table 6.2. Comparison of number of SDS magnets and VS magnets from fabricated patterns. The disk Diameter is 110 nm , 10 nm FM2 thickness [151] with STRAN output

Region	Observed SDS magnets from MFM	Observed VS magnets from MFM
1	100%	100%
2	100%	100%
3	100%	100%

using 3×3 , 5×5 and 6×6 STRANs and captured the salient and non-salient edge segments which matched with the expected output.

6.6 Conclusion

In this work, we have explored a computing grid using nanomagnets that could be easily reprogrammable. We have evaluated the design by using circular nanomagnetic grid directly solving a non-Boolean quadratic optimization problem and Boolean computation by harnessing energy minimization aspects of nanomagnets. In the past, Sarkar *et al.* have already shown this type of computation using mono-layer pillar nanomagnets using magnetic fields. Unlike the field based computing, our spin-torque driven programmable grid could operate for 2^n layouts. In this work, we have presented micromagnetic simulations backed up by relevant experimental verification, to match the results obtained from our programmable grid. We have also presented our unique way of selecting particular cells from the array to only participate in the computation, while the deselected cells through ST current will be in non-computing oscillating states. The key aspect of our programmable grid is that any quadratic optimization problem, which could be non-Boolean, can be mapped to our programmable grid, which is easier to fabricate than being individual layouts.

CHAPTER 7

CONCLUSION

This research work blends two different research areas of multilayer nanomagnetic systems and dipolar coupling between nanomagnetic disks, where we have explored novel nanomagnetic computing paradigm is investigated. The transistor technology in today's digital electronic devices uses two conductance states "0" and "1". If more charges are present in the channel then the transistor is in "ON" state and if less number of charges then the transistor is in "OFF" state. The problem happens when the transistor is switching from one to another and vice versa. When the transistor is switching, the charges in the channel moves out or goes through the channel. This movement of charges creates current flow and thereby huge power is dissipated from the transistor. This power dissipation poses a huge threat to the CMOS scaling of the devices. There are several techniques to counter this threat. One of the approach is the magnetic field based computing proposed by Imre in 2006 [112]. This work is focused such magnetic field based computing based on multilayer nanomagnetic systems. Our group has been actively working on the logic computation verifying the non-Boolean computing nature of nanomagnets to solve optimization problems that arises in computer vision. We have reviewed all the fundamental devices in multilayer spintronic devices for logic computation.

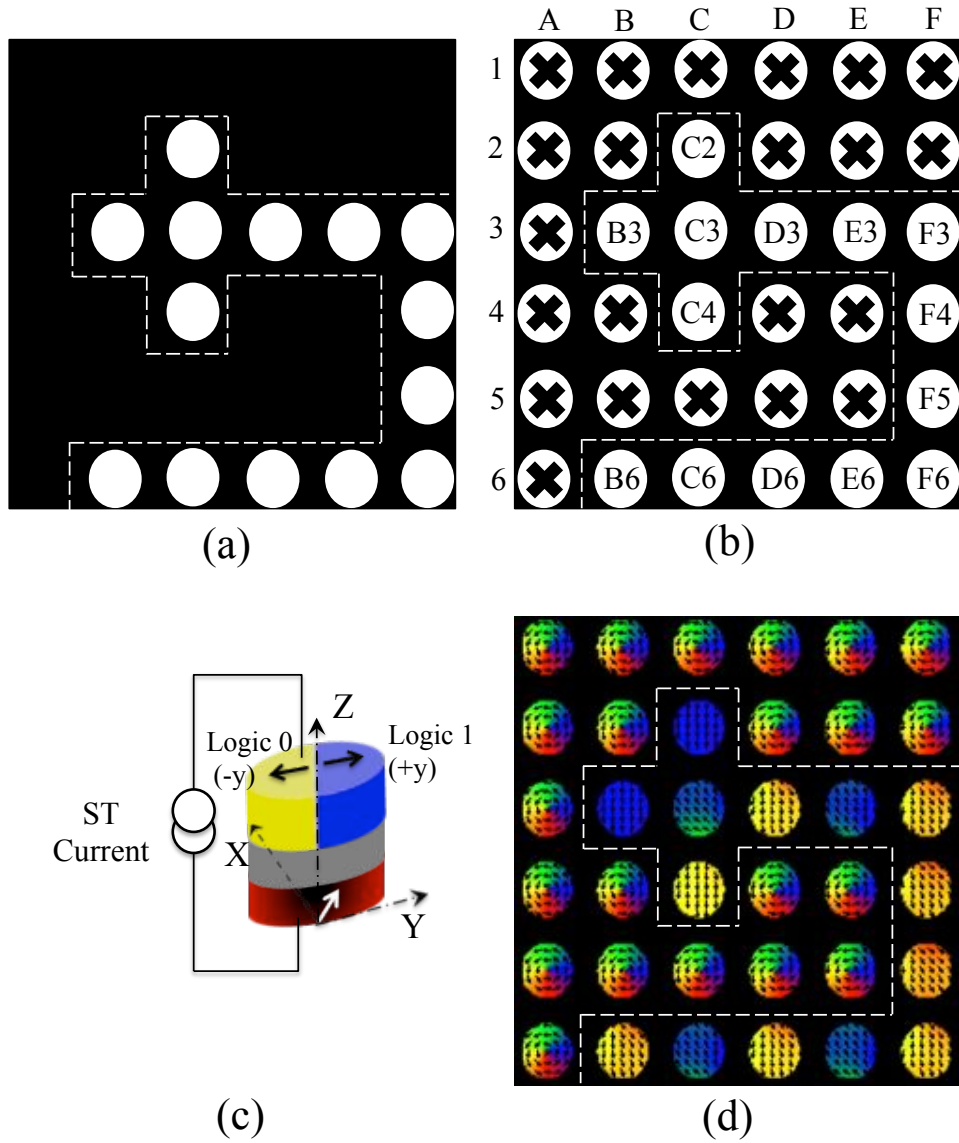


Figure 7.1. OR gate operation using a 6 x 6 MRAM reconfigurable array

7.1 Future Work - Extension of Reconfigurable Nanomagnetic Grids for Boolean Computation

Here we propose our crossbar architecture based STRAN, which has several advantages that could improve the logic density through easy programmability for constructing Boolean logic functions. In this system, the shape anisotropy provides two stable magnetization

directions encoded with classical binary bits “0” and “1” as shown in Fig. 7.1(c). The cells are deselected by passing a short ST current of $200\mu\text{A}$ for few nanoseconds to allow the magnets to settle in non-interacting vortex states. We have demonstrated a 3-input OR/NOR gate design mapped to STRAN with fanout as shown in Table. 7.1 & Fig. 7.1(a). The MTJ elements have the dimension $110 \times 100 \times 10 \text{ nm}^3$ with a tilted reference layer for readout. The inputs for this layout are B3, C2 and C4 and the fan-outs are from D3, E3 to B6 shown in Fig. 7.1(b). The Boolean operation is performed in three steps. The first step, named “DESELECT”, deselected the non-computing magnets from the grid by forcing them to non-interacting vortex state, by passing a ST current of $200\mu\text{A}$. The ST current carries the free layer magnetization of these cells to a precessional state and once released quickly they settle to their energy minimum vortex states with almost zero interaction with its neighbors. The second step, named “SET”, sets the inputs of the free layer to an initial logic state. In this step, input cells B3, C2 are set to 1 and C4 is set to 0 respectively. The third step, which is “CLOCKING and OUTPUT” clocks the output magnets to +y direction with ST current of $200\mu\text{A}$ in which the MTJ output is dependent on the inputs. The initial and final state of magnetization of the output cell C3 is shown in Fig. 7.2. As one can see the clocked magnetization of the cell C3 in +x direction settles in its ground state to +y direction depending on the inputs given to the logic circuit. We have extracted the magnetization state diagram for all input combinations. Using our STRAN many different logic designs can be produced in the same integrated circuit, by enabling users to create their own custom design. Our future work is related on fabricating this patterned STRAN and observing the programmability for Boolean or Non-Boolean computing.

7.2 Programmable Nanomagnetic Grids using Multiferroic Structures

The multiferroic devices has been of great interest in the past few years as beyond CMOS devices [152, 153, 154]. The main applications of these devices are sensors, memory and spin-

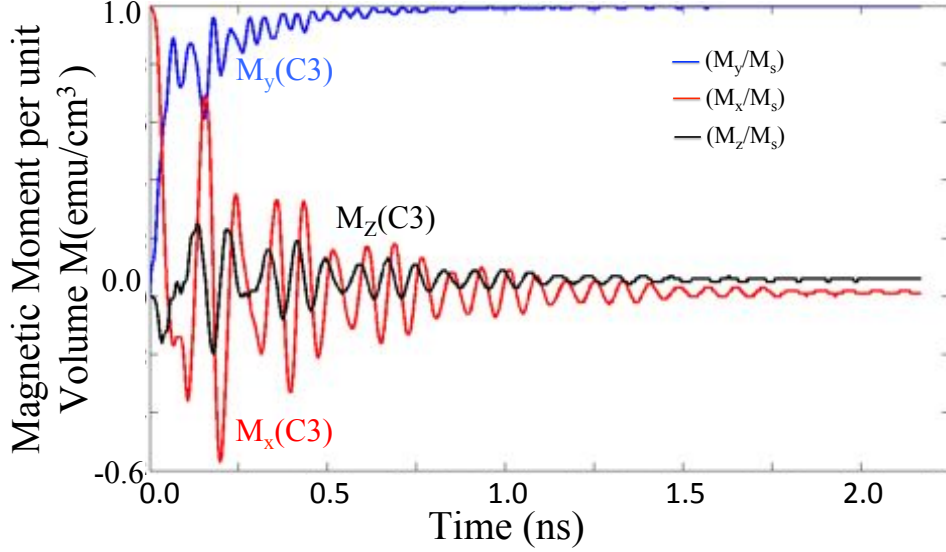


Figure 7.2. Magnetization state of cell C3

Table 7.1. Logic-OR and NOR gates programmed in a 6x6 array of nanomagnets

Input A (Cell B3)	Input B (Cell C2)	Input C (Cell C4)	Output (Cell C3) OR Gate	Fan-Out (Cell B6) NOR Gate
1	0	0	0	1
1	0	1	1	0
1	1	0	1	0
1	1	1	1	0

tronic devices. We have explored Boolean logic computation using multiferroic devices as computational elements. As proposed in this section, we are using the underneath PZT material to induce strain in the top free layer. The free layer material can be any multiferroic material and we have chosen TERFENOL-D as the free layer material, which has excellent multiferroic characteristics. The saturation magnetization, which is the most important parameter with the crystalline anisotropy parameters were carefully embedded into the simulator. As the first design exploration, we are planning to set up experiments to validate the ferromagnetic and antiferromagnetic coupling between the free layers of the multiferroic structure. We hope that, by applying strain at the bottom layer, we can induce magnetiza-

tion clocking in one of the multiferroic device and released to settle in its energy minimum state where it couples with the neighboring free layer. Once we have validated these building blocks of ferro and antiferro coupling for logic computation, we will incorporate these devices into the programmable array with both circular and elliptical shaped nanomagnetic pillars to validate the results from our STRAN hardware. A schematic of this proposed structure is shown in Fig. 7.3.

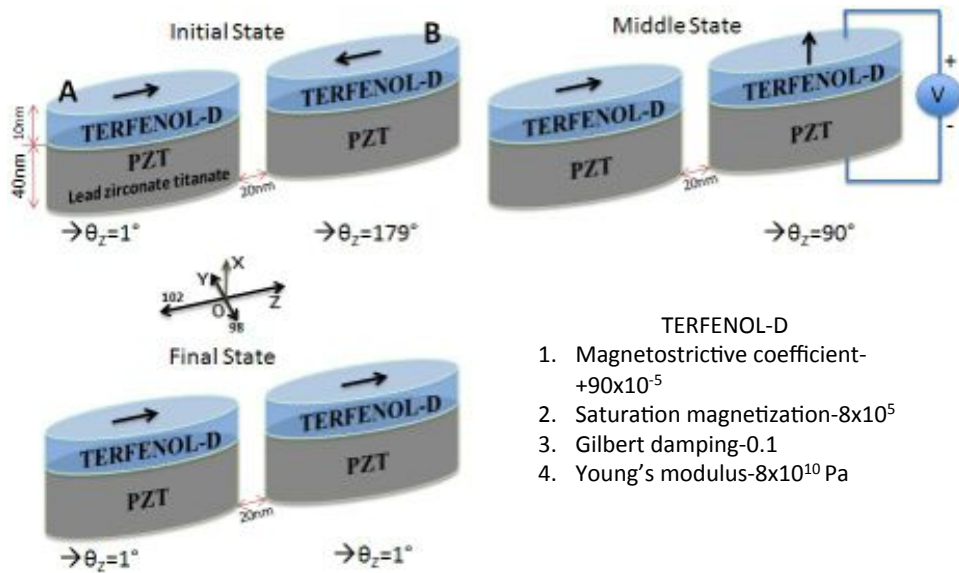


Figure 7.3. Dipolar interaction between multiferroic structures

REFERENCES

- [1] Stuart A Wolf, Jiwei Lu, Mircea R Stan, Eugene Chen, and Daryl M Treger. The promise of nanomagnetism and spintronics for future logic and universal memory. *Proceedings of the IEEE*, 98(12):2155–2168, 2010.
- [2] A. Imre, G. Csaba, L. Ji, A. Orlov, G. H. Bernstein, and W. Porod. Majority logic gate for magnetic quantum-dot cellular automata. *Science*, 311(5758):205–208, 2006.
- [3] Anita Kumari, Sudeep Sarkar, Javier F. Pulecio, D. K. Karunaratne, and Sanjukta Bhanja. Study of magnetization state transition in closely spaced nanomagnet two-dimensional array for computation. *JAP*, 109(7):07E513, 2011.
- [4] S. Sarkar and S. Bhanja. Direct quadratic minimization using magnetic field-based computing. In *NDCS, IEEE*, pages 31–34, sept. 2008.
- [5] Ashok K Sharma. *Advanced semiconductor memories: architectures, designs, and applications*. Wiley-IEEE Press, 2009.
- [6] Leland Chang, David M Fried, Jack Hergenrother, Jeffrey W Sleight, Robert H Dennard, Robert K Montoye, Lidija Sekaric, Sharee J McNab, Anna W Topol, Charlotte D Adams, et al. Stable sram cell design for the 32 nm node and beyond. In *VLSI Technology, 2005. Digest of Technical Papers. 2005 Symposium on*, pages 128–129. IEEE, 2005.
- [7] David E Kotecki. A review of high dielectric materials for dram capacitors. *Integrated Ferroelectrics*, 16(1-4):1–19, 1997.
- [8] David J Frank, Robert H Dennard, Edward Nowak, Paul M Solomon, Yuan Taur, and Hen-Sum Philip Wong. Device scaling limits of si mosfets and their application dependencies. *Proceedings of the IEEE*, 89(3):259–288, 2001.
- [9] Kiyoo Itoh, Yoshinobu Nakagome, Shin’ichiro Kimura, and Takao Watanabe. Limitations and challenges of multigigabit dram chip design. *Solid-State Circuits, IEEE Journal of*, 32(5):624–634, 1997.
- [10] Benjamin C Lee, Engin Ipek, Onur Mutlu, and Doug Burger. Architecting phase change memory as a scalable dram alternative. *ACM SIGARCH Computer Architecture News*, 37(3):2–13, 2009.

- [11] Gary Forni, Collin Ong, Christine Rice, Ken McKee, and Ronald J Bauer. Flash memory applications. *Nonvolatile Memory Technologies with Emphasis on Flash: A Comprehensive Guide to Understanding and Using NVM Devices*, pages 19–62, 2007.
- [12] Yuan-Hao Chang, Jen-Wei Hsieh, and Tei-Wei Kuo. Endurance enhancement of flash-memory storage systems: an efficient static wear leveling design. In *Proceedings of the 44th annual Design Automation Conference*, pages 212–217. ACM, 2007.
- [13] P Cappelletti, R Bez, D Cantarelli, and L Fratin. Failure mechanisms of flash cell in program/erase cycling. In *Electron Devices Meeting, 1994. IEDM'94. Technical Digest., International*, pages 291–294. IEEE, 1994.
- [14] Robert S Patti. Three-dimensional integrated circuits and the future of system-on-chip designs. *Proceedings of the IEEE*, 94(6):1214–1224, 2006.
- [15] CJ Lin, SH Kang, YJ Wang, K Lee, X Zhu, WC Chen, X Li, WN Hsu, YC Kao, MT Liu, et al. 45nm low power cmos logic compatible embedded stt mram utilizing a reverse-connection 1t/1mtj cell. In *Electron Devices Meeting (IEDM), 2009 IEEE International*, pages 1–4. IEEE, 2009.
- [16] Xiangyu Dong, Xiaoxia Wu, Guangyu Sun, Yuan Xie, Helen Li, and Yiran Chen. Circuit and microarchitecture evaluation of 3d stacking magnetic ram (mram) as a universal memory replacement. In *Design Automation Conference, 2008. DAC 2008. 45th ACM/IEEE*, pages 554–559. IEEE, 2008.
- [17] Kenji Tsuchida, Tsuneo Inaba, Katsuyuki Fujita, Yoshihiro Ueda, Takafumi Shimizu, Yoshiaki Asao, Takeshi Kajiyama, Masayoshi Iwayama, Kuniaki Sugiura, Sumio Ikegawa, et al. Isscc 2010/session 14/non-volatile memory/14.2. 2010.
- [18] Kumiko Nomura, Keiko Abe, Hiroaki Yoda, and Shinobu Fujita. Ultra low power processor using perpendicular-stt-mram/sram based hybrid cache toward next generation normally-off computers. *Journal of Applied Physics*, 111(7):07E330–07E330, 2012.
- [19] Said Tehrani, JM Slaughter, E Chen, M Durlam, J Shi, and M DeHerren. Progress and outlook for mram technology. *Magnetics, IEEE Transactions on*, 35(5):2814–2819, 1999.
- [20] Xiaochun Zhu and Jian-Gang Zhu. Spin torque and field-driven perpendicular mram designs scalable to multi-gb/chip capacity. *Magnetics, IEEE Transactions on*, 42(10):2739–2741, 2006.
- [21] AV Khvalkovskiy, D Apalkov, S Watts, R Chepulskaa, RS Beach, A Ong, X Tang, A Driskill-Smith, WH Butler, PB Visscher, et al. Basic principles of stt-mram cell operation in memory arrays. *Journal of Physics D: Applied Physics*, 46(7):74001–74020, 2013.

- [22] Shinji Yuasa, Taro Nagahama, Akio Fukushima, Yoshishige Suzuki, and Koji Ando. Giant room-temperature magnetoresistance in single-crystal fe/mgo/fe magnetic tunnel junctions. *Nature materials*, 3(12):868–871, 2004.
- [23] Wei Xu, Hongbin Sun, Xiaobin Wang, Yiran Chen, and Tong Zhang. Design of last-level on-chip cache using spin-torque transfer ram (stt ram). *Very Large Scale Integration (VLSI) Systems, IEEE Transactions on*, 19(3):483–493, 2011.
- [24] Z. Weisheng *et al.* Design of mram based logic circuits and its applications. In *GLSVLSI, GLSVLSI '11*, pages 431–436, New York, NY, USA, 2011. ACM.
- [25] R Beach, T Min, C Horng, Q Chen, P Sherman, S Le, S Young, K Yang, H Yu, X Lu, et al. A statistical study of magnetic tunnel junctions for high-density spin torque transfer-mram (stt-mram). In *Electron Devices Meeting, 2008. IEDM 2008. IEEE International*, pages 1–4. IEEE, 2008.
- [26] Jung Pill Kim, Taehyun Kim, Wuyang Hao, Hari M Rao, Kangho Lee, Xiaochun Zhu, Xia Li, Wah Hsu, Seung H Kang, Nowak Matt, et al. A 45nm 1mb embedded stt-mram with design techniques to minimize read-disturbance. In *VLSI Circuits (VLSIC), 2011 Symposium on*, pages 296–297. IEEE, 2011.
- [27] Young Min Lee, Chikakko Yoshida, Koji Tsunoda, Shinjiro Umehara, Masaki Aoki, and Toshihiro Sugii. Highly scalable stt-mram with mtjs of top-pinned structure in 1t/1mtj cell. In *VLSI Technology (VLSIT), 2010 Symposium on*, pages 49–50. IEEE, 2010.
- [28] STMicroelectronics. The nvrn. <http://www.ief.u-psud.fr/~zhao/papers/2012/IMWSTTMRAM.pdf>, 2012.
- [29] Yi Gang, Weisheng Zhao, J-O Klein, Claude Chappert, and Pascale Mazoyer. A high-reliability, low-power magnetic full adder. *Magnetics, IEEE Transactions on*, 47(11):4611–4616, 2011.
- [30] Weisheng Zhao, Eric Belhaire, Bernard Dieny, Guillaume Prenat, and Claude Chappert. Tas-mram based non-volatile fpga logic circuit. In *Field-Programmable Technology, 2007. ICFPT 2007. International Conference on*, pages 153–160. IEEE, 2007.
- [31] Victor Silva, Luís Bica Oliveira, Jorge R Fernandes, Mário P Véstias, and Horácio C Neto. Run-time reconfigurable array using magnetic ram. In *Digital System Design, Architectures, Methods and Tools, 2009. DSD'09. 12th Euromicro Conference on*, pages 74–81. IEEE, 2009.
- [32] Weisheng Zhao, Dafine Ravelosona, J Klein, and Claude Chappert. Domain wall shift register-based reconfigurable logic. *Magnetics, IEEE Transactions on*, 47(10):2966–2969, 2011.

- [33] Yahya Lakys, Weisheng Zhao, Jacques-Olivier Klein, and Claude Chappert. Magnetic look-up table (mlut) featuring radiation hardness, high performance and low power. In *Reconfigurable Computing: Architectures, Tools and Applications*, pages 275–280. Springer, 2011.
- [34] Dan A Allwood, Gang Xiong, CC Faulkner, D Atkinson, D Petit, and RP Cowburn. Magnetic domain-wall logic. *Science*, 309(5741):1688–1692, 2005.
- [35] DA Allwood, Gang Xiong, MD Cooke, CC Faulkner, D Atkinson, N Vernier, and RP Cowburn. Submicrometer ferromagnetic not gate and shift register. *Science*, 296(5575):2003–2006, 2002.
- [36] G Hrkac, J Dean, and DA Allwood. Nanowire spintronics for storage class memories and logic. *Philosophical Transactions of the Royal Society A: Mathematical, Physical and Engineering Sciences*, 369(1948):3214–3228, 2011.
- [37] Jean Anne Currivan, Youngman Jang, Mark D Mascaro, Marc A Baldo, and Caroline A Ross. Low energy magnetic domain wall logic in short, narrow, ferromagnetic wires. *Magnetics Letters, IEEE*, 3:3000104–3000104, 2012.
- [38] Paul R Gray and Robert G Meyer. *Analysis and design of analog integrated circuits*. John Wiley & Sons, Inc., 1990.
- [39] Norman Einspruch. *Advanced MOS device physics*. Elsevier, 2012.
- [40] Ben G Streetman and Sanjay Banerjee. *Solid state electronic devices*, volume 4. Prentice Hall Englewood Cliffs, NJ, 1995.
- [41] Phillip E Allen, Douglas R Holberg, Phillip E Allen, and PE Allen. *CMOS analog circuit design*. Holt, Rinehart and Winston New York, 1987.
- [42] Neil HE Weste and Kamran Eshraghian. Principles of cmos vlsi design: a systems perspective. *NASA STI/Recon Technical Report A*, 85:47028, 1985.
- [43] Carver A Mead. Scaling of mos technology to submicrometer feature sizes. *Journal of VLSI signal processing systems for signal, image and video technology*, 8(1):9–25, 1994.
- [44] Claudio Fiegna, Hiroshi Iwai, Tetsunori Wada, Masanobu Saito, Enrico Sangiorgi, and Bruno Ricco. Scaling the mos transistor below 0.1 μm : methodology, device structures, and technology requirements. *Electron Devices, IEEE Transactions on*, 41(6):941–951, 1994.
- [45] Paul S Peercy. The drive to miniaturization. *Nature*, 406(6799):1023–1026, 2000.
- [46] JULIO S EDGAR LILIENFELD. Method and apparatus for controlling electric currents, January 28 1930. US Patent 1,745,175.

- [47] Bruce Hoeneisen and Carver A Mead. Fundamental limitations in microelectronics. mos technology. *Solid-State Electronics*, 15(7):819–829, 1972.
- [48] HL Hughes and JM Benedetto. Radiation effects and hardening of mos technology: devices and circuits. *Nuclear Science, IEEE Transactions on*, 50(3):500–521, 2003.
- [49] Naohiko Kimizuka, Toyoji Yamamoto, Tohru Mogami, Ken Yamaguchi, Kazuhiro Imai, and T Horiuchi. The impact of bias temperature instability for direct-tunneling ultra-thin gate oxide on mosfet scaling. In *VLSI Technology, 1999. Digest of Technical Papers. 1999 Symposium on*, pages 73–74. IEEE, 1999.
- [50] TY Chan, J Chen, PK Ko, and C Hu. The impact of gate-induced drain leakage current on mosfet scaling. In *Electron Devices Meeting, 1987 International*, volume 33, pages 718–721. IEEE, 1987.
- [51] Hang Hu, Jarvis B Jacobs, Lisa T Su, and Dimitri A Antoniadis. A study of deep-submicron mosfet scaling based on experiment and simulation. *Electron Devices, IEEE Transactions on*, 42(4):669–677, 1995.
- [52] James A Hutchby, George I Bourianoff, Victor V Zhirnov, and Joe E Brewer. Extending the road beyond cmos. *Circuits and Devices Magazine, IEEE*, 18(2):28–41, 2002.
- [53] Alan C Seabaugh and Qin Zhang. Low-voltage tunnel transistors for beyond cmos logic. *Proceedings of the IEEE*, 98(12):2095–2110, 2010.
- [54] John H Reif. The design of autonomous dna nano-mechanical devices: Walking and rolling dna. *Natural Computing*, 2(4):439–461, 2003.
- [55] Jeffrey J Welsler, George I Bourianoff, Victor V Zhirnov, and Ralph Keary Cavin III. The quest for the next information processing technology. *Journal of Nanoparticle Research*, 10(1):1–10, 2008.
- [56] BS Doyle, S Datta, M Doczy, S Hareland, B Jin, J Kavalieros, T Linton, A Murthy, R Rios, and R Chau. High performance fully-depleted tri-gate cmos transistors. *Electron Device Letters, IEEE*, 24(4):263–265, 2003.
- [57] Jack Kavalieros, Brian Doyle, Suman Datta, Gilbert Dewey, Mark Doczy, Ben Jin, Dan Lionberger, Matthew Metz, Willy Rachmady, Marko Radosavljevic, et al. Tri-gate transistor architecture with high-k gate dielectrics, metal gates and strain engineering. In *VLSI Technology, 2006. Digest of Technical Papers. 2006 Symposium on*, pages 50–51. IEEE, 2006.
- [58] T Naito, T Ishida, T Onoduka, M Nishigoori, T Nakayama, Y Ueno, Y Ishimoto, A Suzuki, W Chung, R Madurawe, et al. World’s first monolithic 3d-fpga with tft sram over 90nm 9 layer cu cmos. In *VLSI Technology (VLSIT), 2010 Symposium on*, pages 219–220. IEEE, 2010.

- [59] Satish Damaraju, Varghese George, Sanjeev Jahagirdar, Tanveer Khondker, Robert Milstrey, Sanjib Sarkar, Scott Siers, Israel Stolero, and Arun Subbiah. A 22nm ia multi-cpu and gpu system-on-chip. In *Solid-State Circuits Conference Digest of Technical Papers (ISSCC), 2012 IEEE International*, pages 56–57. IEEE, 2012.
- [60] Nasser Kurd, Muntaquim Chowdhury, Edward Burton, Thomas P Thomas, Christopher Mozak, Brent Boswell, Manoj Lal, Anant Deval, Jonathan Douglas, Mahmoud Ellassal, et al. 5.9 haswell: A family of ia 22nm processors. In *Solid-State Circuits Conference Digest of Technical Papers (ISSCC), 2014 IEEE International*, pages 112–113. IEEE, 2014.
- [61] Luqiao Liu, Chi-Feng Pai, Y Li, HW Tseng, DC Ralph, and RA Buhrman. Spin-torque switching with the giant spin hall effect of tantalum. *Science*, 336(6081):555–558, 2012.
- [62] Chi-Feng Pai, Luqiao Liu, Y Li, HW Tseng, DC Ralph, and RA Buhrman. Spin transfer torque devices utilizing the giant spin hall effect of tungsten. *Applied Physics Letters*, 101(12):122404, 2012.
- [63] SA Wolf, DD Awschalom, RA Buhrman, JM Daughton, S Von Molnar, ML Roukes, A Yu Chtchelkanova, and DM Treger. Spintronics: a spin-based electronics vision for the future. *Science*, 294(5546):1488–1495, 2001.
- [64] Lapo Bogani and Wolfgang Wernsdorfer. Molecular spintronics using single-molecule magnets. *Nature materials*, 7(3):179–186, 2008.
- [65] Mario Norberto Baibich, JM Broto, Albert Fert, F Nguyen Van Dau, F Petroff, P Etienne, G Creuzet, A Friederich, and J Chazelas. Giant magnetoresistance of (001) fe/(001) cr magnetic superlattices. *Physical Review Letters*, 61(21):2472, 1988.
- [66] Albert Fert. Nobel lecture: Origin, development, and future of spintronics. *Reviews of Modern Physics*, 80(4):1517, 2008.
- [67] Albert Fert. The present and the future of spintronics. *Thin Solid Films*, 517(1):2–5, 2008.
- [68] William J Gallagher and Stuart SP Parkin. Development of the magnetic tunnel junction mram at ibm: From first junctions to a 16-mb mram demonstrator chip. *IBM Journal of Research and Development*, 50(1):5–23, 2006.
- [69] Stuart SP Parkin, Masamitsu Hayashi, and Luc Thomas. Magnetic domain-wall race-track memory. *Science*, 320(5873):190–194, 2008.
- [70] Ching Tsang, Robert E Fontana, Tsann Lin, David E Heim, Virgil S Speriosu, Bruce A Gurney, and Mason L Williams. Design, fabrication and testing of spin-valve read heads for high density recording. *Magnetics, IEEE Transactions on*, 30(6):3801–3806, 1994.

- [71] Ching H Tsang, Robert E Fontana Jr, Tsann Lin, David E Heim, Bruce A Gurney, and ML Williams. Design, fabrication, and performance of spin-valve read heads for magnetic recording applications. *IBM journal of research and development*, 42(1):103–116, 1998.
- [72] Stuart SP Parkin. Data in the fast lanes of racetrack memory. *Scientific American*, 300(6):76–81, 2009.
- [73] Alan S Edelstein and Gregory A Fischer. Minimizing 1/f noise in magnetic sensors using a microelectromechanical system flux concentrator. *Journal of applied physics*, 91(10):7795–7797, 2002.
- [74] Jian-Gang Jimmy Zhu and Chando Park. Magnetic tunnel junctions. *Materials Today*, 9(11):36–45, 2006.
- [75] BN Engel, J Akerman, B Butcher, RW Dave, M DeHerrera, M Durlam, G Grynkewich, J Janesky, SV Pietambaram, ND Rizzo, et al. A 4-mb toggle mram based on a novel bit and switching method. *Magnetics, IEEE Transactions on*, 41(1):132–136, 2005.
- [76] Johan Åkerman. Toward a universal memory. *Science*, 308(5721):508–510, 2005.
- [77] Daniel Christopher Worledge. Single-domain model for toggle mram. *IBM journal of research and development*, 50(1):69–79, 2006.
- [78] MD Stiles and A Zangwill. Anatomy of spin-transfer torque. *Physical Review B*, 66(1):014407, 2002.
- [79] Mark D Stiles and Jacques Miltat. Spin-transfer torque and dynamics. In *Spin dynamics in confined magnetic structures III*, pages 225–308. Springer, 2006.
- [80] Akinobu Yamaguchi, Teruo Ono, Saburo Nasu, Kousaku Miyake, Ko Mibu, and Teruya Shinjo. Real-space observation of current-driven domain wall motion in submicron magnetic wires. *Physical Review Letters*, 92(7):077205, 2004.
- [81] IN Krivorotov, NC Emley, JC Sankey, SI Kiselev, DC Ralph, and RA Buhrman. Time-domain measurements of nanomagnet dynamics driven by spin-transfer torques. *Science*, 307(5707):228–231, 2005.
- [82] Jonathan Z Sun. Spin angular momentum transfer in current-perpendicular nanomagnetic junctions. *IBM journal of research and development*, 50(1):81–100, 2006.
- [83] WF Brinkman, RC Dynes, and JM Rowell. Tunneling conductance of asymmetrical barriers. *Journal of Applied Physics*, 41(5):1915–1921, 2003.
- [84] L-B Faber, Weisheng Zhao, J-O Klein, Thibaut Devolder, and Claude Chappert. Dynamic compact model of spin-transfer torque based magnetic tunnel junction (mtj). In *Design & Technology of Integrated Systems in Nanoscale Era, 2009. DTIS'09. 4th International Conference on*, pages 130–135. IEEE, 2009.

- [85] John C Slonczewski. Initiation of spin-transfer torque by thermal transport from magnons. *Physical Review B*, 82(5):054403, 2010.
- [86] Morgan Madec, J Kammerer, Fabien Pregaldiny, Luc Hebrard, and Christophe Lallement. Compact modeling of magnetic tunnel junction. In *Circuits and Systems and TAISA Conference, 2008. NEWCAS-TAISA 2008. 2008 Joint 6th International IEEE Northeast Workshop on*, pages 229–232. IEEE, 2008.
- [87] Ethan L Miller, Scott A Brandt, and Darrell DE Long. Hermes: High-performance reliable mram-enabled storage. In *Hot Topics in Operating Systems, 2001. Proceedings of the Eighth Workshop on*, pages 95–99. IEEE, 2001.
- [88] JM Slaughter, RW Dave, M Durlam, G Kerszykowski, K Smith, K Nagel, B Feil, J Calder, M DeHerrera, B Garni, et al. High speed toggle mram with mgo-based tunnel junctions. In *Electron Devices Meeting, 2005. IEDM Technical Digest. IEEE International*, pages 873–876. IEEE, 2005.
- [89] EB Myers, FJ Albert, JC Sankey, E Bonet, RA Buhrman, and DC Ralph. Thermally activated magnetic reversal induced by a spin-polarized current. *Physical Review Letters*, 89(19):196801, 2002.
- [90] Sergei Urazhdin, Norman O Birge, WP Pratt Jr, and J Bass. Current-driven magnetic excitations in permalloy-based multilayer nanopillars. *Physical review letters*, 91(14):146803, 2003.
- [91] DM Apalkov and PB Visscher. Spin-torque switching: Fokker-planck rate calculation. *Physical Review B*, 72(18):180405, 2005.
- [92] Michael. R Scheinfein. LLG Micromagnetic Simulator, 1997.
- [93] M Speckmann, HP Oepen, and H Ibach. Magnetic domain structures in ultrathin co/au (111): on the influence of film morphology. *Physical review letters*, 75(10):2035, 1995.
- [94] RJ Enkin and DJ Dunlop. A micromagnetic study of pseudo single-domain remanence in magnetite. *Journal of Geophysical Research: Solid Earth (1978–2012)*, 92(B12):12726–12740, 1987.
- [95] Wyn Williams and David J Dunlop. Three-dimensional micromagnetic modelling of ferromagnetic domain structure. *Nature*, 337(6208):634–637, 1989.
- [96] JA Katine, FJ Albert, RA Buhrman, EB Myers, and DC Ralph. Current-driven magnetization reversal and spin-wave excitations in co/cu/co pillars. *Physical Review Letters*, 84(14):3149, 2000.
- [97] R Coldea, SM Hayden, G Aeppli, TG Perring, CD Frost, TE Mason, S-W Cheong, and Z Fisk. Spin waves and electronic interactions in la₂cuo₄. *Physical review letters*, 86(23):5377, 2001.

- [98] M Hatherly, K Hirakawa, RD Lowde, JF Mallett, MW Stringfellow, and BH Torrie. Spin wave energies and exchange parameters in iron-nickel alloys. *Proceedings of the Physical Society*, 84(1):55, 1964.
- [99] E. Varga, A. Orlov, M.T. Niemier, X.S. Hu, G.H. Bernstein, and W. Porod. Experimental demonstration of fanout for nanomagnetic logic. *Nanotechnology, IEEE Transactions on*, 9(6):668–670, Nov 2010.
- [100] Javier F. Pulecio and Sanjukta Bhanja. Magnetic cellular automata coplanar cross wire systems. *Journal of Applied Physics*, 107(3):–, 2010.
- [101] R. P. Cowburn and M. E. Welland. Room temperature magnetic quantum cellular automata. *Science*, 287(5457):1466–1468, 2000.
- [102] M. Niemier, X.S. Hu, A. Dingler, M.T. Alam, G. Bernstein, and W. Porod. Bridging the gap between nanomagnetic devices and circuits. In *ICCD 2008.*, pages 506 –513, oct. 2008.
- [103] Andrew Lyle, Angeline Klemm, Jonathan Harms, Yisong Zhang, Hui Zhao, and Jian-Ping Wang. Probing dipole coupled nanomagnets using magnetoresistance read. *Applied Physics Letters*, 98(9):092502, 2011.
- [104] G. Csaba, A. Imre, G.H. Bernstein, W. Porod, and V. Metlushko. Nanocomputing by field-coupled nanomagnets. *Nanotechnology, IEEE Transactions on*, 1(4):209 – 213, dec 2002.
- [105] Charles Augustine, Behtash Behin-Aein, Xuanyao Fong, and Kaushik Roy. A design methodology and device/circuit/architecture compatible simulation framework for low-power magnetic quantum cellular automata systems. ASP-DAC '09, pages 847–852, 2009.
- [106] Behtash Behin-Aein, Deepanjan Datta, Sayeef Salahuddin, and Supriyo Datta. Proposal for an all-spin logic device with built-in memory. 2010.
- [107] Shiliang Liu, X.S. Hu, J.J. Nahas, M.T. Niemier, W. Porod, and G.H. Bernstein. Magnetic-electrical interface for nanomagnet logic. *Nanotechnology, IEEE Transactions on*, 10(4):757 –763, july 2011.
- [108] P.M. Braganca, J.A. Katine, N.C. Emley, D. Mauri, J.R. Childress, P.M. Rice, E. Delenia, D.C. Ralph, and R.A. Buhrman. A three-terminal approach to developing spin-torque written magnetic random access memory cells. *Nanotechnology, IEEE Transactions on*, 8(2):190 –195, march 2009.
- [109] Giorgio Bertotti, Claudio Serpico, and Isaak D. Mayergoyz. Nonlinear magnetization dynamics under circularly polarized field. *Phys. Rev. Lett.*, 86:724–727, Jan 2001.
- [110] S. Rajaram *et al.* Study of dipolar neighbor interaction on magnetization states of nano-magnetic disks. *IEEE Trans. Magn.*, 49(7):3129–3132, 2013.

- [111] R. P. Cowburn and M. E. Welland. Room temperature magnetic quantum cellular automata. *Science*, 287(5457):1466–1468, 2000.
- [112] A. Imre, G. Csaba, L. Ji, A. Orlov, G. H. Bernstein, and W. Porod. Majority logic gate for magnetic quantum-dot cellular automata. *Science*, 311(5758):205–208, 2006.
- [113] M.T. Alam, S. Kurtz, M.T. Niemier, S.X. Hu, G.H. Bernstein, and W. Porod. Magnetic logic based on coupled nanomagnets: Clocking structures and power analysis. In *Nano., IEEE*, page 637, aug. 2008.
- [114] K. Bernstein, R.K. Cavin, W. Porod, A. Seabaugh, and J. Welser. Device and architecture outlook for beyond cmos switches. *Proc. IEEE*, 98(12):2169 –2184, dec. 2010.
- [115] Johan Akerman. Toward a universal memory. *Science*, 308(5721):508–510, 2005.
- [116] J.M. Slaughter. Recent advances in mram technology. In *Device Research Conf., 2007 65th Annual*, pages 245 –246, june 2007.
- [117] A. Wachowiak, J. Wiebe, M. Bode, O. Pietzsch, M. Morgenstern, and R. Wiesendanger. Direct observation of internal spin structure of magnetic vortex cores. *Science*, 298:577–580, 2002.
- [118] F. Boust and N. Vukadinovic. Micromagnetic simulations of vortex resonances in coupled nanodisks. *IEEE Trans. Magn.*, 47(2):349 –354, feb. 2011.
- [119] W. Scholz *et al.* Transition from single-domain to vortex state in soft magnetic cylindrical nanodots. *J MAGN MAGN MATER*, 266(12):155 – 163, 2003.
- [120] Roman Verba *et al.* Collective spin-wave excitations in a two-dimensional array of coupled magnetic nanodots. *Phys. Rev. B*, 85:014427, Jan 2012.
- [121] P.-O. Jubert and R. Allenspach. Analytical approach to the single-domain-to-vortex transition in small magnetic disks. *Phys. Rev. B*, 70:144402, Oct 2004.
- [122] H. Hoffmann and F. Steinbauer. Single domain and vortex state in ferromagnetic circular nanodots. *JAP*, 92(9):5463 –5467, nov 2002.
- [123] A. J. Bennett and J. M. Xu. Simulating collective magnetic dynamics in nanodisk arrays. *APL*, 82(15):2503 –2505, apr 2003.
- [124] J. Mejía-López, D. Altbir, A. H. Romero, X. Batlle, Igor V. Roshchin, Chang-Peng Li, and Ivan K. Schuller. Vortex state and effect of anisotropy in sub-100-nm magnetic nanodots. *JAP*, 100(10):104319, 2006.
- [125] Gavin S Abo, Yang-Ki Hong, Byoung-Chul Choi, Michael J Donahue, Seok Bae, Jeevan Jalli, Jihoon Park, Jaejin Lee, Mun-Hyoun Park, and Sung-Hoon Gee. Micromagnetic computer simulated scaling effect of s-shaped permalloy nano-element on operating fields for and or or logic. *Magnetics, IEEE Transactions on*, 48(5):1851–1855, 2012.

- [126] L. Hu and T. Hesjedal. Micromagnetic investigation of the s-state reconfigurable logic element. *IEEE Trans. Magn.*, 48(7):2103–2111, July 2012.
- [127] M.J. Donahue and R.D. McMichael. Micromagnetics on curved geometries using rectangular cells: Error correction and analysis. *IEEE Trans. Magn.*, 43(6):2878–2880, June 2007.
- [128] Y. Yilmaz and P. Mazumder. Nonvolatile nanopipelining logic using multiferroic single-domain nanomagnets. *Very Large Scale Integration (VLSI) Systems, IEEE Transactions on*, 21(7):1181–1188, July 2013.
- [129] Qijun Xiao, Tianyu Yang, Andrei Ursache, and Mark T. Tuominen. Clusters of interacting single domain co nanomagnets for multistate perpendicular magnetic media applications. *Journal of Applied Physics*, 103(7):07C521–07C521–3, Apr 2008.
- [130] Li. Peng *et al.* Direct measurement of magnetic coupling between nanomagnets for nanomagnetic logic applications. *Magnetics, IEEE Transactions on*, 48(11):4402–4405, Nov 2012.
- [131] Jian-Ping Wang and Xiaofeng Yao. Programmable spintronic logic devices for reconfigurable computation and beyondhistory and outlook. *J Nanoelectron Optoe*, 2008.
- [132] W. Jianguo. *et al.* Programmable spintronics logic device based on a magnetic tunnel junction element. *J. Appl. Phys.*, 97(10):10D509–10D509, 2005.
- [133] L. Shiliang *et al.* Exploring the design of the magneticelectrical interface for nanomagnet logic. *Nanotechnology, IEEE Transactions on*, 12(2):203–214, March 2013.
- [134] Y. Xiaofeng *et al.* Magnetic tunnel junction-based spintronic logic units operated by spin transfer torque. *IEEE Trans. Nanotechnol.*, 2012.
- [135] G. Csaba and W. Porod. Computational study of spin-torque oscillator interactions for non-boolean computing applications. *Magnetics, IEEE Transactions on*, 49(7):4447–4451, July 2013.
- [136] M. Sharad, C. Augustine, and K. Roy. Boolean and non-boolean computation with spin devices. In *IEDM*, pages 11.6.1–11.6.4, 2012.
- [137] S. Sarkar and S. Bhanja. Direct quadratic minimization using magnetic field-based computing. In *Design and Test of Nano Devices, Circuits and Systems, 2008 IEEE International Workshop on*, pages 31–34, 2008.
- [138] N. DrSouza *et al.* An ultrafast image recovery and recognition system implemented with nanomagnets possessing biaxial magnetocrystalline anisotropy. *IEEE Trans. Nanotechnol.*, 2012.
- [139] B. Zhang *et al.* Reconfigurable processor for binary image processing. *IEEE Trans. Circuits Syst. Video Technol.*, 23(5):823–831, 2013.

- [140] S.P. Levitan *et al.* Non-boolean associative architectures based on nano-oscillators. In *Cellular Nanoscale Networks and Their Applications (CNNA), 2012 13th International Workshop on*, pages 1–6, Aug 2012.
- [141] J. Pulecio, S. Bhanja, and S. Sarkar. An experimental demonstration of the viability of energy minimizing computing using nano-magnets. In *IEEE-NANO*, pages 1038–1042, 2011.
- [142] WS Zhao, Thibaut Devolder, Yahya Lakys, Jacques-Olivier Klein, Claude Chappert, and Pascale Mazoyer. Design considerations and strategies for high-reliable stt-mram. *Microelectronics Reliability*, 51(9):1454–1458, 2011.
- [143] W. Zhao. *et al.* Evaluation of a non-volatile fpga based on mram technology. In *ICICDT'06*, pages 1–4. IEEE, 2006.
- [144] L. Yahya *et al.* Mram crossbar based configurable logic block. In *ISCAS*, pages 2945–2948. IEEE, 2012.
- [145] Z. Weisheng *et al.* Power and area optimization for run-time reconfiguration system on programmable chip based on magnetic random access memory. *IEEE Trans. Magn.*, 45(2):776–780, 2009.
- [146] John C Slonczewski. Current-driven excitation of magnetic multilayers. *Journal of Magnetism and Magnetic Materials*, 159(1):L1–L7, 1996.
- [147] Roberto Bonin, Giorgio Bertotti, Paolo Bortolotti, Claudio Serpico, Massimiliano d’Aquino, and Isaak D Mayergoyz. Analytical study of synchronization in spin-transfer-driven magnetization dynamics. In *Journal of Physics: Conference Series*, volume 200, page 042005. IOP Publishing, 2010.
- [148] HB Huang, XQ Ma, ZH Liu, CP Zhao, and LQ Chen. Micromagnetic simulation of high-power spin-torque oscillator in half-metallic heusler alloy spin valve nanopillar. *AIP Advances*, 3(3):032132, 2013.
- [149] SI Kiselev, JC Sankey, IN Krivorotov, NC Emley, M Rinkoski, C Perez, RA Buhrman, and DC Ralph. Current-induced nanomagnet dynamics for magnetic fields perpendicular to the sample plane. *Physical review letters*, 93(3):036601, 2004.
- [150] Giulio Siracusano and Aurelio La Corte. A comparison between advanced time-frequency analyses of non-stationary magnetization dynamics in spin-torque oscillators. *Physica B: Condensed Matter*, 2013.
- [151] R. Panchumarthy *et al.* Magnetic state estimator to characterize the magnetic states of nano-magnetic disks. *Magnetics, IEEE Transactions on*, 49(7):3545–3548, July 2013.
- [152] H Béa, M Gajek, M Bibes, and A Barthélémy. Spintronics with multiferroics. *Journal of Physics: Condensed Matter*, 20(43):434221, 2008.

- [153] D Pantel, S Goetze, D Hesse, and M Alexe. Reversible electrical switching of spin polarization in multiferroic tunnel junctions. *Nature materials*, 11(4):289–293, 2012.
- [154] Kuntal Roy, Supriyo Bandyopadhyay, and Jayasimha Atulasimha. Hybrid spintronics and straintronics: A magnetic technology for ultra low energy computing and signal processing. *Applied Physics Letters*, 99(6):063108, 2011.


APPENDICES

Appendix A Copyright Permission

The IEEE copyright permissions for reprinting the article for one of my published paper in IEEE Transactions on Magnetics included in Chapter. 5 in this dissertation is given below.

3/19/2014 Rightslink® by Copyright Clearance Center

Copyright Clearance Center RightsLink® Home Create Account Help

 **Requesting permission to reuse content from an IEEE publication**

Title: Study of Dipolar Neighbor Interaction on Magnetization States of Nano-Magnetic Disks
Author: Rajaram, S.; Karunaratne, D.K.; Sarkar, S.; Bhanja, S.
Publication: Magnetics, IEEE Transactions on
Publisher: IEEE
Date: July 2013
Copyright © 2013, IEEE

User ID
Password
 Enable Auto Login
LOGIN
[Forgot Password/User ID?](#)
If you're a copyright.com user, you can login to RightsLink using your copyright.com credentials. Already a RightsLink user or want to [learn more?](#)

Thesis / Dissertation Reuse

The IEEE does not require individuals working on a thesis to obtain a formal reuse license, however, you may print out this statement to be used as a permission grant:

Requirements to be followed when using any portion (e.g., figure, graph, table, or textual material) of an IEEE copyrighted paper in a thesis:

- 1) In the case of textual material (e.g., using short quotes or referring to the work within these papers) users must give full credit to the original source (author, paper, publication) followed by the IEEE copyright line © 2011 IEEE.
- 2) In the case of illustrations or tabular material, we require that the copyright line © [Year of original publication] IEEE appear prominently with each reprinted figure and/or table.
- 3) If a substantial portion of the original paper is to be used, and if you are not the senior author, also obtain the senior author's approval.

Requirements to be followed when using an entire IEEE copyrighted paper in a thesis:

- 1) The following IEEE copyright/ credit notice should be placed prominently in the references: © [year of original publication] IEEE. Reprinted, with permission, from [author names, paper title, IEEE publication title, and month/year of publication]
- 2) Only the accepted version of an IEEE copyrighted paper can be used when posting the paper or your thesis on-line.
- 3) In placing the thesis on the author's university website, please display the following message in a prominent place on the website: In reference to IEEE copyrighted material which is used with permission

<https://100.copyright.com/AppDispatchServlet?formTop>

3/19/2014 Rightslink® by Copyright Clearance Center

in this thesis, the IEEE does not endorse any of [university/educational entity's name goes here]'s products or services. Internal or personal use of this material is permitted. If interested in reprinting/republishing IEEE copyrighted material for advertising or promotional purposes or for creating new collective works for resale or redistribution, please go to http://www.ieee.org/publications_standards/publications/rights/rights_link.html to learn how to obtain a License from RightsLink.

If applicable, University Microfilms and/or ProQuest Library, or the Archives of Canada may supply single copies of the dissertation.

BACK CLOSE WINDOW

Copyright © 2014 Copyright Clearance Center, Inc. All Rights Reserved. [Privacy statement](#).
Comments? We would like to hear from you. E-mail us at customer@copyright.com

Figure A.1. IEEE copyright information

ABOUT THE AUTHOR

Srinath Rajaram received the B.E. degree in Electronics and Communication Engineering from Anna University, India, in 2005. He worked for Tata Services, Inc. for three years and left job to pursue his Masters in Electrical Engineering. He received his M.S. degree in Electrical Engineering from University of South Florida, Tampa, U.S.A, in 2013, and currently pursuing the Ph.D. degree in Electrical Engineering at University Of South Florida. His research interests include designing and modeling nanodevices for data storage and logic computation applications.